Theoretical and Experimental Investigations on Microelectrodeposition Process

Atieh Haghdoost

Dissertation submitted to the Faculty of the
Virginia Polytechnic Institute and State University
in partial fulfillment of the requirements for the degree of

Doctor of Philosophy
In
Mechanical Engineering

Ranga Pitchumani, Chair
Masoud Agah
Rafael V. Davalos
Roop Mahajan
Dwight D. Viehland

August 02, 2013
Blacksburg, Virginia

Keywords: Electrochemistry, Multiphysics Modeling, Micro/Nano Fabrication, Micro/Nano Electrochemical Systems, Nanoscale Characterization Techniques, Materials Structure-property Relationship

Theoretical and Experimental Investigations on Microelectrodeposition Process

Atieh Haghdoost

Abstract

Electrodeposition is one of the main techniques for fabricating conductive parts with one or two dimensions in the micron size range. This technique is utilized to coat surfaces with protective films of several micrometers thickness or fabricate standalone microstructures. In this process, an electrochemical reaction occurs on the electrode surface by applying an electric voltage, called overpotential. Different electrochemical practices were presented in the literature to obtain kinetic parameters of an electrochemical reaction but most of these practices are hard to implement for the reactions occur on a microelectrode. Toward addressing this issue, the first part of the dissertation work presents a combined experimental and analytical method which can more appropriately provides for the kinetic measurement on a microelectrode.

Another issue which occurs for electrodeposition on microscale recessed areas is the deviation of the profile of the deposition front from the substrate shape. Non-uniform deposition front usually obtains for a deposit evolved from a flat substrate with microscale size. Consequently, a subsequent precision grinding process is required to level the surface of the electrodeposited microparts. In order to remove the need for this subsequent process, in the second and third parts of the dissertation work, multiphysics modeling was used to study the effects of the fabrication parameters on the uniformity of the deposit surface and suggest a design strategy.

Surface texture of the deposit is another parameter which depends on the fabrication parameters. Several important characteristics of the electrodeposited coating including its wettability depend on the surface texture. The next part of the dissertation work presents an experimental investigation and a theoretical explanation for the effects of the overpotential and bath concentration on the surface texture of the copper deposit. As a result of this investigation, a novel two-step electrodeposition technique is developed to fabricate a superhydrophobic copper coating.

In the last part of the dissertation work, similar investigation to the previous sections was presented for the effects of the fabrication parameters on the crystalline structure of the deposit. This investigation shows that nanocrystalline and superplastic materials can be fabricated by electrodeposition if appropriate fabrication parameters are applied.

Acknowledgements

I would like to express my deepest gratitude and appreciation to my advisor, Dr. Ranga Pitchumnai, for his insightful advice and compassionate support throughout my PhD studies. I appreciate his tremendous insight, guidance, resourcefulness, kindness, and patience throughout this research. He introduced me to the wonders, accomplishments, and frustrations of a scientific research. Dr. Pitchumani's mentorship style granted me freedom and independence without which my achievements would have been of less significance and flavor.

Many thanks go to Dr. Masoud Agah, Dr. Rafael Davalos, Dr. Roop Mahajan, and Dr. Dwight Viehland for serving in my committee and providing valuable inputs on this research. I would also like to thank Dr. William Reynolds for the thought-provoking discussions during the course of this work. His scientific personality would remain an inspiration to me throughout my entire life. In addition, I would like to acknowledge Dr. Jerry Hunter and Dr. Niven Monsegue for useful discussions during the course of this work. I also greatly acknowledge the contribution of Dr. Arash Bahrami and Mr. Mehdi Kargar in the 2^{nd} and 5^{th} chapters of the dissertation work. It is hardly enough to mention the debt I owe to my previous advisors and mentors, Dr. Asghar Dehkurdi, Dr. Masoud Darbandi, Dr. Hossein Haj-Hariri, Dr. Carl Knospe and Dr. Sean Corcoran, for believing in me, for teaching me how to think independently, and for challenging me to grow.

Last but not least, words cannot bring to express my heartfelt, eternal gratitude, appreciation, and thanks to my wonderful husband, Mehdi. I feel fortunate to have such a supportive husband which has always offered me courage, inspiration, and strength to prevail over the personal difficulties and professional challenges in the arduous times of my life. In a way, my PhD degree in the Mechanical Engineering is the crop of the seeds my parents planted years ago by their immaculate training and never-ending sacrifices. To my family, I wish to dedicate this dissertation.

The research in this dissertation is partially funded by the National Science Foundation through Grant No. CBET-0934008. Their support is gratefully acknowledged.

Table of Contents

List of Figures

Chapter 1: Introduction

Though electrodeposition is mainly known as a competitive coating technique, its ability to produce shapes to close dimensional tolerance with controlled roughness and metallurgical properties ensures that electrodeposition is a viable process in precision micro-manufacturing. In fact, when fabrication requirements specify high tolerance, complexity, miniature geometry, and specific surface and crystalline structure, electrodeposition is a serious contender and in certain cases may be the only economically viable manufacturing process [1]. Dissertation work aims at improving the current understanding of different aspects of the electrodeposition process for making both protective coatings with several micrometers thickness or standalone microstructures. In this work, electrodeposited films are called one-dimensional microparts while standalone microstructures are referred to as two-dimensional microparts.

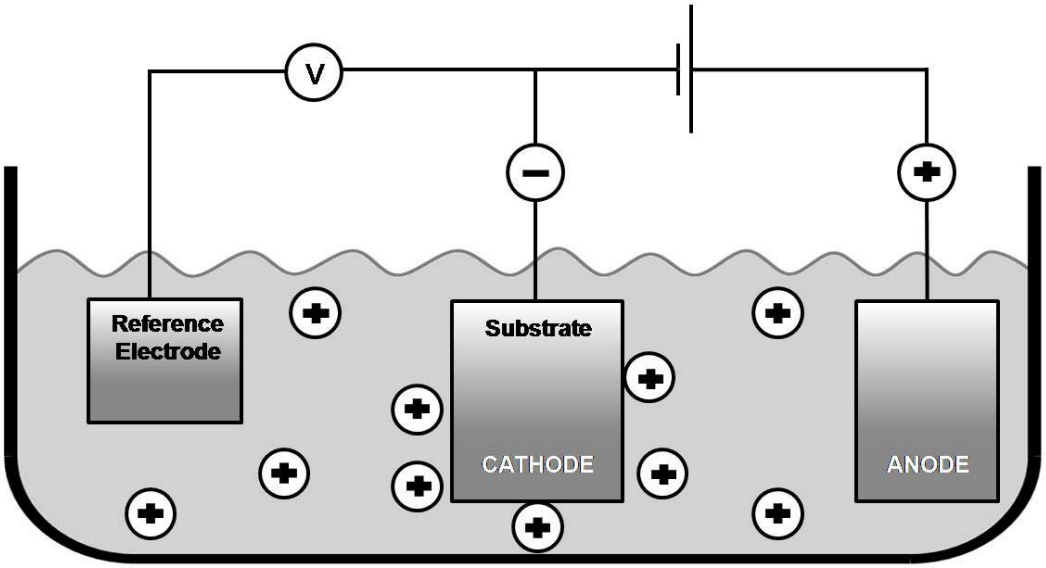

Figure 1: Schematic of the electrodeposition process

Figure 1 shows schematic of the electrodeposition process. The process is composed of three conductive electrodes placed in an ionic solution, electrolyte. As used herein, the term "substrate" refers to a surface, part, or item on which deposition occurs. Substrate plays the role of the cathode in the electrodeposition process. Electrodeposition voltage is measured against the voltage of a reference electrode. If the reference electrode is composed of the same material as deposit, the voltage is called overpotential. The third electrode in an electrodeposition cell is called anode which is usually a non-reacting electrod. When a negative overpotential is applied to the electrochemical cell, positively charged metallic ions are transferred to the cathode surface. The overpotential provides the driving force for an electron-transfer reaction which occurs on the cathode surface. This electrochemical reaction results in neutralizing ions on the electrode surface and consequently, a metallic deposit which is negative in feature with respect to the cathode is formed.

The process schematic shown in Figure 1 is used for both coating the substrate surface and making two-dimensional microparts which are initially attached to the substrate. The only difference is that for making two-dimensional microparts, deposition occurs through microsize patterns made on a layer of photoresist spread over the cathode surface. This microfabrication technique is called LIGA, an acronym for the German words for lithography, electrodeposition and molding. The steps of the LIGA process are shown in Figure 2. Synchrotron radiation lithography is used to make patterns with micron dimensions on a layer of photoresist spread over a conducting substrate (Figure 2a and Figure 2). Each pattern is considered a primary micromold with a conducting base and insulating walls, such that the metal deposit originates from its conducting base and grows along the insulating walls conforming to the micromold geometry (Figure 2c). Therefore, a metallic microstructure that is negative in feature with respect to the micromold

(Figure 2d) is formed which can be either used directly or placed as a mold insert in an injection molding process to force a metal microscreen into a softened thermoplastic (Figure 2e). The injection molding process results in the formation of the secondary micromold composed of a microscreen base and thermoplastic walls (Figure 2f). The holes of the microscreen are filled by the thermoplastic during the injection molding process and form insulating parts on the base of the secondary micromold. In contrast, the base of the primary micromold is composed of an integrated conductive part. In addition, the cost and fabrication time of the secondary micromold are much less than the primary micromold [2-5].

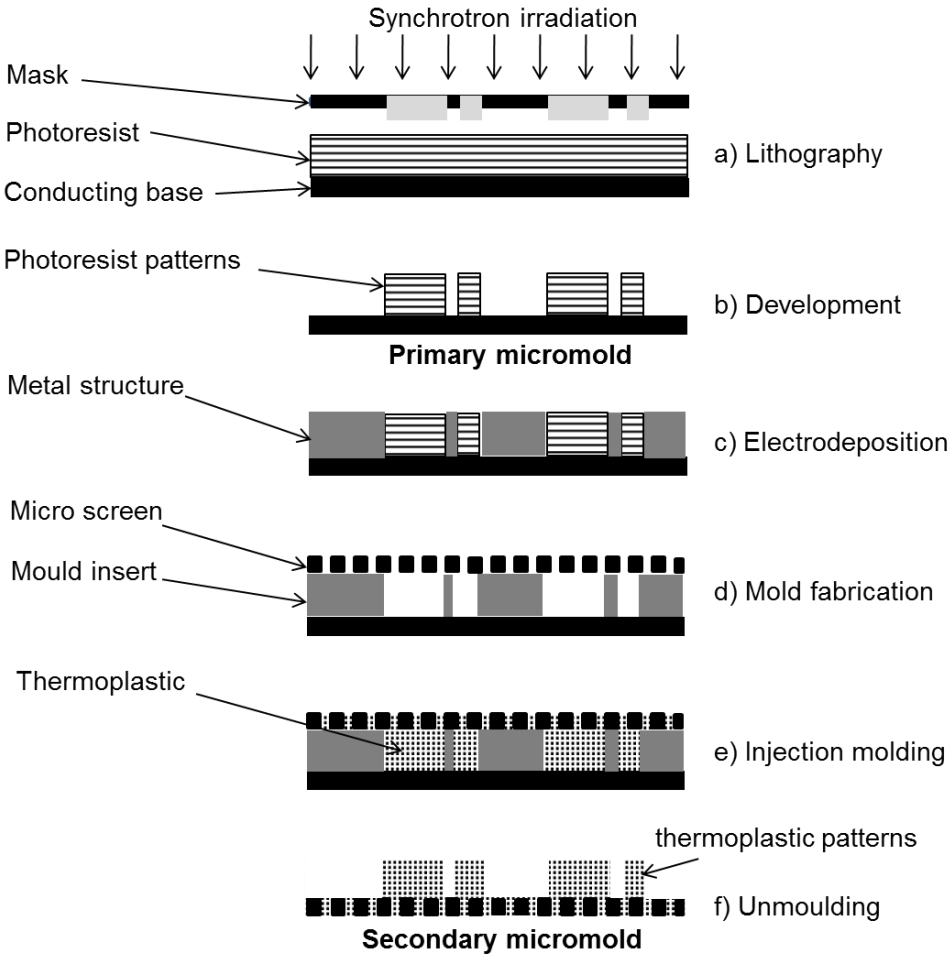

Figure 2: Steps of the LIGA process

Regardless of the electrode size, electrodeposition is composed of two main steps in serial configuration: a mass transfer process from the bulk solution to the electrode surface and an electron-transfer reaction on the electrode surface. The more facile step of this series is held back from its maximum rate by the slower step; therefore, the deposition rate is often limited by the inherent sluggishness of one of these steps called rate determining step. The rates of all steps in the series are the same and equal to the deposition rate, *N*, which can be obtained by measuring current, *I*, using Faraday's equation:

$$N = \frac{I}{nF} \tag{1}$$

in which *n* and *F* stand for the number of transferred electrons in the electrochemical reaction and Faraday constant, respectively. The effects of the mass transfer and electron transfer rates on the deposition rate may be explained considering following electrochemical reaction:

$$O^+ + \ e \rightleftarrows O \tag{2}$$

The mass transfer in the electrolyte may occur through three separate processes: diffusion, electromigration and convection. Following equation is obtained for the total mass transfer rate, using the total mass transfer rate coefficient of k_m:

$$N = Ak_m(c_0 - c_s) \tag{3}$$

where *A*, c_0, and c_s refer to the electrode surface area, bulk concentration, and surface concentration of the depositing ion, respectively. Similarly using reaction rate coefficient of k_r, deposition rate may be evaluated from the rate of the electron-transfer reaction, Eq. (2), as follows:

$$N = Ak_r(c_s e^{-\frac{\alpha F\eta}{RT}} - e^{\frac{(1-\alpha)F\eta}{RT}}) \tag{4}$$

where η is the overpotential, which is defined as the difference between the electrode potential, *E*, and the equilibrium potential, E_{eq}, ($\eta = E - E_{eq}$). Furthermore *T*, *R*, and α denote temperature, universal gas constant, and transfer coefficient, respectively. The first and second terms in the

parentheses of Eq. (4) correspond to the reducing and oxidation components of the reaction shown in Eq. (2), respectively.

From mass transfer and electrode reaction steps, the one with the slowest rate coefficient is known as the rate determining step in electrodeposition. In the extreme cases, when one of the rate coefficients is much larger than the other one, the effect of the very fast step can be completely neglected. The condition of very fast mass transfer with respect to the electrode reaction ($k_m \geq k_d$) occurs under a convective mass transfer regime in a well-mixed bath or if sufficiently low overpotential is applied in a diffusive bath. At these cases, electrolyte concentration profile is uniform ($c_s \approx c_0$) and deposition is mainly controlled by the electrochemical reaction. In contrast, the condition of very fast electrode reaction with respect to the mass transfer ($k_d \geq k_m$) occurs when a high overpotential is applied in a diffusive bath. At this condition, surface concentration approaches zero ($c_s \approx 0$ [M]) and the effect of the electrode reaction on the electrodeposition process is negligible compared to the mass transfer effect.

Other than these extreme cases, the effect of both mass transfer and electrode reaction steps should be considered in electrodeposition. These steps are linked together through the concentration of the depositing ion on the electrode surface, c_s. Characterizing the kinetic parameters of the electrode reaction is necessary to analyze the electrodeposition process when reaction step is not negligible compared to the mass transfer process. The transfer coefficient, α, shown in the exponents of Eq. (4), is known as one of the kinetic parameters. The second kinetic parameter is the exchange current density, i_0, which relates to the reaction rate coefficient, k_r, in the pre-exponent term of Eq. (4) through the following equation:

$$i_0 = F k_r c_0 \tag{5}$$

Equation (4) may be used to determine i_0 and α, but the main difficulty of this method for obtaining the kinetic parameters is finding the concentration of the reactant on the electrode surface, c_s. In order to address this difficulty, different procedures have been suggested in the previous studies [6-12]. Each of these procedures has its own limitations and is able to determine appropriate kinetic parameters under specific conditions. The most common technique, which was implemented by several authors [6, 13, 14], requires applying very low overpotentials, which makes that hard to implement for kinetic measurement of the reactions occur on a microelectrode. Toward addressing this issue, the second chapter of the dissertation presents a combined experimental and analytical method, which can be used at higher overpotentials compared to the traditional kinetic measurement technique. Consequently, this combined method more appropriately provides for prediction of kinetics of the reactions occur on microscale electrodes.

Another issue which specifically occurs during electrodeposition on microscale recessed areas is the evolution of a nonuniform deposition front from a flat microelectrode. The deviation of the profile of the deposition front from the substrate shape is a consequence of the diffusive mass transfer in the bath. When mass transfer is partially or completely governed by diffusion, ion concentration along the edges of the electrode surface, which are more accessible to the bath, is higher than the central part. The nonuniform concentration results in the higher deposition rate along the microtrench edges and evolution of a volcano structure from the initially flat deposit surface. This effect of the diffusion process on the nonuniformity of the deposition front is referred to as the "edge effect" in this dissertation. Though edge effect is usually negligible for electrodeposition on a large electrode, its effect on the shape of the electrodeposited structure can be significant for electrodeposition on a microscale electrode and especially for electrodeposition through a micromold during LIGA process. This is because mass transfer through a micromold is

mainly controlled by diffusion. Even if convection is applied in the bath, the speed of the induced circulating flow in the micromold falls dramatically along the depth of the micromold and transport is controlled by diffusion along most of the micromold depth [15].

Evolution of the volcano deposition front in electrodeposition through a micromold requires a subsequent precision grinding process to level the surface of the microparts. The third chapter of the dissertation work aims at removing the need for this subsequent process in electrodeposition through a primary micromold. To this end, multiphysics modeling has been used to simulate temporal evolution of deposition front in a primary micromold. The work presents a systematic study for the effects of the applied overpotential and micromold geometry on the uniformity of the deposit surface. Consequently, a design strategy has been suggested to obtain a flat deposition front at the highest possible deposition rate. Unlike models presented previously in the literature [16], the model presented in this work covers the complete range of the relevant overpotentials. This model has been presented previously in a couple of literatures [15, 16] but it has been used for the first time for the detailed analysis of the effects of the fabrication parameters on the uniformity of the deposit surface.

Unlike electrodeposition through a primary micromold, relatively few investigations are found in the literature on electrodeposition through a secondary micromold. The base of the secondary micromold is composed of the insulating thermoplastic and conductive metal parts. Chen and Evans [16] showed that the deposit surface is essentially flat when the thermoplastic part of the base is elevated relative to the microscreen metal. In contrast, dimples are formed on the deposit surface when the microscreen metal is slightly elevated relative to the thermoplastic parts of the microtrench base. In this case, uniformity of the deposit surface depends on the size and number of the insulating holes on the micromold base in addition to the “edge effect”. In the work presented

by Chen and Evans, the effect of the microscreen geometry on the shape profile of the deposition front has not been presented. Later on in this dissertation, the effect of the insulating holes on the deposit surface profile is referred to as the "active-area density effect". In the fourth chapter of the dissertation work, a model for the electrodeposition through a secondary micromold considering both "edge effect" and "active-area density effect" is presented. This model is used to systematically study the evolution of the deposition front through a secondary micromold and find the effects of the microscreen geometry (i.e. size and number of the insulating holes) on the fill time and uniformity of the deposition front.

In electrodeposition, surface texture of the deposit is another parameter which depends on the fabrication parameters. Unlike uniformity of the deposition front, the study of the deposit surface texture is more significant for the one-dimensional microparts. Several important characteristics of the electrodeposited coatings including their wettability depend on the surface texture. In the fifth section of the dissertation work, an experimental investigation is presented for the effects of the overpotential and bath concentration on the surface texture of the copper deposit, which has not been reported in the literature with this detail, previously. This investigation shows that morphological instabilities, which are inherently made during electrodeposition [17-20], are enhanced by increasing overpotential or bath concentration. Beyond a certain stage, these instabilities can provide the surface texture which satisfies the requirements for the superhydrophobic state. Based on these requirements, the static contact angle of a sessile droplet on the surface should be higher than 150°; in addition, a dynamic droplet should not stick to the surface [21-26].

As a result of the experimental investigation on the surface texture of the deposit, a novel two-step electrodeposition technique is developed to fabricate a superhydrophobic copper coating. In

the first step, applying a high overpotential in a concentrated electrolyte results in the formation of fractal-shaped structures, which are loosely attached to the surface. In the second step, an additional thin layer of the deposit is formed by applying a low overpotential for a short time, which is used to reinforce the loosely-attached structures on the surface. This method is a potentially low-cost and simple approach for coating metallic surfaces with an enduring superhydrophobic film which is totally made of copper. In addition to the experimental investigation, this part of the dissertation also presents a theoretical explanation, based on similar models presented in the literature on thermal solidification [27], to explain formation of the morphological instabilities during electrodeposition. This theoretical explanation shows that though deposit growth is always unstable, the instability is enhanced by applying a larger overpotential or using a more concentrated electrolyte. At high overpotential in a concentrated bath, the electrodeposition is so unstable that branches which become detached from the deposit surface can grow independently in the electrolyte. This unstable growth process results in the formation of the fractal-shaped structures which are known as the main reason of the superhydrophobic characteristic of the deposit.

Last section of the dissertation work explains the effects of the fabrication parameters on the crystalline structure of the deposit. The crystalline structure of an electrodeposited metal usually differs from the samples made by other techniques. In addition to the high level of impurities and defects, size and shape of the crystalline grains are also different in the metal made by electrodeposition compared to other techniques [28]. In particular, metals with small crystalline grains, such as nanocrystalline and superplastic metals, can be obtained by applying appropriate process variables during electrodeposition. In the six section of the dissertation work, an experimental investigation was presented for the effects of overpotential and current density on the

internal structure of the copper deposited from a copper sulfate bath. In addition, the work also presents a theoretical explanation for the effect of the overpotential on the formation of material defects other than the grain boundaries, such as dislocations.

In general, dissertation work explains the effects of the fabrication parameters such as overpotential, size of the substrate and its position in the bath on the uniformity of the deposit surface, surface texture, and crystalline structure of the deposit. These three factors, which are shown in Figure 3, difine different physical, chemical, and mechanical properties of the deposit.

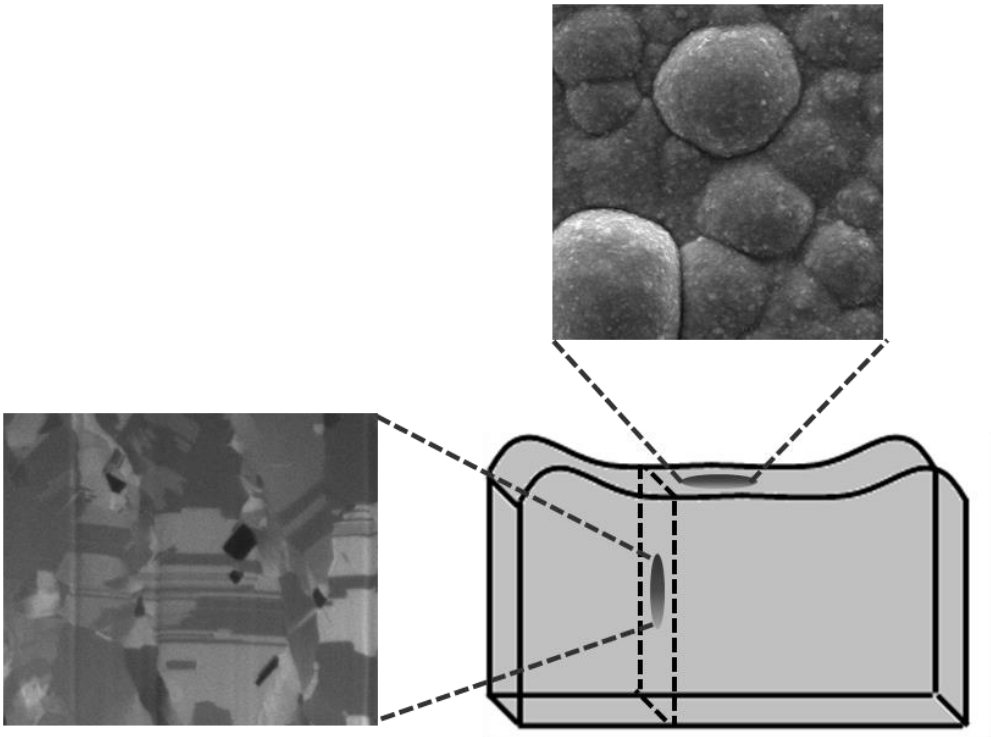

Figure 3: Uniformity of the deposit surface, crystalline structure, and surface texture of the deposit

1.1 Mass Transfer Process in Electrodeposition

The mass transfer in the electrolyte may occur through three separate processes: diffusion, electromigration, and convection. In general, convection reduces the effect of the process parameters such as overpotential, bath concentration, size of the substrate, and its position in the bath, on all three factors of uniformity of the deposit surface, surface texture, and crystalline structure. In fact, in the ideal condition of a well-mixed bath with uniform concentration, these three factors are almost independent of the process parameters. Therefore in the studies presented in the dissertation, quiescent electrolyte is considered, in which mass transfer process is governed by diffusion and electromigration and the effect of convection is neglected.

The relative importance of diffusion and electromigration in a quiescent electrolyte depends on the deposition time and differs at different locations in the electrolyte [29]. In general, diffusion dominates over electromigration at a given position and time, *t*, provided the following condition is satisfied [29]:

$$\xi \ll 2\frac{RT}{nF(2Dt)^{0.5}} \tag{6}$$

where ξ is the field strength, equivalent to the overpotential gradient, and *D* denotes diffusion coefficient. This condition is not usually satisfied in the very thin layer of the electrolyte adjacent to the electrode surface called double layer because large overpotential gradient is the main characteristic of this layer. Therefore, in general the effect of the electromigration is not negligible in the double layer compared to the diffusion. In addition, at very small process times, Eq. (6) is not applicable in the bath and the effect of the electromigration cannot be neglected. In contrast, negligible effect of electromigration compared to diffusion outside the double layer region may be explained by Eq. (6) at the steady-state condition, especially if low overpotentials are applied.

Since the condition presented by Eq. (6) does not necessarily apply in the double layer, the surface concentration obtained from a diffusion equation, c_s, really refers to the concentration outside the double layer. The two concentrations are very close as long as the thickness of the double layer is negligible compared to the diffusion layer thickness. For the electrolyte concentrations used in this dissertation, thickness of the double layer in the order of several nanometers was reported in the literature. At the steady-state condition, diffusion layer thickness depends on the steady-state current density and bulk concentration and at low overpotentials its value is several orders of magnitude larger than the thickness of the double layer.

Despite the relatively large density differences associated with ion depletion during electrodeposition through micromolds, there is very little mention of natural convection in the electrodeposition literature. This is because natural convection plays only a secondary role in conventional plating of flat surfaces. However, the strength of the forced convective transport decreases logarithmically with the ratio of feature depth to width, making it nearly irrelevant for aspect ratios beyond three or four. Thus, only buoyancy-driven convection is important in electrodeposition through high aspect-ratio micromolds [1].

In the natural convection analysis, two dimensionless parameters, Rayleigh and Schmidt numbers, are appear; both are written below in terms of the dynamic viscosity ($\upsilon = \mu/\rho_0$):

$$Ra = \frac{\Delta\rho g H^3}{\rho_0 D \upsilon} \quad ; \qquad Sc = \frac{\nu}{D} \tag{7}$$

The numerical model presented by Griffiths et al. [2] suggested that no motion due to the natural convection will occur for Rayleigh numbers less than a critical value which is strongly dependent on the aspect ratio($A.R = H/W$):

$$Ra_{crit} = 192(A.R)^4 \tag{8}$$

For electrodeposition from a 1 M electrolyte into a micromold having a depth of 1 mm, this criterion suggests that significant convection will only occur for aspect ratios less than about 10 or 20. The allowable aspect ratio is twice as great in features half as deep.

Similar to the forced convection, natural convection reduces the effects of the fabrication parameters on the deposit characteristics such as non-uniformity of the deposit surface. Consequently, the model presented in the third chapter of the dissertation for the effects of voltage on the overplating amount neglects the contributions of both forced and natural convections.

1.2. Thermodynamic Effect During Electrodeposition

Reversibility is an important concept in the thermodynamic study of a process. The term reversibility takes on several different, but related, meanings in the electrochemical literature. The cell is termed chemically reversible, if reversing the cell current reverses the cell reaction. Depending on the electrochemical reaction, electrodeposition may or may not be chemically reversible. In addition, a process is thermodynamically reversible when an infinitesimal reversal in a driving force causes it to reverse direction. Obviously this cannot happen unless the system feels only an infinitesimal driving force at any time. Electrodeposition approaches thermodynamic reversibility if very low overpotential is applied. At this condition, Nernst equation may be used to provide a linkage between electrode potential, *E*, and the concentrations of participants in the electrode process:

$$\mathrm{E} = E^{0\prime} + \frac{RT}{nF} ln \frac{[\mathrm{O}^{+}]}{[\mathrm{O}]} \qquad (9)$$

where $E^{0'}$ formal potential which is measured for the electrochemical reaction when (a) the species O^+ and O are present at concentrations such that the ratio $\frac{[O^+]}{[O]}$ is unity and (b) other specified substances, for example, miscellaneous components of the medium, are present at designated concentrations.

Chapter 2: Determination of Electron Transfer Kinetics on a Microelectrode

This chapter presents an analytical model for the electron-transfer kinetics in an electrochemical process, which is, in turn, used to determine the kinetics parameters with only a limited number of potentiostatic measurements. The method provides a reliable and practical tool for kinetics measurement of fast-electron-transfer reactions or reactions that occur on micro- or sub-micro-electrodes, such as those used in various electrochemical sensors. The method is described in detail by considering the kinetic measurement of the electrochemical reaction of copper on a platinum microelectrode.

2.1 Introduction

Since the invention of electrochemical sensors in the 1950s, different electroanalytical techniques have been widely employed [30] to study the governing phenomena. The interest in developing such techniques has significantly grown due to the emergence of micro- and sub-micro-electrodes following the remarkable progress in microfabrication methods during the past two decades. Moreover, the electron-transfer reactions, occurring in most electrochemical sensors and biosensors have fast kinetics. A deep understanding of the electron-transfer mechanism and characterizing the reaction kinetics are necessary to analyze electrochemical behavior of these sensors in their whole operating range.

Kinetics of an electrochemical reaction depends on both physical and chemical properties of the electrode/electrolyte interface. In fact, kinetic parameters are sensitive to the properties of the electrode surface including chemical composition, crystal structure and metallography [31, 32]. In

addition, most of these properties depend on the preliminary treatment of the electrode surface such as polishing or chemical cleaning process. This complex relationship between the kinetic parameters and surface properties demands developing an inclusive method to determine reaction kinetics, applicable to all electrodes regardless of the size.

The electron-transfer kinetics on a surface can be characterized in terms of two parameters, i_0 and α, representing the exchange current density and the transfer coefficient, respectively. Note that α is a physical measure for the energy path symmetry of the electrochemical reaction and varies from zero to unity. The exchange current density, i_0, indicates the exchange velocity of the electron-transfer process for the overall reaction. It is worth mentioning that i_0 depends on the bulk concentration of the reducing ion, c_0, whereas α is independent of c_0. For a two-step electron-transfer reaction, when the first step of the electron transfer is much more sluggish than the second step, the net current density, i, is given by the following relation, in terms of the two kinetic parameters [6, 33]:

$$i = i_0 \left(\frac{c_s}{c_0} e^{-\frac{\alpha F \eta}{RT}} - e^{\frac{(2-\alpha) F \eta}{RT}} \right) \tag{10}$$

where η is the overpotential, which is defined as the difference between the electrode potential, E, and the equilibrium potential, E_{eq}, ($\eta = E - E_{eq}$), c_s and c_0 are, respectively, the surface and bulk concentrations of the reducing ion, and T, R, and F denote temperature, universal gas constant, and Faraday constant, respectively. The first term in the parentheses of Eq. (10) corresponds to the reducing component of the reaction, which is similar for the one-step and two-step reactions. In general, this term is much larger than the second term in the parentheses of Eq. (10), characterizing the oxidation component of a two-step reaction, unless very low overpotentials are applied. For the range of the overpotentials considered in this study, the second term is three orders of magnitude smaller than the first term, which provides for simplification of Eq. (10) as follows:

$$i = i_0 \left(\frac{c_s}{c_0} e^{-\frac{\alpha F \eta}{RT}} \right) \tag{11}$$

Equation (11) may be used to determine i_0 and α based on the measured observable values, i, η, and c_0, from the experiment. In most practical methods, the transient behavior of one of the observable values is analyzed while the other two are kept constant: In potentiostatic methods, η and c_0 are assumed to remain constant and the transient trend of current is recorded, whereas in galvanostatic transients the time variation of the overpotential is recorded at constant i and c_0 [34]. The main difficulty of the methods for obtaining the kinetic parameters is finding the concentration of the reactant on the electrode surface, c_s. In order to address this difficulty, different procedures have been suggested in the previous studies, which are briefly explained in this section. Surface concentration has a reducing trend during the transient part of the electrochemical deposition and reaches a fraction of the bulk concentration at steady state. In mass-transfer-controlled processes, the reaction kinetics are negligible and, therefore, c_s can be found based on the solution of the mass-transport equation in the Nernst diffusion layer [29]. To obtain kinetic parameters, experiments should be performed at the region where the surface concentration deviates from the Nernstian equilibrium condition. In this region, the surface concentration is influenced by both reaction kinetics and mass transfer. Mattsson and Bockris [6] presented a method to estimate kinetic parameters by conducting a low-current galvanostatic measurement and neglecting the mass transfer effect. Such a condition would lead to a uniform surface concentration distribution, $c_s \cong c_0$, as a result, Eq. (11) may be employed to obtain kinetic parameters. Although the method has been demonstrated to provide sufficiently accurate results for many systems, it is incapable of precise measurement of the kinetic parameters for cases involving fast reactions or for microscale electrodes. For situations involving fast reactions, the impact of the reaction kinetics on the surface concentration may not be neglected even when the current is very small and, thus, the

concentration distribution might not be uniform. Furthermore, for the small electrodes, electrochemical response is hard to measure in a low-current galvanostatic experiment.

Several investigators have utilized extrapolation techniques to find the value of the electrochemical response, i.e., current or overpotential, at the initial time, $t = 0$, when the surface and bulk concentrations are equal [7, 8]. These methods assume that the ideal and the real responses of the system are identical. However, such an assumption is not essentially held in all cases due to the capacitive current and the system ohmic resistance. Capacitive current, induced due to the double-layer charging, gives rise to a peak at the beginning of the transient and then decays gradually. The distance between the working and the reference electrodes causes an uncompensated ohmic resistance, which is the second reason for the deviation of the real electrochemical response from the ideal trend. This deviation results in a serious error in the extrapolation method for obtaining initial current or overpotential value. Therefore, these methods are not capable of finding kinetic parameters, especially when fast reactions are involved [9]. To address the aforementioned limitations, methods like double impulse measurements have been developed [10, 11], in which a high-amplitude perturbation is applied at the beginning of the experiment which results in a complete double-layer charging after a short period of time. A lower current/overpotential is then applied and the consequent electrochemical response is extrapolated to obtain the value of the electrochemical response at the outset. In spite of the fact that this technique resolves the capacitance current issue, for some systems the initial perturbation may cause undesired changes in the reaction mechanism, which are not easily detectable [12].

Most of the methods use either the potentiostatic or the galvanostatic experiment to measure kinetics parameters; the double impulse method, however, may use a combination of both techniques. In addition, cyclic voltammetry has also been employed to obtain exchange current

density, although it fails to reliably estimate transfer coefficient [12]. Each of the available electrochemical approaches in the literature has its own limitations and is able to determine appropriate kinetic parameters under specific conditions. The most common technique in the literature [6, 13, 14] requires applying very low voltages, which makes it hard to implement for measurement of the kinetic parameters of fast-electron-transfer reactions and reactions that occur on a microelectrode.

Toward addressing the aforementioned issues and to overcome practical challenges involved in the conventional kinetic measurement methods, this paper presents a combined experimental and analytical method, which can be used at higher overpotentials compared to the low-current technique explained before. Consequently, this combined method more appropriately provides for prediction of kinetics of the fast-electron-transfer reactions or reactions occur on microscale electrodes. The method used a set of potentiostatic experiments to obtain kinetic parameters. Equation (11) holds for both transient and steady state parts of the potentiostatic deposition, although, the steady-state values are utilized in the present method. Steady-state current, $\boldsymbol{i}_{\infty}$, corresponding to each constant overpotential, η, is measured, and used in a galvanostatic model, such that the steady-state surface concentration, c_s, obtained from the model would be identical with that of the potentiostatic experiment. Note that, for the potentiostatic experiment, the mass transfer flux on the electrode surface depends on the surface concentration, and the associated boundary-value problem does not admit a closed-form solution. For a galvanostatic system, on the other hand, the mass transfer flux on the electrode surface is constant, which permits a closed-form solution for the surface concentration as developed in the next section. Equation (11) is utilized to determine kinetic parameters, i_0 and α, using the measured data and the theoretically evaluated c_s.

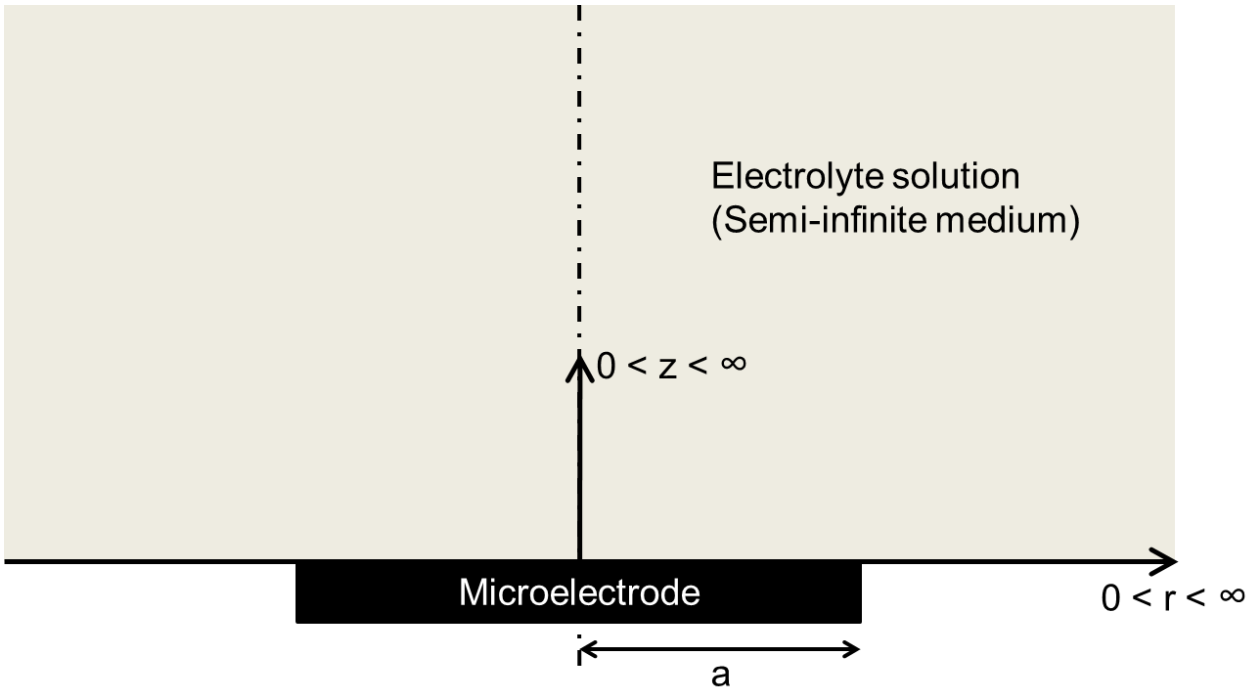

Figure 4: Schematic of the mathematical model: A disk-shaped microelectrode of radius *a* which is surrounded by a semi-infinite cylindrical domain.

The mathematical model is discussed in Section 2, followed by a description of the experimental study in Section 3 and a discussion of the results of the study in Section 4.

2.2 Mathematical Model

The mathematical model of a galvanostatic system is developed by considering a disk-shaped microelectrode of radius, *a*, which is surrounded by a semi-infinite cylindrical domain, as illustrated in Figure 4. The origin of the cylindrical coordinate system is coincident with the center of the disk. In the copper sulfate electrolyte used in this work, both H^+ and Cu^{2+} ions may reduce on the cathode surface. However, in the overpotential range used in this study, hydrogen evolution

is negligible [29] and reduction of copper, described by the reactions shown below [35, 36], are the only electrochemical reactions that occur on the microelectrode:

$$Cu^{2+} + e^- \leftrightarrows Cu^+$$
$$Cu^+ + e^- \leftrightarrows Cu \tag{12}$$

Note that copper reduction is used here as an example to describe the present model, although the model is equally applicable to the other one-step or two-step electrochemical reactions as well. The thickness of the deposit formed during the time durations considered in this study is at least three orders of magnitude smaller than the diffusion layer thickness, as verified later in this chapter. Therefore, the change of the microelectrode shape during deposition, which has been explained in other works [37, 38], has negligible effect on the concentration profile in the bath and is neglected in this model. Moreover, the diffusion coefficient in the electrolyte is considered to be constant.

In a quiescent electrolyte, mass transfer occurs by diffusion and migration. The relative contributions of these two mass-transfer methods to the flux of the reducing agent depends on the deposition time and differs at different locations in the electrolyte [29]. For the overpotential and concentration range used in this work, diffusion is the main mass-transfer process at steady state, and the effect of the migration can be neglected. This assumption is also verified later in this chapter. Under these assumptions, the steady-state diffusion of the reducing agent, Cu^{2+}, in the semi-infinite cylindrical domain, is governed by the following dimensionless equation:

$$\frac{1}{r^*}\frac{\partial}{\partial r^*}\left(r^*\frac{\partial c^*}{\partial r^*}\right) + \frac{\partial^2 c^*}{\partial z^{*2}} = 0 \tag{13}$$

where $c^*(r^*,z^*)$ represents the dimensionless steady-state concentration of Cu^{2+} ions, and the asterisked terms denote dimensionless parameters defined as:

$$c^* = \frac{c_0 - c}{c_0}, \qquad z^* = \frac{z}{a}, \qquad r^* = \frac{r}{a} \tag{14}$$

Equation (13) is associated with the following boundary conditions:

$$\frac{\partial c^*}{\partial r^*}(0, z^*) = 0 \tag{15}$$

$$c^*(\infty, z^*) = c^*(r^*, \infty) = 0 \tag{16}$$

$$\frac{\partial c^*}{\partial z^*}(r^*, 0) = \begin{cases} -\dfrac{i_\infty a}{FnDc_0} & 0 \le r^* \le 1 \\ 0 & r^* > 1 \end{cases} \tag{17}$$

Equation (17) shows the constant mass-transfer flux or constant current density on the electrode surface, which occurs in a galvanostatic system, as mentioned previously. In this equation, i_∞ is the steady-state current density, which is determined from the potentiostatic measurements, c_0, F, D and n are, respectively, the bulk concentration, Faraday constant, diffusion coefficient and the number of transferred electrons; n = 2 for the copper reduction reaction. Using the method of separation of variables [39], the solution to the partial differential equation in Eq. (13) and the associated boundary conditions may be expressed as:

$$c^*(r^*, z^*) = \int_0^\infty e^{-\lambda z^*} J_0(\lambda r^*) f(\lambda)\, d\lambda \tag{18}$$

where $f(\lambda)$ is determined so as to satisfy the prescribed conditions on the plane $z^* = 0$, Eq. (17), λ is the eigenvalue of the problem, and $J_0(.)$ is the Bessel function of the first kind of order zero. Using the following relation of Bessel functions [40]:

$$\int_0^\infty J_0(\lambda r^*) J_1(\lambda)\, d\lambda = \begin{cases} 0 & if\ r^* > 1 \\ 1 & if\ r^* < 1 \end{cases} \tag{19}$$

It is evident that the steady-state concentration profile of Cu^{2+} in the bath in the presence of the microelectrode is given by:

$$c^*(r^*, z^*) = \frac{i_\infty a}{FnDc_0} \int_0^\infty e^{-\lambda z^*} J_0(\lambda r^*) J_1(\lambda) \frac{d\lambda}{\lambda} \quad (20)$$

The average dimensionless concentration of Cu^{2+} ions over the circular electrode surface, $z^* = 0$ and $0 < r^* < 1$ is, then, obtained using Eq. (20) as:

$$c_s^* = \frac{2 i_\infty a}{FnDc_0} \int_0^1 \int_0^\infty J_0(\lambda r^*) J_1(\lambda) \frac{d\lambda}{\lambda} r^* dr^* \quad (21)$$

The numerical calculation of the integral in Eq. (21) results in the following equation for c_s^*:

$$c_s^* = 0.849 \frac{i_\infty a}{FnDc_0} \quad (22)$$

The average surface concentration given by Eq. (22), together with the relationship for the current, given by Eq. (11), will be used to determine the kinetic parameters, as discussed in Section 4.

2.3 Experimental Studies

Reagents. The chemicals used in this study are of analytical grade or better all supplied by Fisher Chemicals (Pittsburgh, PA, USA). Solution of copper sulfate and sulfuric acid was used as the electrolyte while acetone, nitric acid, sodium hydroxide and hydrochloric acid were used to clean the electrode surface. Distilled deionized water (18.2 MΩ.cm) with the maximum total organic carbon of 8 ppb was utilized for all different purposes.

Apparatus. Electroanalytical measurements were performed using an AUTOLAB PGSTAT128N potentiostat (ECO Chemie, Utrecht, The Netherlands), with a low-current module, especially tailored for electroanalytical measurements with microelectrodes. The potentiostatic measurements were done in a cell composed of a platinum mesh and a platinum microelectrode as the counter and the working electrodes, respectively. Also, a copper sheet (99.9 %) was used as a reference electrode for all experiments, unless otherwise mentioned. The platinum microelectrode

(Bioanalytical Systems, West Lafayette, IN, USA) is a disk with 100 μm diameter, sealed to a glass support. To eliminate effects of oxygen and contamination in the working environment, all electrochemical measurements were performed in glove bags, filled with high-purity nitrogen (99.995 %, Airgas).

Experimental Procedure. High purity of all components of an electrochemical cell is important for accurate experimental results [41, 42]. Impurities adversely influence the reproducibility of the experiment because they have uncontrolled effects on the mass transfer process in the bath and on the surface characteristic of the electrode [43]. In this work, the procedure described below, which is presented by May et al. [44], was used to remove impurities from the experimental setup.

All glassware were washed sequentially with a hot detergent solution, deionized (DI) water and neutralizing acid, followed by successive rinsing with hot DI water and drying at 90 °C. After degreasing in acetone and a hot 1M NaOH solution, the platinum mesh electrodes were pickled in 5 N HCl and 5 N HNO_3 solutions, consecutively. The electrodes were rinsed thoroughly with DI water after each surface treatment. The platinum microelectrode was polished with 1 μm diamond paste and 0.05 μm alumina slurry, and was sonicated for 4 min in DI water. After this mechanical preparation, the platinum microelectrode was subject to the same surface treatments as the platinum mesh. The electrodes were kept in the electrolyte solution after finishing chemical surface treatments. It should be noted that a new surface treatment was required if the electrodes were removed from the bath. Three sets of the potentiostatic measurements were performed with different electrolyte concentrations. In order to remove any copper-platinum alloy that might be formed on the electrode surface, the microelectrode was polished before each measurement set.

To minimize reducible impurities, pre-electrolysis treatment was performed using two strips of a platinum mesh. A current of 0.024 A was applied for at least 24 hr in a 0.5 M sulfuric acid

electrolyte (blank solution). Moreover, to remove oxygen from the pre-electrolyzed solution, it was bubbled with high-purity nitrogen for one hour before the next step. Before each measurement set, the microelectrode was subjected to cyclic polarization in the pre-electrolyzed solution at the potential scan rate of 0.05 V/s. Coincidence of the polarization curves in both oxygen and hydrogen regions was verified to guarantee that the electrode surface remained unchanged. In order to provide measurement stability during cyclic polarization, a mercury-mercury sulfate reference electrode was used instead of the copper sheet. A voltage range from –0.56 V to 0.64 V was applied and the polarization curve shape was monitored to ensure reproducible surface condition for all measurements. It was found that the oxide reduction peak occurred at 67 mV for all curves, in agreement with the value reported in the literature [36].

After cyclic polarization, $CuSO_4$ was added to the sulfuric acid solution to make electrolytes with following concentrations: (1) 0.5 M H_2SO_4 and 1 M $CuSO_4$, (2) 0.5 M H_2SO_4 and 0.5 M $CuSO_4$, and (3) 0.5 M H_2SO_4 and 0.1 M $CuSO_4$. Though high concentration of H_2SO_4 relative to $CuSO_4$ serves to eliminate the effect of the migration even at large overpotential magnitudes, the impurities presented by such large concentration can cause serious interference in the experiment[29]. Therefore in this work, the H_2SO_4 concentration was kept at 0.5 M, and in order to eliminate the effect of migration, overpotential magnitudes less than 0.3 V were applied. As explained in the results and discussion section of this paper, the impact of migration compared to diffusion at the condition used in this work is negligible.

Before each potentiostatic experiment, the solution was bubbled with high-purity nitrogen for another hour. For further activation of the platinum microelectrode, a high voltage of 0.59 V was applied for 360 sec before each potentiostatic measurement set. The voltage was reduced from 0.59 V to 0 V with the scan rate of 0.05 V/s and then kept constant for 500 sec. Using this

procedure, a full coverage of the underpotential deposition (UPD) layer on the electrode surface was achieved, thereby the effects of the UPD formation on the subsequent potentiostatic measurement were eliminated. For each electrolyte, the potentiostatic curves were obtained by applying five different overpotentials in the range of –0.30 V to –0.1 V, with repeated measurements, that indicated a perfect reproducibility.

2.4 Results and Discussion

The variation of current, *i(t),* with time was measured at different overpotentials using the potentiostatic experiments described in the previous section. The results are examined in terms of a superficial current density, $i_s(t)$, defined as the current *i(t)* divided by the electrode superficial area ($A_s = \pi a^2$). Since the active area of the electrode changes during the deposition process, the superficial current density might differ from its actual value, *i*, throughout the transient process. Figure 5a–c show the time-variation of the superficial current density obtained from the potentiostatic experiments when overpotentials of –0.1 V, –0.2 V, and –0.3 V are applied, respectively. The figures present the results of potentiostatic experiments performed on three electrolytes with bulk $CuSO_4$ concentrations, c_0, of 1 M, 0.5 M, and 0.1 M. The superficial current density initially increases with a sharp gradient to a maximum value, as seen in **Error! Reference source not found.**a–b for the electrolytes with 1 M and 0.5 M $CuSO_4$ concentrations in the bulk. For the other curves, the gradients are so sharp that the maximum points are not evident in the plots. After reaching a maximum point, superficial current density decreases to a local minimum which is seen clearly for the curves corresponding to the $CuSO_4$ concentrations of 1 M and 0.5 M in Figure 5 a–c. For the

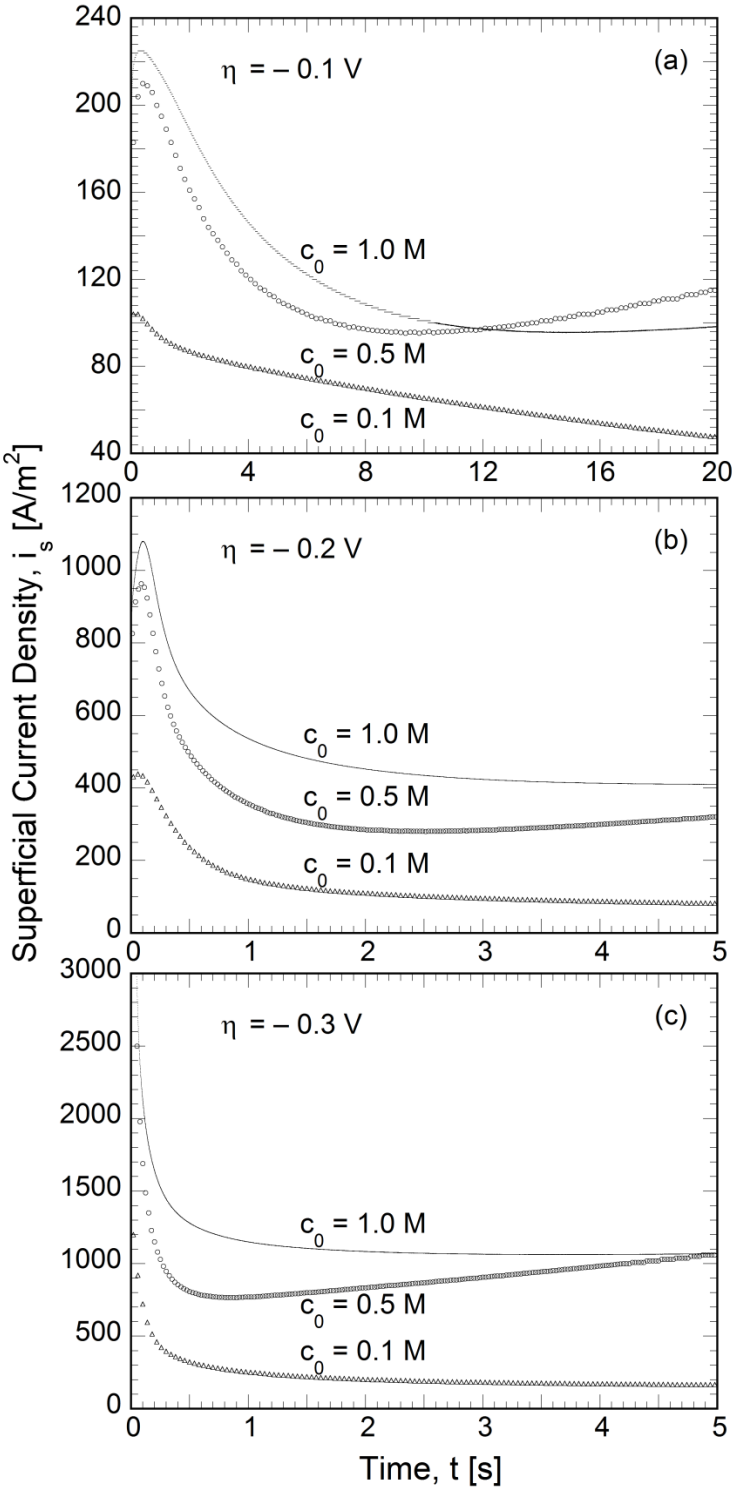

Figure 5: Time variation of the superficial current density, $i_s(t)$ for the electrolytes with 0.1 M, 0.5 M, and 1 M $CuSO_4$ concentrations when overpotential of η = (a) -0.1 V, (b) -0.2 V, and (c) -0.3 V is applied in a potentiostatic experiment.

electrolyte with 0.1 M $CuSO_4$ concentration, the local minimum occurs beyond the time scales shown in Figure 5a–c.

In general, the superficial current density varies with time during the deposition process because of (1) changes in the electrolyte concentration on the electrode surface and (2) changes in the active electrode area. The former decreases monotonically from c_0 to the steady-state concentration while the latter initially increases due to an increase in the size and number of the nucleation sites and after reaching a maximum decreases to a local minimum value [45, 46]. The larger the overpotential, the sharper the initial gradient observed in Figure 5a–c. It was also found that at the local minimum of the superficial current density, the surface concentration approaches that of the steady state. In addition, at this point, an almost flat deposition front is formed whose surface area is very close to the electrode area of πa^2 in the reference configuration (Figure 4). Therefore, the superficial current density at the local minimum, denoted as the steady state current density, i_∞, can be used for i in Eq. (11). After this local minimum, the flat deposit surface gradually evolves to a volcano structure due to edge effects [37, 38], resulting in a gradual increase of the active area and consequently, a slight increase in the final value of the superficial current density.

The diffusion layer thickness, L, is obtained from the following equation, at the steady-state condition[35]:

$$L = \frac{nFDc_0}{i_\infty} \tag{23}$$

Using the steady-state current densities, i_∞, obtained from the local minima of Figure 5c, and diffusivity value of 1×10^{-9} m^2/s in Eq. (23), a diffusion layer thickness of around 1×10^{-4} m is obtained for a bath with 0.1 M, 0.5 M, and 1 M $CuSO_4$ concentrations, with an applied overpotential of –0.3 V. Note that a larger thickness of the diffusion layer is expected for smaller

overpotential magnitudes. The deposit height, *h*, at the local minimum of the potentiostatic curve ($t = t_{min}$) is obtained from the following equation:

$$h = \frac{M}{nF\rho}\int_0^{t_{min}} i_s dt \tag{24}$$

where M and ρ are the molecular weight and density of the copper deposit. At the local minimum points of Figure 5c, Eq. (24) results in the deposit heights of 1.6×10^{-7} m, 3.0×10^{-8} m, and 4.3×10^{-8} m, respectively, for electrolytes with 1 M, 0.5 M, and 0.1 M $CuSO_4$ concentrations, when the overpotential of –0.3 V is applied. At distances far away from the microelectrode surface, which cover most of the diffusion layer thickness, the system does not sense the difference between the superficial and active areas [47]. At these distances, the assumption of negligible change in the microelectrode shape, used in the model presented in Section 2, holds and the current density corresponds to i_s. In contrast, superficial and actual current densities are different on the electrode surface at all times except the times corresponding to the local minimum points in Figure 5a–c, as explained before.

For the electrolyte concentrations between 0.1 M and 1 M, the double layer thickness was reported to be on the order of 1×10^{-9} m, which is much smaller than the diffusion layer thickness, for the overpotential range used in this study [29]. Therefore, any effect of the double layer formation on the model presented in Section 2, and the steady-state current densities obtained from Figure 5a–c, can be neglected. The comparison between double layer thickness and diffusion layer thickness can also be utilized to explain the negligible effect of migration compared to diffusion for the conditions used in this study. In general, diffusion dominates over migration at a given position and time, *t*, provided the following condition is satisfied [29]:

$$\xi \ll 2\frac{RT}{nF(2Dt)^{0.5}} \tag{25}$$

where ξ is the field strength, equivalent to the overpotential gradient, at the given position and time. The term on the right hand side of Eq. (25) is approximately 300 V/m at the maximum overpotential, η = –0.3 V, used in this work, and is larger for lower overpotentials. Though overpotential gradient in the double layer does not generally satisfy the condition of Eq. (25), this condition is held outside the double layer for the bath composition used in this study. Steady-state transport by combined migration-diffusion in a finite planar geometry has a closed-form solution only if all ions present have the same magnitude of charge (homovalent electrolyte). At this condition, for a concentration ratio of the supporting ion to the other ions of 0.4, the maximum potential drop in the region outside the double layer between the cathode and the anode is estimated as 0.014 V [48]. In the present study, the concentration ratio is 0.4 for the electrolyte solution of 1 M $CuSO_4$ and 0.5 M H_2SO_4, and is larger, with a corresponding smaller potential drop, for solutions with lower $CuSO_4$ concentrations. Although the electrolyte of $CuSO_4$ and H_2SO_4 is not homovalent, the value of 0.014 V obtained for the potential drop of a homovalent solution can provide a good quantitative estimate for the change of the overpotential between the cathode and the anode outside the double layer. Considering that the distance between the cathode and the anode is at least 0.07 m in this work, a very small potential gradient that satisfies Eq. (25) is expected. Moreover, for deposition on microelectrodes, an excess of supporting electrolyte is generally not that essential, especially at the lower overpotential magnitudes, since microelectrodes are almost free from ohmic polarization compared to regular electrodes [49].

Note that since the model assumptions described in Section 2 do not necessarily apply in the double layer, in this study, the concentration at the electrode surface, c_s, really refers to concentration outside the double layer. The two concentrations are very close as long as the thickness of the double layer is negligible compared to the diffusion layer thickness. This

condition is valid for overpotential magnitudes less than 0.3 V, as explained before. Furthermore, for the overpotential range used in this investigation, as mentioned previously in Section 2, negligible current is obtained from hydrogen evolution compared to that corresponding to the copper reduction. In fact, the upper limit on the overpotential range used in the present method for determining the kinetic parameters is primarily governed by the need to eliminate the effects of migration and hydrogen evolution, so as to simplify the analysis.

In order to evaluate surface concentration from Eq. (22), in addition to the steady state current density, i_∞, which is measured using a potentiostatic experiment, diffusion coefficient of the depositing ion in the electrolyte, *D*, should be obtained. In this work, time variation of the limiting current density is applied to determine diffusion coefficient using the method presented in the literature [35]. The maximum possible current density for the electrochemical system is called limiting current density; above this value, the current density remains constant with increasing overpotential and surface concentration of Cu^{2+} approaches zero. Shoup and Szabo [50] presented the following expression for the time variation of the limiting current density at a stationary finite disk electrode with a constant surface area in a quiescent solution:

$$i_L(\tau) = \frac{4nFDc_0}{\pi a}\left(0.7854 + 0.8862\tau^{-1/2} + 0.2146e^{-0.7823\tau^{-1/2}}\right) \quad (26)$$

with $\tau = 4Dt/a^2$. The steady-state current density at the limiting condition, $i_{L,\infty}$ is obtained from Eq. (26), for $t \to \infty$ as follows:

$$i_{L,\infty} = 0.7854\frac{4nFDc_0}{\pi a} \quad (27)$$

Substituting Eq. (27) into Eq. (22) results in the dimensionless surface concentration of 0.849. The 15% error in the dimensionless surface concentration compared to the expected value of 1 is due to

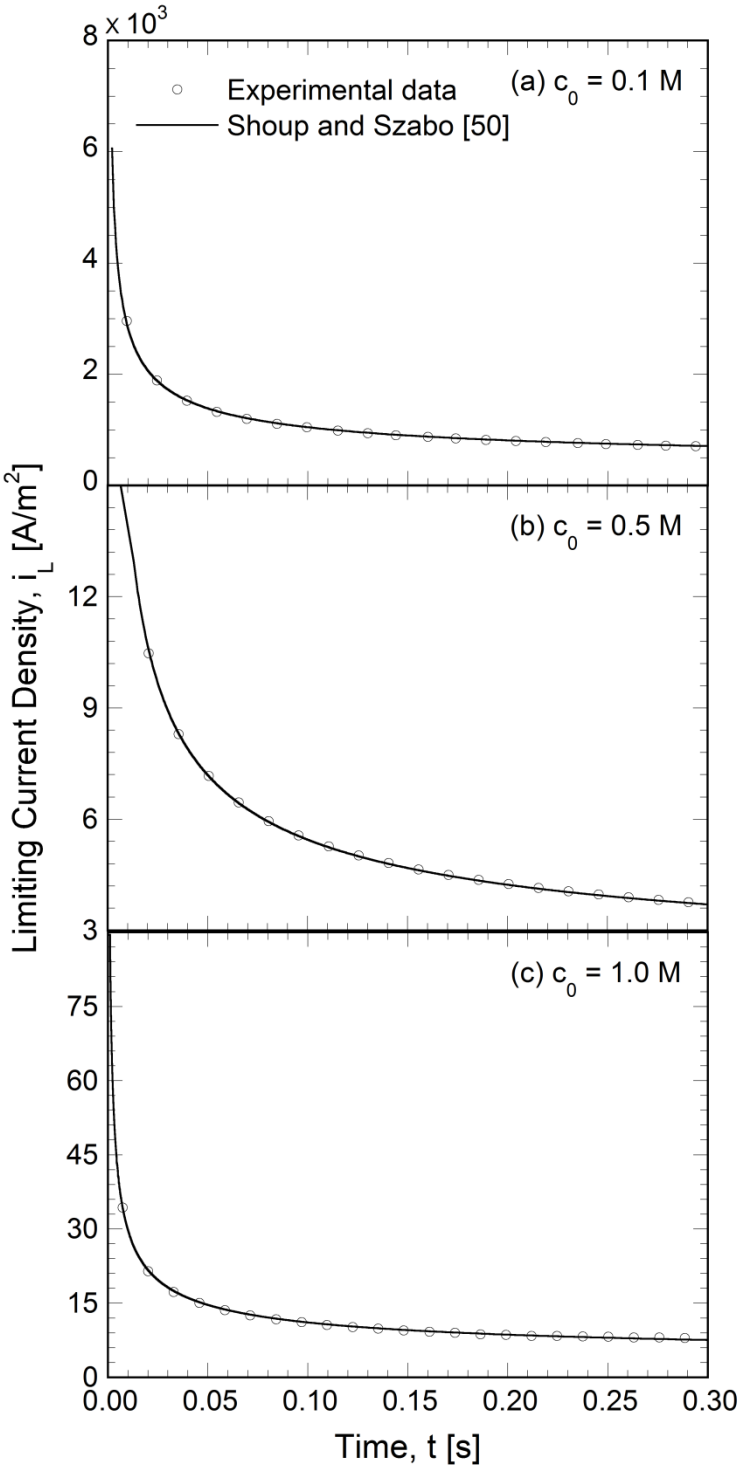

Figure 6: The variations of the limiting current density with time obtained from the potentiostatic experiment and shown by the discrete markers for the electrolytes of (a) c_0 = 0.1 M when overpotential of η = –0.5 V is applied, (b) c_0 = 0.5 M when overpotential of η = –0.7 V is applied,

and (c) c_0 = 1 M when overpotential of η = –0.8 V is applied. The solid lines show the time variations of the limiting current density obtained from Eq. (17) using the diffusivity of (a) D = $\mathbf{5.76 \times 10^{-10}}$ m^2/s, (b) D = $\mathbf{6.10 \times 10^{-10}}$ m^2/s, and (c) D = $\mathbf{6.31 \times 10^{-10}}$ m^2/s.

the effect of the migration mass transfer at high overpotentials in the limiting region. Regardless of this error, since diffusion coefficient is a weak function of the electrolyte concentration, the time variation of the limiting current density shown by Eq. (26) might be used to determine diffusion coefficients for the electrolytes with known $CuSO_4$ concentrations [35].

Note that, depending on the $CuSO_4$ concentration, the limiting value of the current density occurs at different overpotentials. Limiting current densities for the electrolytes with 0.1 M, 0.5 M and 1.0 M $CuSO_4$ concentrations were obtained by applying –0.5 V, –0.7 V, and –0.8 V overpotentials, respectively. Because of the high overpotentials used in the experiments, the surface curvature evolves very quickly and therefore, the surface area is close to the electrode initial area, πa^2, for only a short period of time. The variations of the limiting current density with time at this short period (t < 0.3 s) are shown by the discrete markers in Figure 6a–c for the electrolytes with 0.1 M, 0.5 M and 1.0 M $CuSO_4$ concentrations, respectively. The trust-region-reflective algorithm [51] was used to fit Eq. (26) to the experimental data on the limiting current density to determine the diffusion coefficient, D, for the electrolytes with different $CuSO_4$ concentrations. Based on this approach, diffusion coefficients of 5.76×10^{-10} m^2/s, 6.10×10^{-10} m^2/s, and 6.31×10^{-10} m^2/s are obtained for the electrolytes with 0.1 M, 0.5 M and 1.0 M $CuSO_4$ concentrations, respectively. The solid lines in Figure 6a–c show the time variations of the limiting current density obtained from Eq. (26) using the aforementioned values of the diffusion coefficients for the different electrolytes.

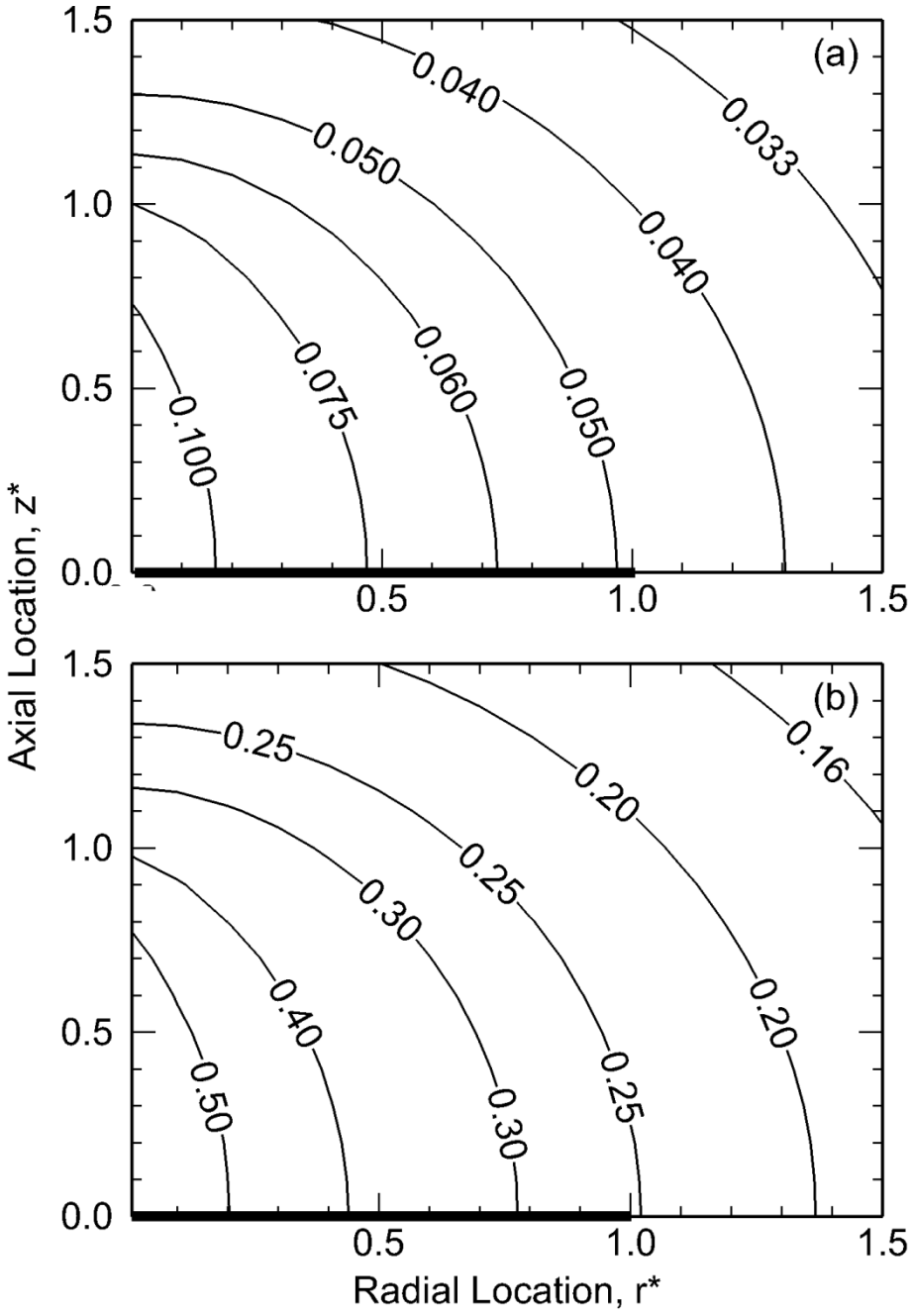

Figure 7: Contour of the dimensionless concentration in the bath with 1.0 M bulk concentration for overpotentials of η = (a) –0.1 V and (b) –0.3 V. The electrode surface lies on $z^* = 0$, for $0 < r^* < 1$, and is depicted by the thick lines in the figure.

Substituting the diffusion coefficient, D, and the measured steady state current density, i_∞, into Eq. (20), and evaluating the integral numerically, yields the dimensionless concentration profile, c^*, with respect to the dimensionless cylindrical coordinates, (r^*, z^*). Figure 7a and 4b present the concentration contours in the bath with 1.0 M bulk concentration for overpotentials of –0.1 V and –0.3 V, respectively. The electrode surface lies on $z^* = 0$, for $0 < r^* < 1$, and is depicted by the thick lines in Figure 7a and 4b. It is seen that the ion concentration increases, or equivalently, from Eq. (14), the dimensionless concentration decreases, in the direction of growth from a surface concentration, c_s, on the electrode surface to the bulk concentration, c_0, or $c^*(r^* \to \infty, z^* \to \infty) = 0$, at points far from the electrode. A comparison of Figure 7a and 4b further shows that the dimensionless surface concentration increases with increasing magnitude of the overpotential, implying that the ion concentration on the electrode surface decreases when a higher overpotential magnitude is applied. The difference between adjacent contour concentration values on the z^* axes of Figure 7a and 4b may be used to explain the effects of the overpotential on the concentration gradient in the bath. The concentration gradient is seen to be higher in Figure 7b for the larger overpotential magnitude compared to the gradient in Figure 7a, by a factor of approximately five. The effects of the overpotential on the concentration gradient and surface concentration may be attributed to its effect on the deposition rate which is higher at larger overpotential magnitudes.

Figure 8 displays the variation of the average electrode surface concentration, c_s, at steady state, with overpotential for three electrolytes with bulk concentrations, c_0, of 0.1 M, 0.5 M, and 1 M. The surface concentrations are obtained by substituting steady-state current densities, i_∞, from Figure 5 into Eq. (22). As inferred from the trends in Figure 7a–b, the average surface concentration decreases as the overpotential magnitude increases. At very low overpotential

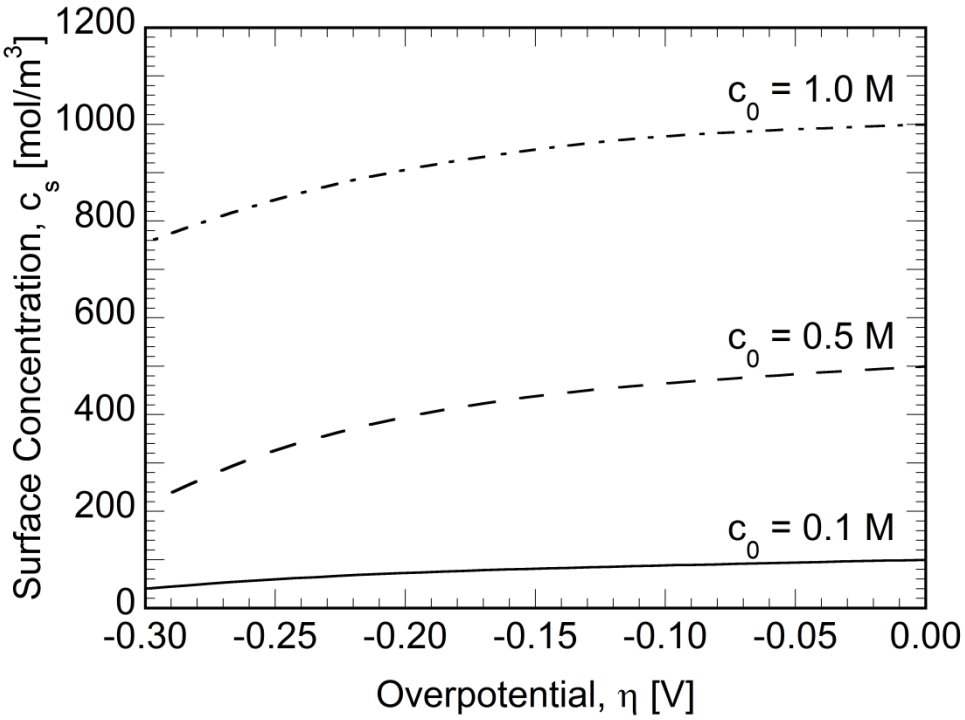

Figure 8: Variation of the average electrode surface concentration, c_s, at steady state, obtained from Eq. (13), with overpotential for three electrolytes with bulk concentrations, c_0, of 0.1 M, 0.5 M, and 1 M.

magnitudes, the change of the surface concentration with overpotential is negligible, and the average surface concentration asymptotically approaches the bulk concentration. At this condition, the mass-transfer rate is much faster than the rate of the electrochemical reaction, and the deposition process is mainly controlled by the kinetics of the electrochemical reaction. On the other hand, the surface concentration tends to zero at the higher overpotential magnitudes, as seen in Figure 8. At large overpotential magnitudes, the rate of deposition is so high that all the ions transferred to the electrode interface from the bath are immediately deposited on the surface. As a result, the concentration of the depositing ion on the electrode surface approaches zero and the current density approaches its limiting value. At the limiting condition, diffusion in the bath

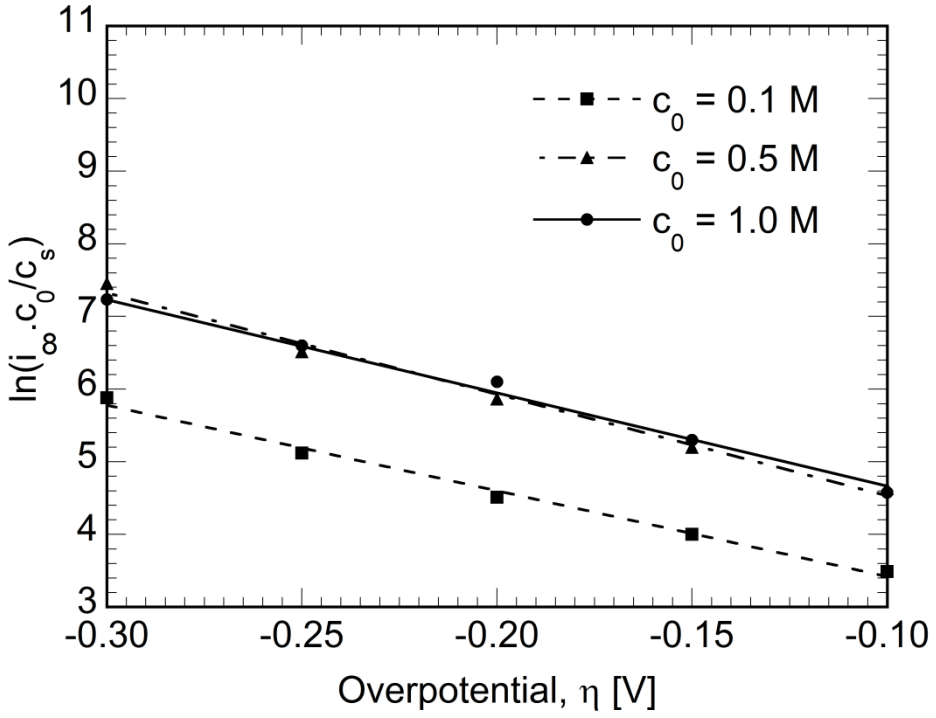

Figure 9: Linear variation of $\mathbf{ln}(\boldsymbol{i}_{\infty}.\frac{\boldsymbol{c_0}}{\boldsymbol{c_s}})$ with respect to η for the three electrolytes with bulk concentrations of 0.1 M, 0.5 M, and 1 M. The intercept and slope of the lines, respectively, correspond to $\ln(i_0)$ and $-\alpha F/RT$.

mainly controls the deposition process, and the effect of the reaction kinetics on the deposition rate is negligible. When the average surface concentration lies in between zero and bulk concentration, both mass transfer and kinetic effects are considered the controlling parameters.

The average surface concentration, c_s, obtained from Eq. (22), together with the steady state current density, i_{∞}, as discussed in Figure 5, may be used in Eq. (11) to determine the kinetic param-eters, i_0 and α. Taking the natural logarithm of Eq. (11), a linear relationship is obtained between $\ln(i_{\infty}.\frac{c_0}{c_s})$ with respect to η, such that the intercept and slope of this line, respectively, correspond to $\ln(i_0)$ and $-\alpha F/RT$. The intercept and slope values are, in turn, utilized to determine the kinetic parameters, i_0 and α. Figure 9 presents the measured steady state current density for the

various overpotentials, η, and for the three electrolytes with bulk concentrations of 0.1 M, 0.5 M, and 1 M, in terms of the variation of $\ln(i_\infty.\frac{c_0}{c_s})$ with respect to η. It is evident that (a) the variation is linear with a negative slope, (b) the variation is significant for c_0 = 0.1 to 0.5 M, but less so for c_0 = 0.5 to 1.0, and (c) the slopes are almost similar, although with different intercepts.

The exchange current densities (i_0), determined as the exponential of the intercepts of these lines on the vertical axis, and the transfer coefficients (α), obtained from the slopes of the lines, are presented in Table 1 (columns 2 and 3) as a function of the bulk concentration, c_0 (column 1). Note that the exchange current density is zero in a blank electrolyte, in which the concentration of the depositing ion is zero. As Figure 9 shows, the slopes of the lines corresponding to different bulk concentrations are almost similar, while the intercept of the line corresponding to a higher bulk concentration is larger. Consequently, electrolyte concentration has no significant effect on transfer coefficient, whereas the exchange current density increases with increasing bulk concentration, in agreement with the trend reported in the literature [29]. These effects of the bulk concentration on the transfer coefficient and exchange current density serve to validate the results shown in Table 1. For the lowest overpotential magnitude applied in this study, η = –0.1 V, substituting the transfer coefficients shown in the third column of Table 1 and surface concentrations obtained from Figure 8 in the first and second terms of Eq. (10) results in the respective values of 3 and 0.001. The difference between these two terms is larger at higher overpotentials. Therefore, in this work, the second term is appropriately neglected compared to the first term and as explained before, Eq. (11) is replaced with Eq. (10) in the model.

The values of the transfer coefficient in column 3 of Table 1 are nearly constant, varying in a narrow range of 0.30 to 0.35. This suggests that the transfer coefficient may be considered to be fixed at an average value of α^* = 0.33 and the corresponding exchange current density, i_0^*, may be

determined through linear regression fit of the data in Figure 9 with a slope of $-\alpha^* F/RT$ and evaluating the exponential of the intercepts on the vertical axis. The exchange current densities, i_0^*, corresponding to the constant transfer coefficient, α^*, of 0.33 are shown in column 4 of Table 1 for the different bulk concentrations, c_0.

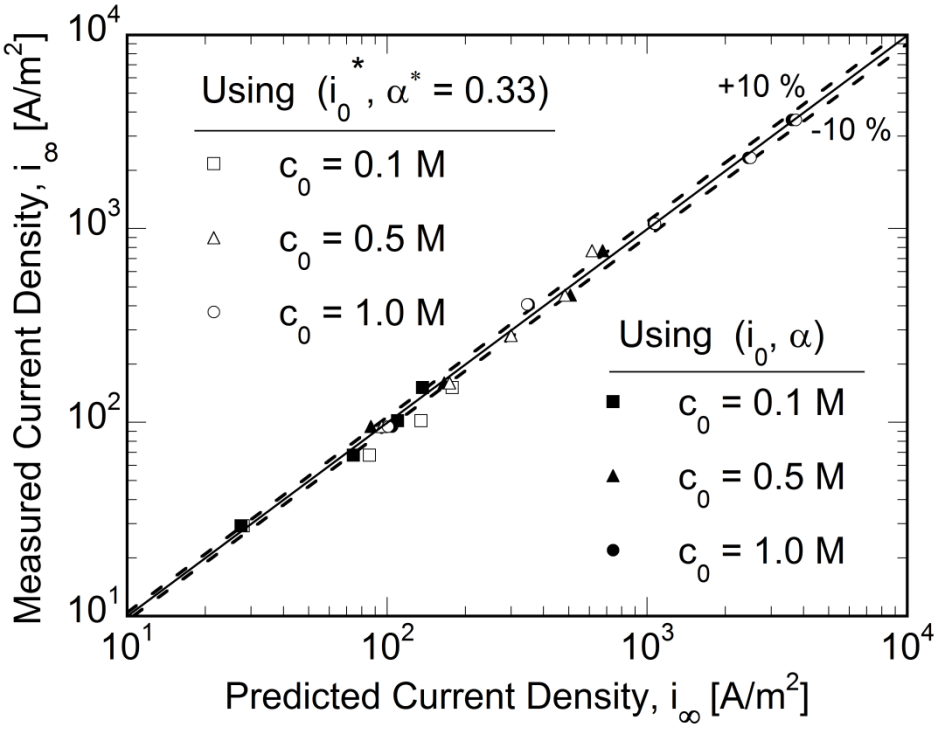

Figure 10: Comparing the predicted and measured values of the steady state current density for the different overpotentials and for the electrolyte bulk concentrations of 0.1 M, 0.5 M, and 1 M. The solid line diagonal to the plot frame represents the line of exact agreement while the dashed lines above and below this line are the ±10% error bands. The filled markers denote the predictions for the i_0 and α combinations, columns 2 and 3 of Table 1, whereas the open markers represent the predicted steady state current density using the i_0^* from column 3 of Table 1 and $\alpha^* = 0.33$.

The accuracy of the kinetic parameters is evaluated by comparing the steady state current densities obtained using the (i_0, α) and (i_0^*, α^* = 0.33) combinations from Table 1 in Eq. (11) to obtain the current densities predicted by the model with the measured values of i_∞ from Figure 5 for the different overpotentials and for the electrolyte bulk concentrations of 0.1 M, 0.5 M, and 1 M. Figure 10 presents the comparison of the measured steady state current density with the predicted values for all the cases studied. The solid line diagonal to the plot frame represents the line of exact agreement while the dashed lines above and below this line are the ±10% error bands. The filled markers denote the predictions for the i_0 and α combinations columns 2 and 3 of Table 1, whereas the open markers represent the predicted steady state current density using the i_0^* from column 3 of Table 1 and α^* = 0.33. In each case, the three different marker shapes denote the different bulk concentrations studied. Overall, Figure 10 shows that the agreement is very good over the three decades of current density values depicted in the plot. Of all the cases presented in the plot, the agreement is to within 10% in all but four of them. The comparison demonstrates that the use of a constant transfer coefficient and i_0^* as a single parameter in the model [Eq. (11)] is adequate to represent the microelectrode kinetics accurately.

Chapter 3: Numerical Analysis of Electrodeposition in Microcavities

Electrodeposition in sacrificial polymeric micromolds is an important step in processes such as LIGA, an acronym for the German words for lithography, electroforming and molding, for fabricating metallic microstructures. This paper investigates electrodeposition in microcavities with a conducting base and plastic features that provide insulating sidewalls for fabrication of the desired metallic micropart. Computational models for the governing transport and electrochemical phenomena are used to simulate the evolution of the electrodeposition front and the spatial current density profiles with time. The effects of the applied voltage and micromold geometry are systematically studied for their influence on the resulting electrodeposition rate and uniformity of the deposition front. Conditions that lead to desirable process and part quality are derived from the studies.

3.1 Introduction

Electrodeposition of a metal or alloy onto a surface that has been patterned by lithographic techniques plays an important role in the fabrication of metallic microstructures using techniques such as LIGA [3]. Usually patterns with micron or submicron dimensions are made on a layer of photoresist spread over a thin conducting seed layer. The pattern acts as an electroforming mold with a conducting base and insulating walls such that the metal electrodeposition originates from its conducting base and grows conforming to the micromold geometry with excellent feature and dimensional fidelity. This approach produces a metallic microstructure that is negative in feature with respect to the micromold and can be either used directly for different applications or placed as

a mold insert in a plastic molding process for the replication of the primary structure in large quantities and low cost [2-5]. The electroforming part of the LIGA process consists of electrodeposition in recessed microcavities and microtrenches, which forms the focus of the present study.

One distinctive aspect of electrodeposition in microchannels is the nonuniform distribution of current density on the electrode surface, which depends on the feature geometry. Chang et al. [52] experimentally studied the effects of the mold feature size on the plating rate, and reported that at low aspect ratios, mold cavities with smaller openings have higher current densities and, in turn, higher plating rates. Nonuniform current density results in thicker deposits along the edges of the microcavity opening than that in the central part away from the edges. This was attributed to the collection of additional current along trench edges from the area above the insulating resist material, while the central part of the trench receives current only from the cell area above it [53].

In addition to the kinetic reaction on the electrode surface, electrodeposition involves in a mass transfer process through the electrolyte by diffusion, convection or ion drift. Process may be mainly controlled by mass transfer or electrode kinetics based on the applied voltage and level of the mixing in the bath. For a well-mixed bath usually mass transfer effect is negligible comparing to the electrode kinetics; and current distribution, referred to as the secondary current distribution, is found by solving Laplace equation of the potential field considering uniform ion concentration in the bath [54, 55]. Based on the geometry of the system, uniform bath concentration may not be an acceptable assumption for electrodeposition through microtrenches. Less intensity of the mixing induced convective mass transfer in microelectrodes, reported by different authors [15, 56-58], suggests that diffusion and ion drift as the slower mass transfer mechanisms comparing to

convection may play role in addition to the kinetic effect in the electrodeposition through microtrenches.

Hume et al. [53] presented a model for a mass transfer controlled process by ignoring the contribution of the electrode kinetics. Based on their model, deposit characteristic like distribution of current density are independent of the applied voltage. In reality this happens when voltage is larger than a limiting value corresponding to the limitation on the rate of ion diffusion to the electrode. When applied voltage is larger than this limiting value, ion concentration on the electrode surface is zero and increasing the applied voltage further (in magnitude) will not increase the current density and deposition rate further. Electrodeposition by applying a voltage lower than the limiting value, which is the typical condition [57], is studied in the current work in which voltage is one of the main controlling parameters.

In addition to its lateral variation, the current density varies with time as the microtrench fills gradually, which results in each deposition layer having a different plating rate. These variations of the current density and deposition rate translate to a variation of the mechanical properties (e.g. Young's modulus, stress level and hardness). Yeh et al. [59] studied the effects of current density on the nanomechanical properties of Ni-Fe mold insert and found that higher current densities resulted in finer grains of the Ni-Fe alloy, which exhibited higher hardness. For specific mold geometry, therefore, it is desirable to have a uniform plating rate during electrodeposition so as to obtain uniform mechanical properties. Lateral uniformity of the current density also causes a flat deposition front and decreases the amount of overplating at the end of the electrodeposition process. Relatively few investigations are found in the open literature on the effects of process parameters on the extent of overplating. Guo et al. [60] modeled metal growth across the top of the

resist mold, but didn't study the effects of the bath conditions and microcavity geometry on overplating.

The goal of the present study is to present a systematic investigation of the effects of the applied voltage and microtrench geometry on the electrodeposition rate (equivalently electrodeposition time) and the extent of nonuniformity of the electrodeposition resulting in an overplating at the end of the microtrench filling process. In the present study, a complete model for electrodeposition in microcavities is developed by considering ohmic and mass transfer effects, and using an arbitrary Lagrangian-Eulerian (ALE) formulation coupled with repeated re-meshing and re-mapping technique [16] to track the entire transient deposition process. The effects of the microcavity and bath geometry and applied potential on overplating and fill time are investigated using a transient model for the evolution of surface during electrodeposition process. The effects of applying constant and time-varying voltage at the cathode is studied, and based on the results, optimum voltage is derived as a function of the microtrench geometry. The article is organized as follows: The mathematical modeling and the numerical simulation procedure are described in the next section, followed by a presentation and discussion of the results of the study.

3.2 Mathematical Model

Figure 11 shows a schematic of the two-dimensional rectangular microtrench geometry of width, W, and height, H, and the electrodeposition bath of height, H_b, and width outside of the microtrench, L_b, considered in the study. As shown in the figure, the anode with reference voltage $V = 0$ V, covers the entire top surface of the bath and the cathodic deposition surface is considered to be at the bottom surface of the trench, where a constant voltage $V = -V_0$ is applied during the

electrodeposition process. All other surfaces shown by the hatched lines in the figure are insulated representing either a wall or a line of symmetry. The origin of the coordinate system is positioned coincident with the center of the top surface of the trench, as indicated in Figure 11. By virtue of symmetry of the geometry domain and the applied boundary conditions, only one half of the domain on one side of the axis of symmetry is considered for the modeling.

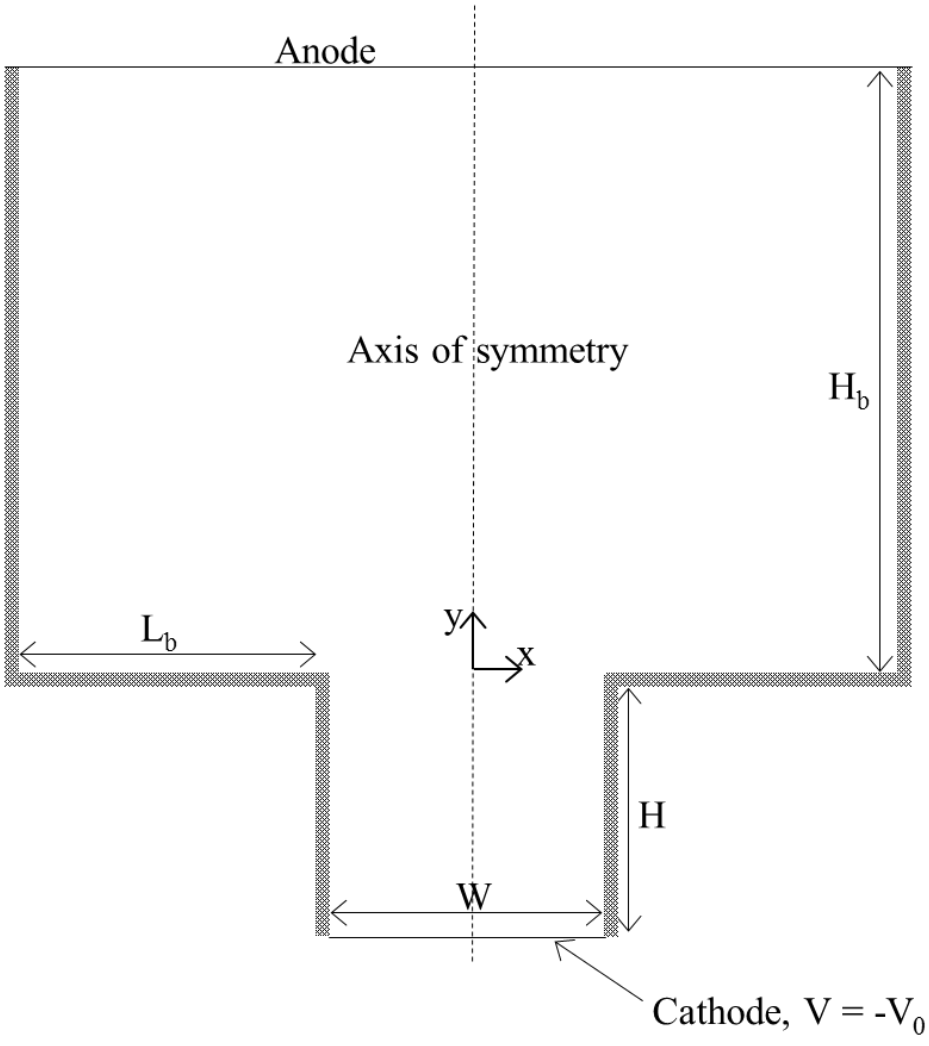

Figure 11: Schematic of the modeling domain considered in the study.

The electrolyte system considered is a nickel sulfate bath consisting of Ni^{2+} and SO_4^{2-} ions and H_2O as a solvent. Nickel reduction $Ni^{2+} + 2e^- \rightarrow Ni$ was considered as a single cathodic reaction. Moreover, homogeneous reactions occur in the electrolyte bath, of which the reaction $Ni^{2+} + OH^- \rightarrow Ni(OH)^+$ could potentially affect the nickel ion concentration. However, in this investigation, the bath pH was assumed to be maintained below 4, for which the concentration of $Ni(OH)^+$ and the corresponding concentration change of Ni^{2+} due to its production is negligible and is not considered in the analysis [16]. Furthermore, diffusion coefficient and electrode kinetic parameters were treated to be constant in this modeling and the anode was assumed to be unpolarized with no change in shape during the process.

The goal of the modeling is to predict the species concentration distribution and the current density distribution in the bath so as to obtain the evolution of the deposition surface with time during the process, from which the microtrench fill time and the overplating amount can be determined. Since the physical domain for the computation changes with time along with the moving electrodeposition front, a moving mesh scheme is used for the solution. The problem formulation and solution scheme are discussed in the following subsections.

3.2.1 Model Formulation

The transport and mass balance of dissolved species, Ni^{2+} and SO_4^{2-}, are governed by:

$$\frac{\partial c_i}{\partial t} + \nabla . N_i = r_i \quad , \qquad i = 1, 2 \tag{28}$$

where c_1 is the concentration of Ni^{2+} and c_2 is the concentration of SO_4^{2-}, r_i is the homogeneous reaction rate for each species which can be neglected since the pH of the bath is below 4 [16], N_i is

the total mass flux vector of the ionic species *i*, composed of three separate terms denoting for the diffusion, electromigration and convection flux as follows:

$$N_i = -D_i \nabla c_i - z_i u_{mi} F c_i \nabla \phi + c_i u \tag{29}$$

in which u_{mi} and $\phi\phi$ in the electromigration term stand for ion mobility and bath potential, respectively, where the former is usually approximated as $u_{mi} = \frac{D_i}{RT}$ [15]. In this work, the convective effect, the third term on the right hand side of Eq. (29), is neglected by considering zero velocity, *u*, for the bath fluid. Based on the assumptions mentioned and using the definition of N_i given by Eq. (29), Eq. (28) can be written as

$$\frac{\partial c_i}{\partial t} + \nabla.(-D_i \nabla c_i - z_i u_{mi} F c_i \nabla \phi) = 0 \tag{30}$$

Moreover, electroneutrality of the bath is governed by the following relationship:

$$\sum_{i=1}^{2} z_i c_i = 0 \tag{31}$$

Multiplying Eq. (30) by $z_i F$ and then summing over the two species, it follows that:

$$F \sum_{i=1}^{2} z_i \frac{\partial c_i}{\partial t} + \nabla.\left(F \sum_{i=1}^{2} (-z_i D_i \nabla c_i - z_i^2 F u_{mi} c_i \nabla \phi) \right) = 0 \tag{32}$$

By taking the time derivative of the electroneutrality condition, Eq. (31), it can be shown that the first term in Eq. (32) is zero and the conservation of electric charge is obtained as:

$$\nabla.\left(F \sum_{i=1}^{2} (-z_i D_i \nabla c_i - z_i^2 F u_{mi} c_i \nabla \phi) \right) = 0 \tag{33}$$

Equations (30) and (33) represent formulations of the Nernst-Plank model for finding three unknowns in the electrodepositing process: the electric potential of the bath, ϕ, concentration of Ni^{2+}, c_1, and concentration of SO_4^{2-}, c_2.

The system of equations is solved subject to the following boundary conditions: (a) along the anode surface, molar concentration of Ni^{2+} is fixed at its initial values (c_0 = 0.00126 mol/cm^3) and the electric potential is set to zero to establish its datum; (b) insulated conditions are applied along the symmetry boundary, side walls of the bath and microtrench and on the bottom surface of the bath; and (c) along the moving cathodic deposition surface at the bottom of the microtrench, nickel reduction flux and normal current density are calculated using following equations:

$$J_{Ni} = k_{Ni} c_{Ni}^{\beta_{Ni}} [e^{\alpha_{a,Ni}\frac{F}{RT}(-V_0-\phi-U_{0,Ni})} - e^{-\alpha_{c,Ni}\frac{F}{RT}(-V_0-\phi-U_{0,Ni})}] \quad (34)$$

$$i = z_{Ni} F J_{Ni} \quad (35)$$

Equation (34) is the Butler-Volmer kinetic expression in which k_{Ni}, β_{Ni}, $U_{0,Ni}$, $\alpha_{a,Ni}$ and $\alpha_{c,Ni}$ are, respectively, the rate constant, reaction order, thermodynamic open-circuit potential, anodic and cathodic transfer coefficients, all assumed to be constant during the process. In Eq. (34), V_0 is the magnitude of the external voltage applied to the cathodic deposition surface. Model formulation described above using Nernt-Plank formulation is the basis of other electrochemical systems as well like polymer electrolyte fuel cells [61, 62]

3.2.2 Moving Mesh Formulation

The moving computational domain during electrodeposition was modeled using the arbitrary Lagrangian-Eulerian (ALE) method [63] which is briefly outlined here. If $x(\tau)$ is considered as the points of the reference domain at time τ, while the points of the moving domain at a later time t are denoted by $x(t)$ then it is possible to associate a trajectory to each point $x(\tau)$ of the domain at time τ according to

$$x(t) = \varphi_\tau(x(\tau), t) \quad (36)$$

where $\varphi_\tau(x(\tau), t)$ is the mapping function from the domain points at time τ to the same points at a later time, *t*. The domain velocity, v, is defined as the time derivative of $x(t)$ as:

$$v(x(\tau), t) = \dot{x}(t) = \frac{\partial}{\partial t}\varphi_\tau(x(\tau), t) = \frac{\varphi_\tau(x(\tau), t) - \varphi_\tau(x(\tau), \tau)}{t - \tau} + O(t - \tau) \quad (37)$$

from which, omitting the error term $O(t - \tau)$ and using Eq. (36), a linear approximation for φ_τ is obtained as follows:

$$\varphi_\tau(x(\tau), t) = x(\tau) + (t - \tau)v(x(\tau), \tau) \quad (38)$$

Knowing the domain velocity and coordinates at time τ, Eq. (38) can be used to find domain coordinates at a later time *t.* Further, the normal velocity of the deposition front is related to the rate of nickel ion reduction at the cathode surface, J_{Ni} (Eq. (34)), as follows:

$$n.v = \frac{M_{Ni}}{\rho_{Ni}} J_{Ni} \quad (39)$$

where M_{Ni} and ρ_{Ni} are nickel atomic mass and deposit density respectively.

The moving mesh formulation given by Eqs. (36)–(38) is subject to the following boundary conditions: (a) the mesh displacement along the left and right side walls of the trench and bath was fixed to be zero in the *x* direction; (b) the mesh displacement along the bottom surface of the bath was fixed to be zero in the *y* direction; (c) the mesh displacement was restricted in both *x* and *y* directions along the top boundaries of the microtrench or bath based on different steps of the solution which are explained in section 2.3 below; and (d) along the moving deposition surface, the normal velocity is obtained from Eq. (39). Equations (36)–(38) describe the main formulation of the arbitrary Lagrangian-Eulerian method. If the mesh displacement becomes large and the mesh quality degrades at any instant during the computations, the domain is re-meshed and all solution variables are mapped from the old mesh to the new one, and this process is continued until

the microtrench is filled. Equation (39) is used to couple the Nernst-Plank formulation, Eqs. (30) and (33), and the moving mesh formulation, Eq. (38).

3.2.3 **Method of Solution**

Finite element analysis implemented in COMSOL 3.5a is used to solve model formulation described above. In this analysis, Galerkin method is used to convert a continuous operator problem (such as a differential equation) to a weak formulation. From the calculus of variations, it can be shown that the functions that satisfy the variational equations also satisfy the differential equations and their boundary conditions.

An initial concentration, c_0 = 0.00126 mol/cm^3, was considered for both Ni^{2+} and SO_4^{2-} ions. For a bath temperature of 40 °C, the other parameters used in the computations were: $k_{Ni} = 0.0001\ cm/s$, $\beta_{Ni} = 1$, $U_{0,Ni} = -0.22\ V$, $\alpha_{a,Ni} = \alpha_{c,Ni} = 0.21 \alpha_{a,Ni} = \alpha_{c,Ni} = 0.21$ and $D_1 = D_2 = 10^{-5}$ cm^2/s [16]. The computations were performed in two different steps: in the first step, structured and unstructured rectangular mesh was used to discretize the microtrench and the bath domain, respectively. For reducing computational cost, moving mesh formulation was solved only in the microtrench and a fixed mesh structure was considered in the bath. In this step, mesh displacement was restricted in both *x* and *y* directions along the top boundary of the microtrench. The solution was stopped when the microtrench was about to fill and a new geometry was created from the deformed mesh and the final solution from the first step was mapped to the new geometry. For the second step, a triangular moving mesh was used for the domain discretization and unlike the first step, restricted movement in *x*- and *y*-directions was applied along the top

boundary of the bath. Gradual mesh refinement was performed for both steps to make the results independent of the mesh refinement.

The outputs of the simulations were the spatial current density variation with time, the concentration profiles of the species with time, and the evolution of the deposition surface with time during the process. The process model developed in this section is used to conduct systematic parametric studies as discussed in the next section

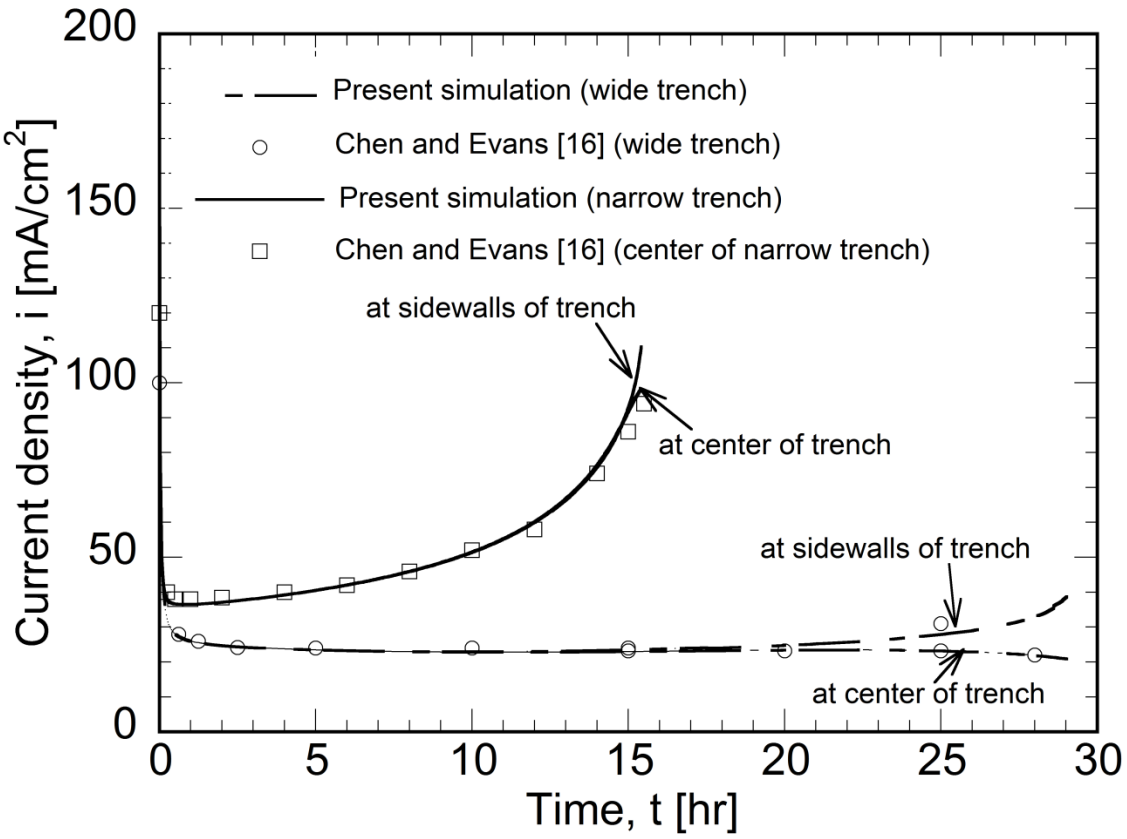

Figure 12: Validation of the present numerical simulation with the results of Chen and Evans [16] for an applied voltage magnitude V_0 = 0.6 V.

3.3 Results and Discussion

The numerical model was validated with the computational results of Chen and Evans [16] on electrodeposition in 1 mm × 1 mm (wide) and 1 mm × 0.2 mm (narrow) trenches, with an applied potential at the cathode, V_0 = –0.6 V. Figure 12 presents a comparison on the current density at the center and sidewalls of the trench as a function of time during electrodeposition. The lines in the plot denote results of the present simulation, while the markers correspond to the data reported in ref. [16]. For the case of the narrow trench, the electrodeposition is completed in about 16 h, and the current density is spatially uniform that the curves for the centerline and the sidewall locations are mutually indistinguishable. For the deposition in the wider trench, the current density variation is seen to be spatially nonuniform, with a higher value toward the sidewalls, that is particularly evident near the end of the process. Figure 12 further shows the effect of the trench geometry on the current density in microelectrodeposition process, that trenches with smaller openings have higher current densities and are accompanied by a higher plating rate. In all cases, the present simulations are seen to be in close agreement with the results of Chen and Evans [16].

Table 1: Trench geometry and maximum applied potential in the cases studied.

Case	H [μm]	W [μm]	$V_{0,max}$ [V]
1	1000	100	0.65
2	500	100	0.75
3	100	100	0.80
4	100	250	0.85
5	100	500	0.75

Based on the validated computational model, parametric studies were conducted to investigate the influence of the applied voltage, the microtrench geometry and the trench spacing on the current density and the deposition rate with time as well as the extent of overplating at the end of the process. The effect of external voltage was studied by considering two different trends for V_0— a constant voltage with time and a time-varying voltage cycle consisting of a hold-and-ramp pattern described later in this section. The effect of the microtrench geometry was studied by varying the trench height (H) and trench width (W), while keeping the bath dimensions, L_b and H_b, constant at 500 μm and 1 cm, respectively. For studying the effect of trench spacing, the model was solved for different L_b for a constant microtrench geometry and external voltage.

Table 1 summarizes the five cases studied on the effects of the microtrench geometry and the applied constant voltage V_0. As seen in the Table, the microtrench aspect ratio (H/W) ranges from 0.2 to 10, and for each geometry, a maximum possible voltage (magnitude), $V_{0,max}$, is also listed in Table 1 based on consideration of the limiting current density, corresponding to the limitation on the rate of diffusion of nickel to the electrode; increasing the applied voltage further (in magnitude) will not increase the current density and deposition rate further. As the voltage approaches a value corresponding to the limiting current, instabilities were observed in the electrodeposition front and in the computational solution, due to an underlying physical instability of the deposition process as also noted by Hume et al. [53]. The maximum voltage, $V_{0,max}$, in Table 1 represents the largest applied voltage that yielded a stable solution just prior to incipient instabilities. Since ion diffusion in deep and narrow trenches with high aspect ratio is more difficult, these geometries are seen to have a smaller magnitude of $V_{0,max}$ in Table 1. Furthermore,

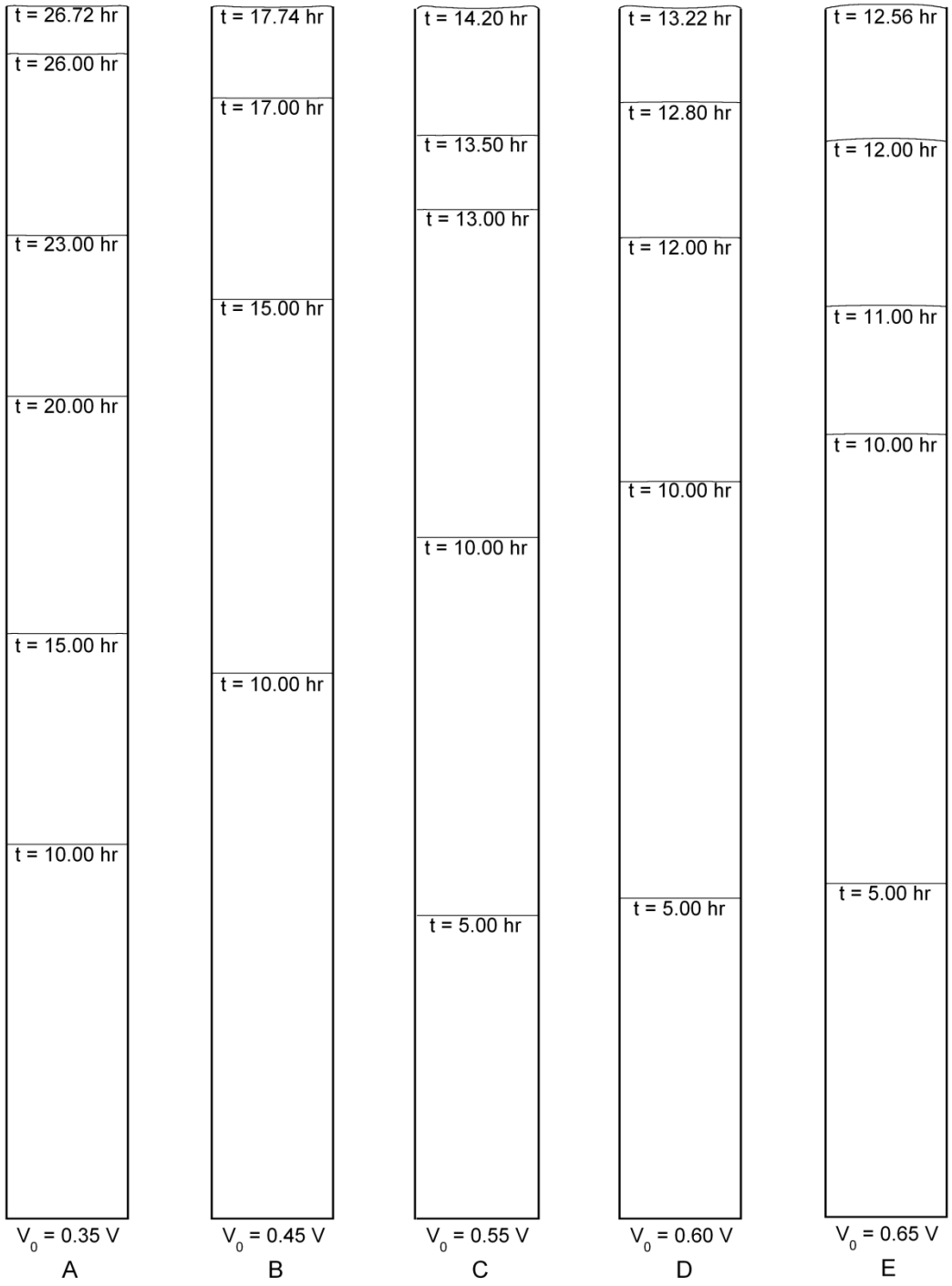

Figure 13: Time evolution of the electrodeposition front in a cavity of W = 100 μm and H = 1000 μm, for applied voltage (magnitude) of (a) 0.35, (b) 0.45, (c) 0.55, (d) 0.60, and (e) 0.65 V.

a rapid consumption of the nickel ions at the microtrench sidewalls limits the maximum voltage for the trenches with very small aspect ratio (*H/W*), as evident by sudden decrease of $V_{0,max}$ for *H/W* = 0.2, Case 5, in Table 1. The studies were performed for each geometry by considering 5 different applied voltage values, V_0, such that $V_{0,max}$–V_0 = 0.0, 0.05, 0.1, 0.2 and 0.3.

The time-evolution of the electrodeposition front for filling a trench of width, *W* = 100 μm, and height, *H* = 1000 μm (Case 1 in Table 1), at five different applied voltages, is shown in Figure 13A–E. For all voltages, the process starts with a flat deposition front and then proceeds to form curved surfaces corresponding to the variation of current density across the microtrench width. The simulation was carried out until the trench filled completely across the entire width of the trench. Since the current density is not uniform across the width, the deposition rate and the deposition front are correspondingly nonuniform. As a result, a certain extent of overplating is necessary in each of the cases, to achieve complete cavity fill. The times shown below the topmost electroplating front in Figure 13A–E are the fill times, including the overplating. Increasing the magnitude of the applied voltage reduces the fill time (from 26.72 hr for V_0 = 0.35 V to 12.56 hr for V_0 = 0.65 V) due to an increase in the average current density, but leads to an enhanced surface curvature and overplating amount, owing to the greater nonuniformity in the current density variation at the higher magnitudes of the applied voltages.

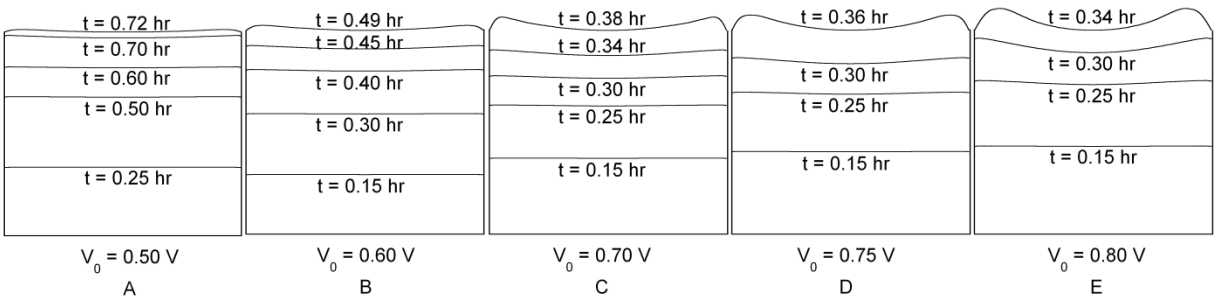

Figure 14: Time evolution of the electrodeposition front in a cavity of *W* = 100 μm and *H* = 100 μm, for applied voltage (magnitude) of (a) 0.50 V, (b) 0.60 , (c) 0.70 , (d) 0.75 , and (e) 0.80 V

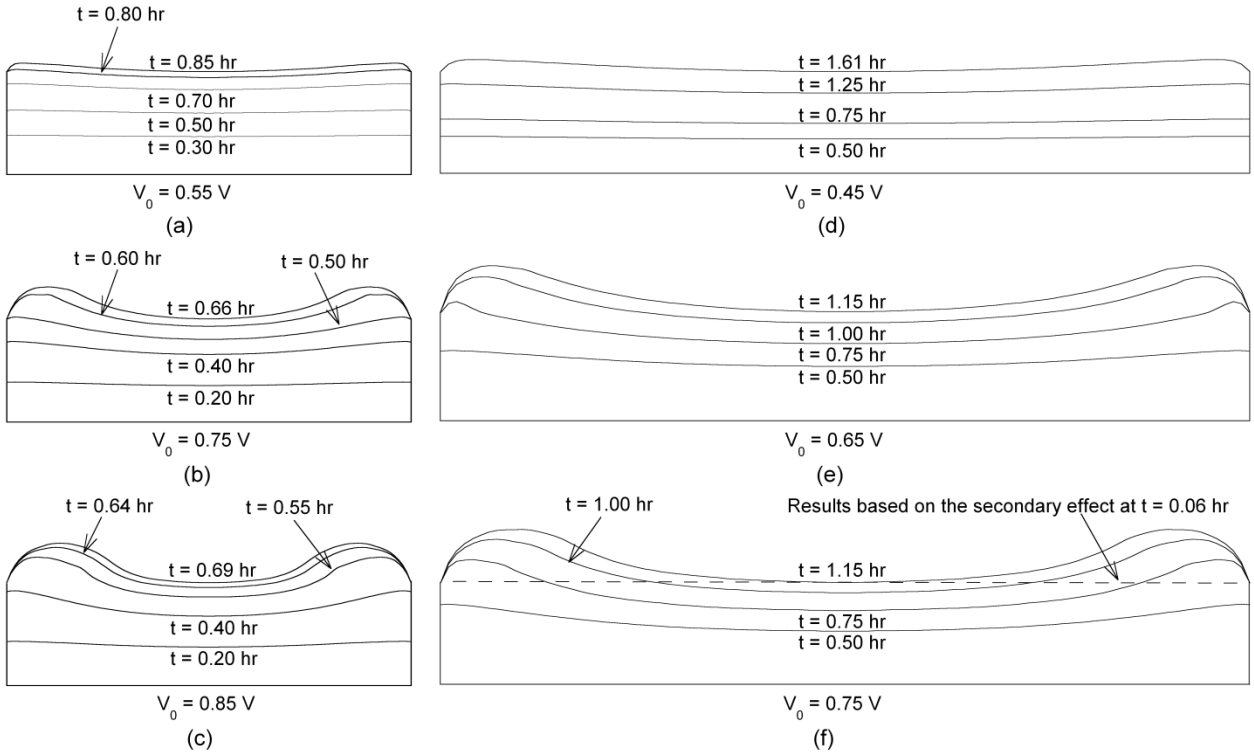

Figure 15: Time evolution of the electrodeposition front in a cavity of W = 250 μm and H = 100 μm, for applied voltage (magnitude) of (a) 0.55 V, (b) 0.75 V, (c) 0.85 V, and in a cavity of W = 500 μm and H = 100 μm, for applied voltage (magnitude) of (d) 0.45 V (e) 0.65 V, and (f) 0.75 V, dashed line shows the profile of the electrodeposition front based on the secondary effect at fill time corresponding to 0.06 hr.

Figure 14A–E show the evolution of the electrodeposition front in a square microtrench of W = H = 100 μm (Case 3 in Table 1), for five different magnitudes of the applied voltage. Once again, the fill time is seen to decrease with increasing voltage magnitude at the cathode, as in Figure 13; however, the nonuniformity of the electroplating front is amplified in this case relative to Figure 13. This suggests that trenches with smaller height have a more nonuniform current density across the trench width, which leads to a more curved deposition front. The fill time is seen to decrease

considerably as the applied voltage magnitude is increased from 0.50 V to 0.70 V, but is relatively less influenced by the voltage for values greater than 0.70 V in magnitude.

Figure 15A–C show the deposition front growth with time in a microtrench of W = 250 μm and H = 100 μm (Case 4 in Table 1), for V_0 = 0.55 V, 0.75 V, and the maximum voltage, $V_{0,max}$ = 0.85 V, respectively, and Figure 15D–F present the evolution of the deposition front in a microtrench of W = 500 μm and H = 100 μm (Case 5 in Table 1), for applied voltages of 0.45 V, 0.65 V and the maximum value of 0.75 V, respectively. Following similar trends as in Figure 13 and Figure 14, increasing the applied voltage is seen to produce considerably nonuniform deposition fronts. Comparing Figure 14 and Figure 15, all of which share a common microtrench height but differ in the trench width, it is seen that the nonuniformity of the electrodeposition front as well as the extent of overplating at the end of the fill increase with the microtrench width. In general, the onset of a nonplanar deposition front is observed to be relatively sooner in the process as the microtrench aspect ratio (H/W) decreases, which results in an increased surface curvature at the end of fill. It is also seen from Figure 14D, Figure 15B and Figure 15F, with the same applied voltage of 0.75 V, that the fill time increases with increasing trench width. Figure 15D–F reiterate the observation in Figure 14 that the fill time decreases considerably with increasing voltage initially, but remains relatively less influenced by the voltage for the larger voltage magnitudes; for example, in Figure 15E and Figure 15F, although the voltage is increased from 0.65 V to 0.75 V, the fill time remains about 1.15 h. Figure 15A–C show that the fill time initially decreases with increasing voltage [Figure 15C and Figure 15B] but increases with further increase of the voltage [Figure 15B and Figure 15C]. This demonstrates the conflicting effect of the voltage on the filling time; on the one hand, increasing the magnitude of the applied voltage tends to decrease fill time but on the other hand, it increases surface curvature and, in turn, the overplating time.

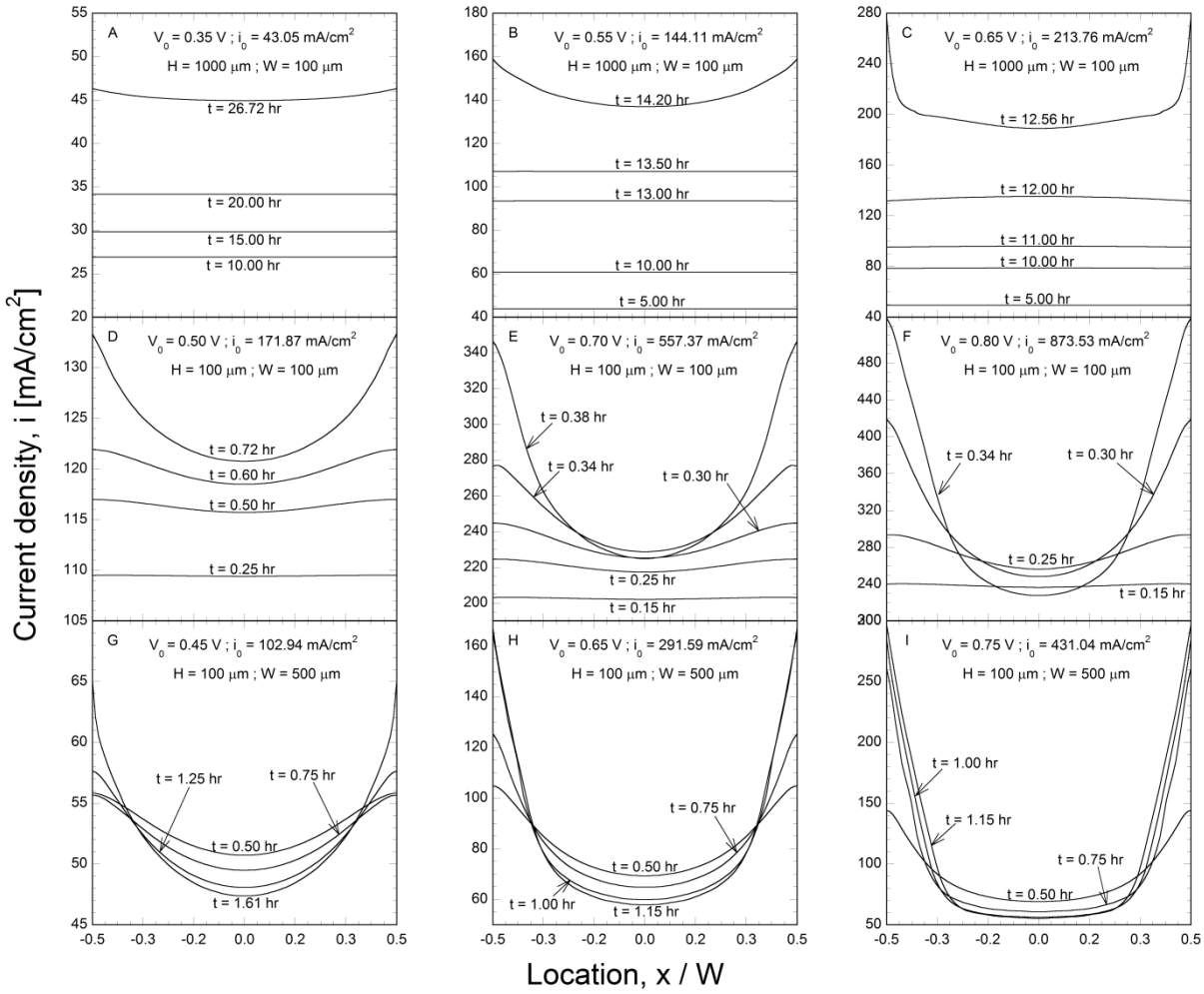

Figure 16: Variation of the current density across the microtrench width at various times during the electrodeposition process for W = 100 μm, H = 1000 μm, and magnitude of V_0 = (a) 0.35 V, (b) 0.55 V and (c) 0.65 V; for W = 100 μm, H = 100 μm and magnitude of V_0 = (d) 0.50 V (e) 0.70 V and (f) 0.80 V; and for W = 500 μm, H = 100 μm and magnitude of V_0 = (g) 0.45 V (h) 0.65 V and (i) 0.75 V.

Figure 6 presents the local current density variation across the microtrench width at various times during the deposition process and for three different applied voltage values as indicated in

the plots, for W = 100 μm and H = 1000 μm [Figure 16A–C], W = 100 μm and H = 100 μm [Figs. 6D–F] and W = 500 μm and H = 100 μm [Figure 16G–I]. For each microtrench geometry, the highest voltage presented corresponds to its respective maximum possible voltage, $V_{0,max}$, and the other two voltages presented are such that $V_{0,max}$–V_0 = 0.3 V and 0.1 V. In Figure 16A–I, the current density variations are shown at the time instants corresponding to the electrodeposition fronts depicted in Figure 13A, C and E, Figure 14A, C and E and Figure 15D, E and F, respectively. The initial value of the current density, i_0, in each case is also indicated in the plots. Note that in all the cases, the current density initially decreases from the respective i_0 value and subsequently increases with progress of the electrodeposition, following the trend with time presented in Figure 12. It is seen from Figure 16A–C and Figure 16D–F that during the electrodeposition process, the current density is initially laterally uniform and progressively becomes nonuniform at later times, with a minimum value at the centerline. Furthermore, the nonuniformity in the current density is seen to occur at earlier times and with a greater magnitude, as the applied voltage is increased [Figure 16A–C and Figure 16D–F], and that this effect is pronounced for the smaller trench height, Figure 16D–F compared to Figure 16A–C. At their respective maximum applied voltages, the lateral current density variation is seen to be about 40% with respect to the centerline value for H = 1000 μm at t = 12.56 h [Figure 16C] and about 136% for H = 100 μm at t = 0.34 h [Figure 16F]. Furthermore, for the same magnitude of $V_{0,max}$–V_0, the current density is significantly larger for the smaller trench height, as seen in Figure 16D–F relative to Figure 16A–C, respectively.

A comparison of Figure 16A–C with the deposition front evolution in Figure 13A, C and E, respectively, and similarly between Figure 16D–F and Figure 14A, C and E, respectively, reveals a strong correlation between the nonuniformity in the current density and the nonplanar

electrodeposition fronts; the deposition rates and deposition front growth are enhanced near the sidewalls that have the larger current density compared to the center of the microtrench. Figure 16G–I demonstrate the amplified nonuniformity of the lateral variation of the current density as the microtrench width is increased to 500 μm. In comparison to Figure 16D–F for W = 100 μm, it is seen that the current density values are smaller but more nonuniform with increasing

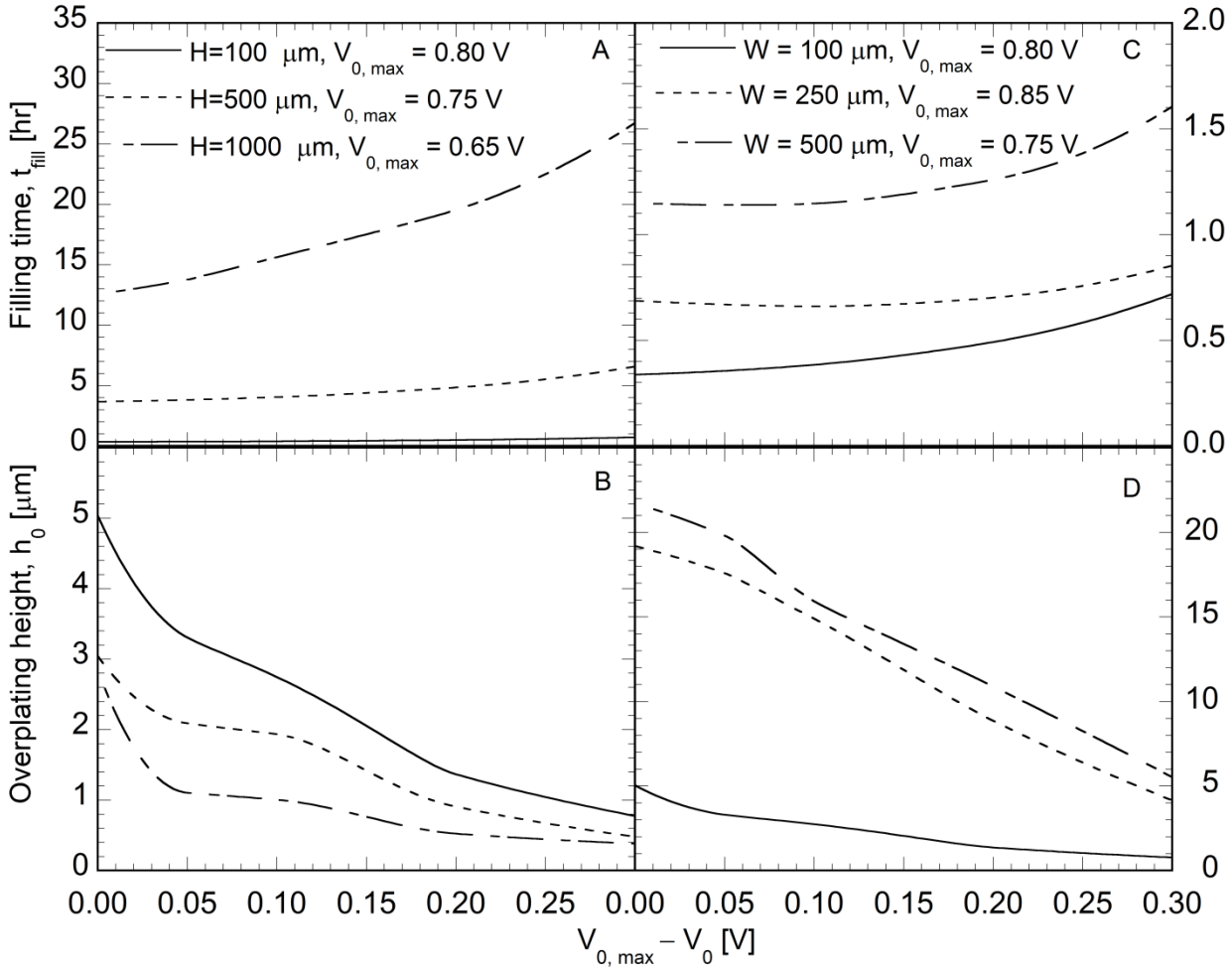

Figure 17: (a) Fill time and (b) overplating height as a function of $V_{0,max}$–V_0 for three microtrenches with W = 100 μm and H = 100, 500, and 1000 μm; (c) fill time and (d) overplating height as a function of $V_{0,max}$–V_0 for three microtrenches with H = 100 μm and W = 100, 250, and 500 μm

trench width, for the same magnitude of $V_{0,max}–V_0$. At the maximum voltage of 0.75 V, Figure 16I shows that the lateral variation of the current density is about 385% with respect to the value at the center of the microtrench for W = 500 μm at t = 1.15 h, which is approximately three times the corresponding nonuniformity in Figure 16F (W = 100 μm). Overall, Figure 16 reveals that the nonuniformity of current density progressively increases as the applied voltage increases, for a fixed microtrench aspect ratio (H/W), and as the microtrench aspect ratio decreases, for any fixed $V_{0,max}–V_0$.

As noted previously, the nonuniformity of the current density directly correlates to a nonplanar deposition and, in turn, overplating at the end of fill. The extent of overplating at the end of fill is an important consideration from the manufacturing viewpoint, in that the excess plating that is needed to completely fill the microtrench is often removed in a secondary processing step of lapping or other means of removal so as to get a flat finished product. It is, therefore, desirable to minimize or ideally eliminate the overplating at the end of fill. Toward analyzing the effect of the microgeometry and plating voltage on the overplating, the overplating amount was quantified in this study as the ratio of the excess volume of the plating at the fill time to the microtrench cross sectional area, to obtain an equivalent overplating height, h_0. Figure 17 shows the effect of the external voltage on the trench filling time [Figure 17A] and overplating height [Figure 17B] for Cases 1, 2 and 3 in Table 1, having the same microtrench width (W = 100 μm) but varying microtrench height. To facilitate comparison among these three cases, the plots are presented based on the difference between the magnitudes of the respective maximum voltage and the applied voltage, $V_{0,max}–V_0$. It is seen in Figure 17A and B that for a given trench height, H, the fill time t_{fill} decreases [Figure 17A] while the overplating height h_o increases [Figure 17B] with increasing external voltage, V_0. Figure 17A further shows that the fill time increases considerably

with increasing microtrench height, and that the increase is greater than the increased microtrench volume to be filled; for example, considering H = 100 μm and 1000 μm, at the smallest applied voltage in the respective cases, the ratio of the microtrench volumes is 10, whereas the ratio of their fill times is seen to be about 25, owing to the smaller deposition rate for the taller (high aspect ratio) microtrench. The overplating height, h_o, on the other hand is seen to decrease with increasing microtrench height, owing to the greater uniformity of current density across the microtrench width for the taller trenches, as discussed in Figure 16.

Figure 17C and D demonstrate the effect of the applied voltage, expressed as $V_{0,max}$–V_0, on the fill time [Figure 17C] and overplating height [Figure 17D], for Cases 3–5 in Table 1 which have the same microtrench height (H = 100 μm) but different microtrench width, W. The qualitative trends with respect to the applied voltage in Figure 17C and D mimic those in Figure 17A and B, respectively. Figure 17C shows that the fill time increases with increasing width as expected, but the increase is less than proportionate to the increase in the microtrench volume, owing to the fact that trenches with smaller opening size have higher current density and deposition rate. For example, although the volume of the microtrench in Case 5 is 5 times larger than that in Case 3, the ratio of the fill time for Case 5 to that of Case 3 is less than 5 at all applied potentials. Similarly, the fill time ratio is less than the volumetric ratio of 2.5 for Case 4 relative to Case 3. Figure 17D shows that the overplating height decreases with a decrease in the applied voltage, V_0, and that a smaller microtrench width results in less overplating. Increased overplating in wider microtrenches may be partly attributed to the increasing surface area for deposition, but is not the sole reason. In Case 4, W = 250 μm, the surface area is 2.5 times more than in Case 3, W = 100 μm; yet, Figure 17D shows that the ratio of their overplating heights is more than 2.5 for all the voltages. In Case 5, W = 500 μm, since the maximum voltage ($V_{0,max}$ = 0.75 V) is less than that

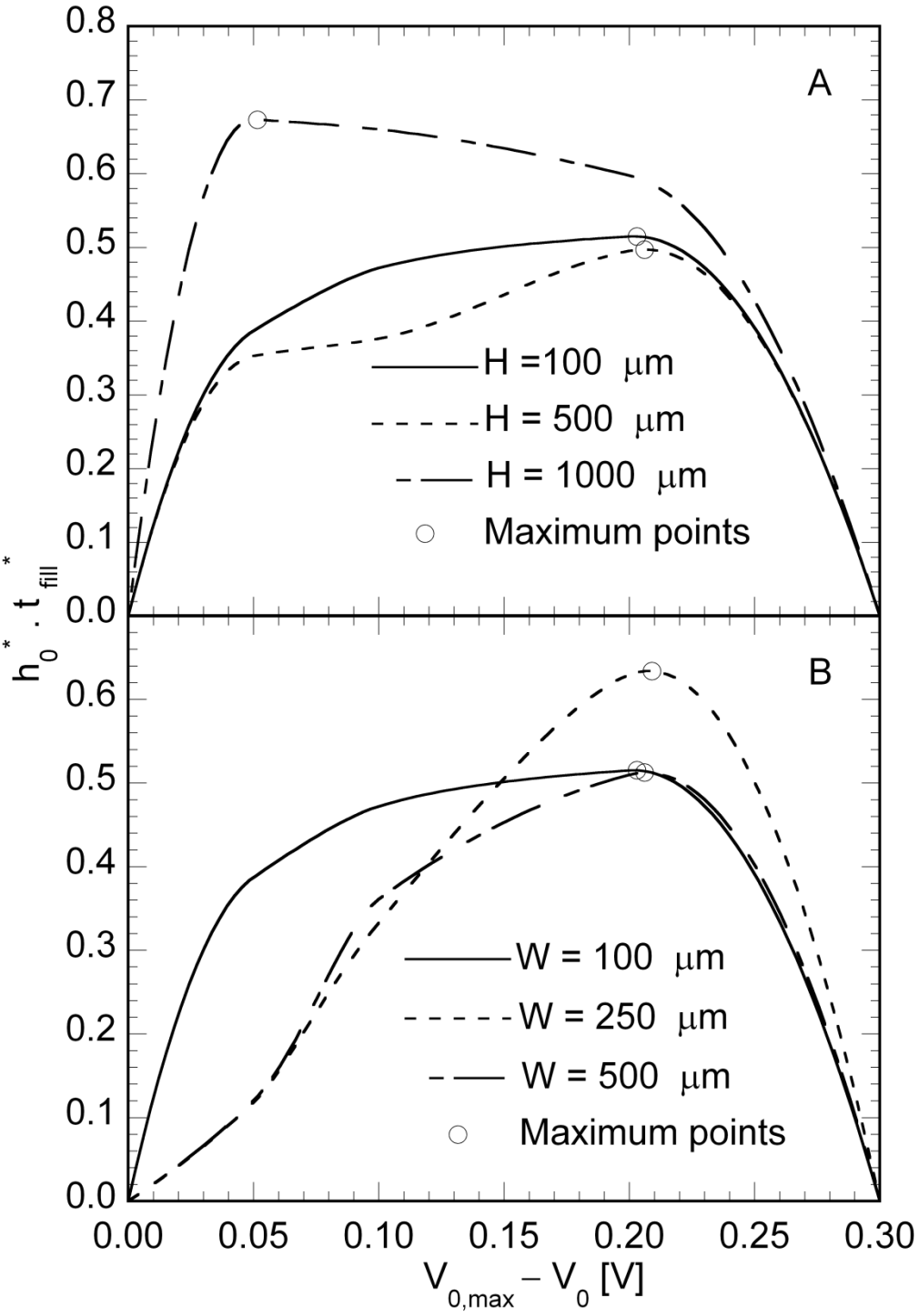

Figure 18: Variation of $h_0^* \cdot t_{fill}^*$ as a function of $V_{0,max}$–V_0 for microtrenches of (a) W = 100 μm and H = 100, 500, 1000 μm and (b) H = 100 μm and W = 100, 250, 500 μm. The optimum applied potential for each geometry is identified by the maximum points.

in Cases 3 (0.80 V) and 4 (0.85 V), the overplating height increase for W = 500 μm in Figure 17D is less than proportionate to the surface area ratio relative to W = 100 μm and 250 μm.

Based on the results in Figure 17, a higher applied voltage leads to a reduction in the fill time, whereas smaller applied voltages are preferred from the viewpoint of minimizing the amount of overplating. It is desirable to determine the optimum voltage, for a given microtrench geometry, that minimizes the fill time and the overplating simultaneously. To this end, a dimensionless fill time and overplating height, t^*_{fill} and h^*_0 respectively, were defined as follows: $t^*_{fill}(V_0) = \frac{t_{fill}(V_{0,min}) - t_{fill}(V_0)}{t_{fill}(V_{0,min}) - t_{fill}(V_{0,max})}$; $h^*_0(V_0) = \frac{h_0(V_{0,max}) - h_0(V_0)}{h_0(V_{0,max}) - h_0(V_{0,min})}$ where $V_{0,min}$ is the minimum applied voltage, which equals $V_{0,max}$ –0.30 V in all the presented cases. The applied voltage magnitude, V_0, which maximizes the product $t^*_{fill} \cdot \square^*_0$ is sought as the optimum voltage that simultaneously minimizes the fill time and the overplating height. Figure 18 shows the variation of the product function, $t^*_{fill} \cdot \square^*_0$, with the applied potential, expressed as $V_{0,max}–V_0$, for the three different microtrench height H [Figure 18A] and microtrench width, W [Figure 18B]. As expected, the product function is zero at the extremes of the applied voltage, and peaks for a certain applied voltage in between. The maximum point on each plot (identified by the open circles) yields the optimum applied potential, $V_{0,opt}$, for each geometry. It is seen from Figure 18A and B that except for the trench height of 1000 μm [Figure 18A], all the other optimum voltages are approximately 0.2 V less than the maximum voltage for the respective geometry such that $V_{0,max}–V_{0,\ opt}$ is approximately equal to 0.2 V in the figures. As Figure 17B shows, for the microtrench height, H = 1000 μm (Case 1 in Table 1), the overplating amount remains relatively less influenced by the applied voltage for $V_{0,max}–V_0$ exceeding about 0.05 V and has a sharp increase for $V_{0,max}–V_0$ below 0.05 V, whereas the applied voltage has a noticeable effect on the fill time over the entire range [Figure 17A]. Consequently, the optimum applied voltage for H = 1000 μm is a high value, based on consideration of

minimizing the fill time, and is seen in Figure 18A to be such that $V_{0,max}$–V_0 = 0.05 V at which point the overplating height sharply increases with further increase in V_0 in Figure 17B.

Table 2: Optimum applied voltage and the corresponding optimum fill time and overplating height for the cases studied

Case	H [μm]	W [μm]	$V_{0,opt}$ [V]	t_{fill} [h]	h_0 [μm]
1	1000	100	0.60	13.81	1.10
2	500	100	0.54	4.90	0.88
3	100	100	0.60	0.49	1.35
4	100	250	0.64	0.71	8.39
5	100	500	0.54	1.27	10.57

Table 2 summarizes the optimum applied voltage and the corresponding optimum fill time and overplating height for the five different microgeometries studied. As expected, the optimum fill time increases with increasing microtrench height (Cases 1–3 in Table 2) but since the optimum potential in Case 1 is nearer to its maximum voltage in comparison with Case 2, the overplating height increases slightly from H equal to 500 μm to 1000 μm. In the cases involving varying microtrench height for a fixed width, the overplating height is limited to within about 1.4 μm, and the optimum fill time is within about 14 hr. Cases 3–5 demonstrate that for a fixed microtrench height, both the optimum fill time and the optimum overplating height increase with increasing microtrench width; for the widest microtrench (Case 5 in Table 2), the optimal overplating height is limited to about 10.6 μm, with a corresponding optimal fill time of 1.27 h.

Figure 18 and Table 2 demonstrated optimal electrodeposition processing conditions (in terms of the applied voltage) for simultaneously minimizing the fill time and the overplating height. An alternative design requirement may be that of limiting the overplating height to within an allowable value. From Figure 17B and D, it is evident that a limit on a maximum allowable overplating height corresponds to a lower bound on $V_{0,max}–V_0$, denoted as $(V_{0,max}–V_0)_{min}$, or equivalently, a maximum value of the applied voltage. Considering an example of limiting the maximum allowable overplating to 1 μm, Figure 19 illustrates the variation of $(V_{0,max}–V_0)_{min}$ as a function of the microtrench height, *H*, based on the results in Figure 17(a) and (b). Also plotted in

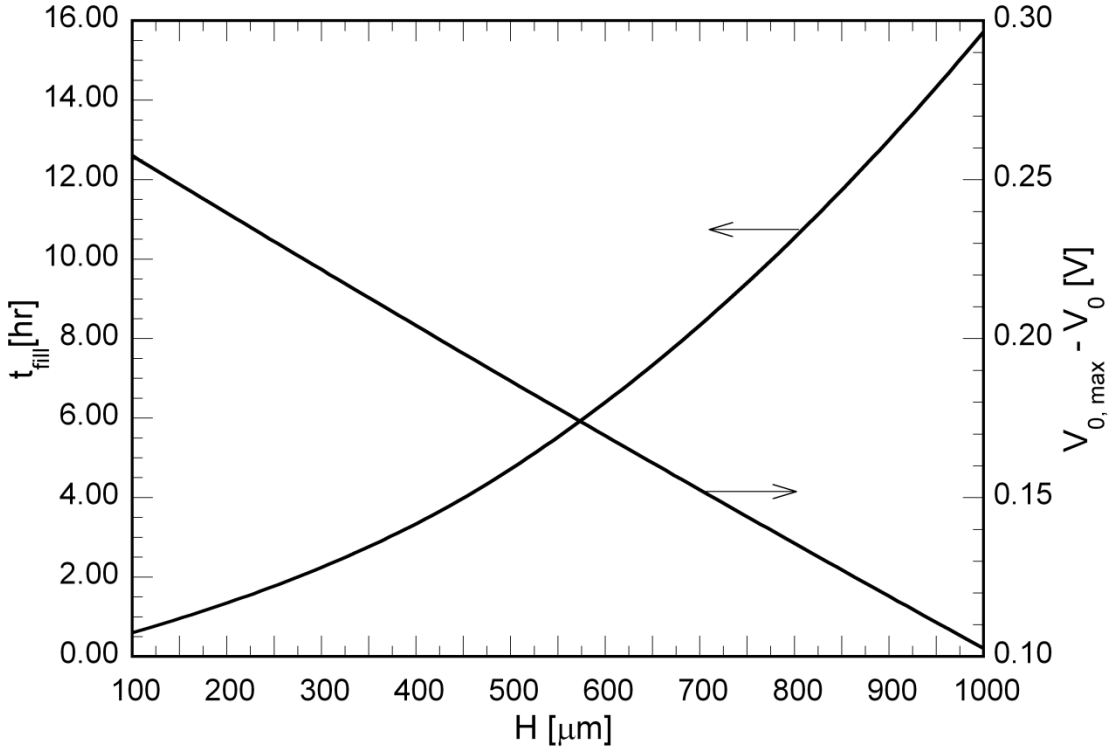

Figure 19: Variation of $(V_{0,max}–V_0)_{min}$ and the corresponding fill time with microtrench height for the design criterion of limiting the maximum overplating height to within 1 μm. The microtrench width is fixed at W = 100 μm.

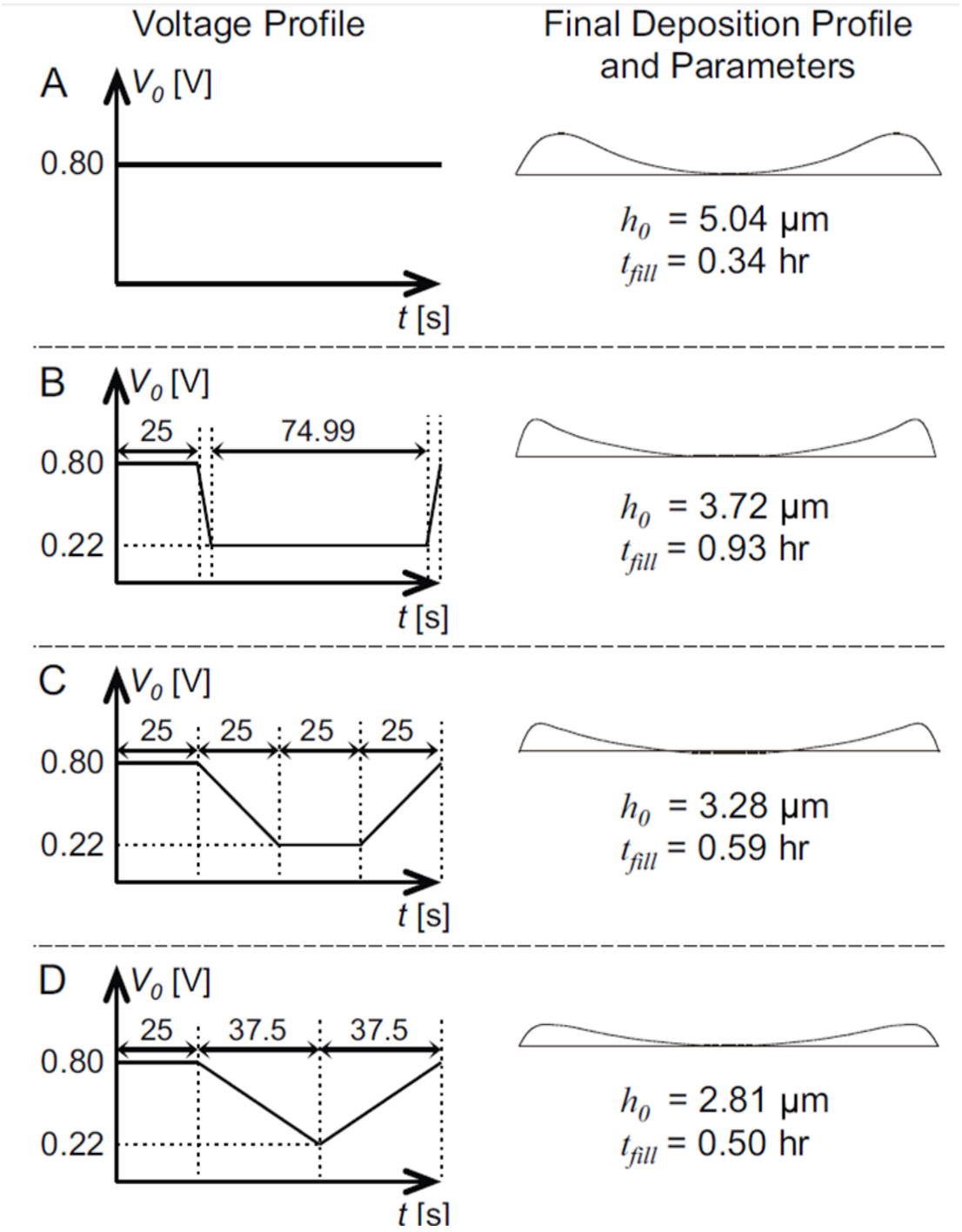

Figure 20: Profiles of the electrodeposition surface across the microtrench width at the fill time for $W = H = 100$ μm when (a) a constant voltage magnitude, and (b)–(d) time-varying voltage magnitude profiles are applied at the cathode.

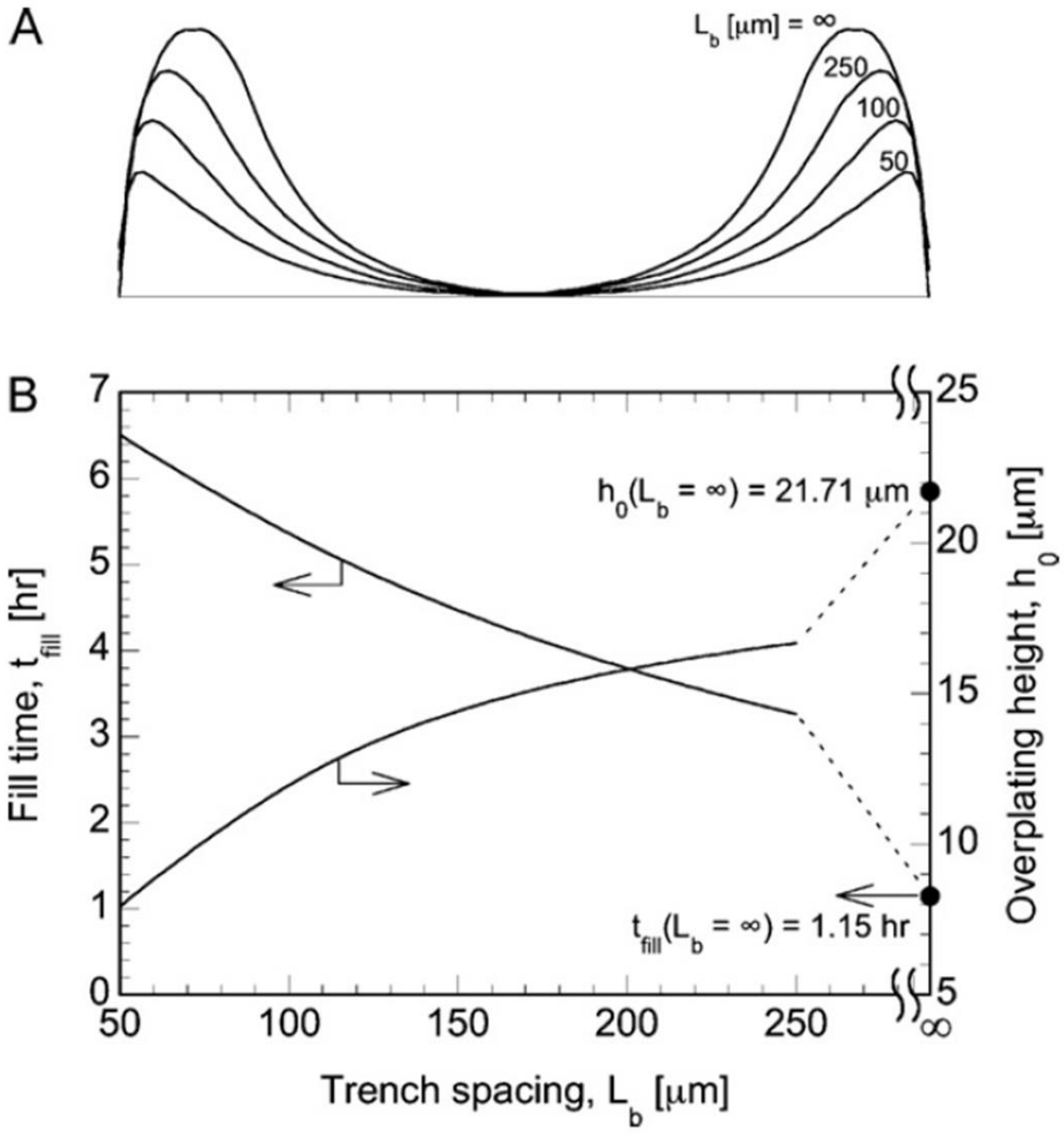

Figure 21: Effect of the trench spacing, L_b, on (a) the electrodeposition surface across the microtrench width at the fill time and (b) the fill time and the overplating height, for W = 500 μm and H = 100 μm.

Figure 19 is the variation of the fill time with the microtrench height, based on the applied voltage according to the $(V_{0,max}–V_0)_{min}$. It is seen that $(V_{0,max}–V_0)_{min}$ decreases—equivalently, the maximum

allowable applied voltage increases—with increasing trench height, and the corresponding fill time increases based on the design criterion of keeping the overplating height to within 1 μm.

The results presented so far elucidated the effects of the microtrench geometry for constant applied voltage values. The effect of a time-varying cathode voltage was studied by considering one cycle of a hold-and-ramp pattern, in which the voltage magnitude was varied between 0.80 V and 0.22 V, the thermodynamic open circuit potential for Nickel reduction, with a cycle duration of 100 s. Considering a square microtrench of $W = H = 100$ μm, and fixed bath dimensions of $L_b =$ 500 μm and $H_b = 1$ cm as before, Figure 20 presents the voltage variation with time and the final shape of the electrodeposition surface across the microtrench width at the fill time, for a constant voltage [Figure 20A] and three different time-varying voltage profiles [Figure 20B–D] with progressively decreasing hold times at the lower voltage. The fill time and the overplating height values in each case are also indicated below the final electrodeposition profiles in the figures. It is seen that the extent of overplating (h_0) as well as the fill time (t_{fill}) decrease as the hold time at the lower voltage decreases in the time-varying voltage profiles [Figure 20B–D]. The results indicate that, in general, use of a time-varying voltage [Figure 20B–D] reduces the amount of overfill, albeit at the expense of an increased fill time, compared to the case of a constant applied voltage [Figure 20A], owing to the reduced average applied potential in the time-varying cycle.

Figure 21 shows the effect of the microtrench spacing, L_b in figure 1, on the final electrodeposition surface across the microtrench width [Figure 21A] and the overplating height (h_0) and fill time (t_{fill}) [Figure 21B] for a microcavity of $W = 500$ μm and $H = 100$ μm. With increasing spacing, L_b, the electrodeposition surfaces are significantly nonuniform leading to pronounced overfills near the microtrench edges at the end of fill, as depicted in Figure 21(a). Figure 21(b) presents a quantitative variation of a monotonically decreasing fill time (solid line)

and a monotonically increasing overplating height (dashed line) with the trench spacing. The asymptotic values of the fill time (1.15 hr) and the overplating height (21.71 μm) for $L_b = \infty$ are also indicated in the plot. As the microtrench spacing increases, the current density increases since much of the surface in the bath is insulated, leading to both a reduction in the fill time as well as increased overplating, which is also in agreement with the findings of Mehdizadeh et al. [47].

The results presented so far elucidated the effects of the microtrench geometry and applied cathode voltage profiles on the overplating and fill time when both diffusion and electrode kinetics were considered as the affecting mechanisms. In addition to these two mechanisms overplating and fill time can be influenced by convection when an agitated bath is used instead of the stagnant condition. In this case if the height of the trench, *H*, is assumed as the characteristic length, time scales of diffusion, convection and reaction kinetics are defined as follows, respectively:

$$\tau_{diff} = \frac{H^2}{D},\ \tau_{conv} = \frac{H}{\omega},\ \tau_{kin} = \frac{H}{k_{Ni}\left[e^{\alpha_{a,Ni}\frac{F}{RT}\left(-V_0-U_{0,Ni}\right)} - e^{-\alpha_{c,Ni}\frac{F}{RT}\left(-V_0-U_{0,Ni}\right)}\right]} \qquad (40)$$

where ω is the average flow velocity. For trenches with height equal or less than width, cases 3 to 5 in table 1, when average flow velocity corresponds to 1000 Reynolds number, diffusive, convective and kinetic time scales are calculated as 10, 2.2e-3 and 1.09 respectively. Based on these time scales convection is much faster than diffusion and reaction kinetics. This corresponds to a more uniform concentration profile in the bath when deposition process is mainly controlled by the reaction kinetics. The current profile in this case will approach the secondary current profile as mixing level is increased in the bath, since uniform concentration profile and a kinetic controlled deposition are the main assumptions for electrodeposition based on the secondary effect. Dashed line in Figure 15F shows the profile of the electrodeposition front based on the secondary effect for the trench with the smallest aspect ratio and when the highest voltage (V_0 = 0.75 V) is applied on the cathode at fill time corresponding to 0.06 hr. Secondary effect shows the

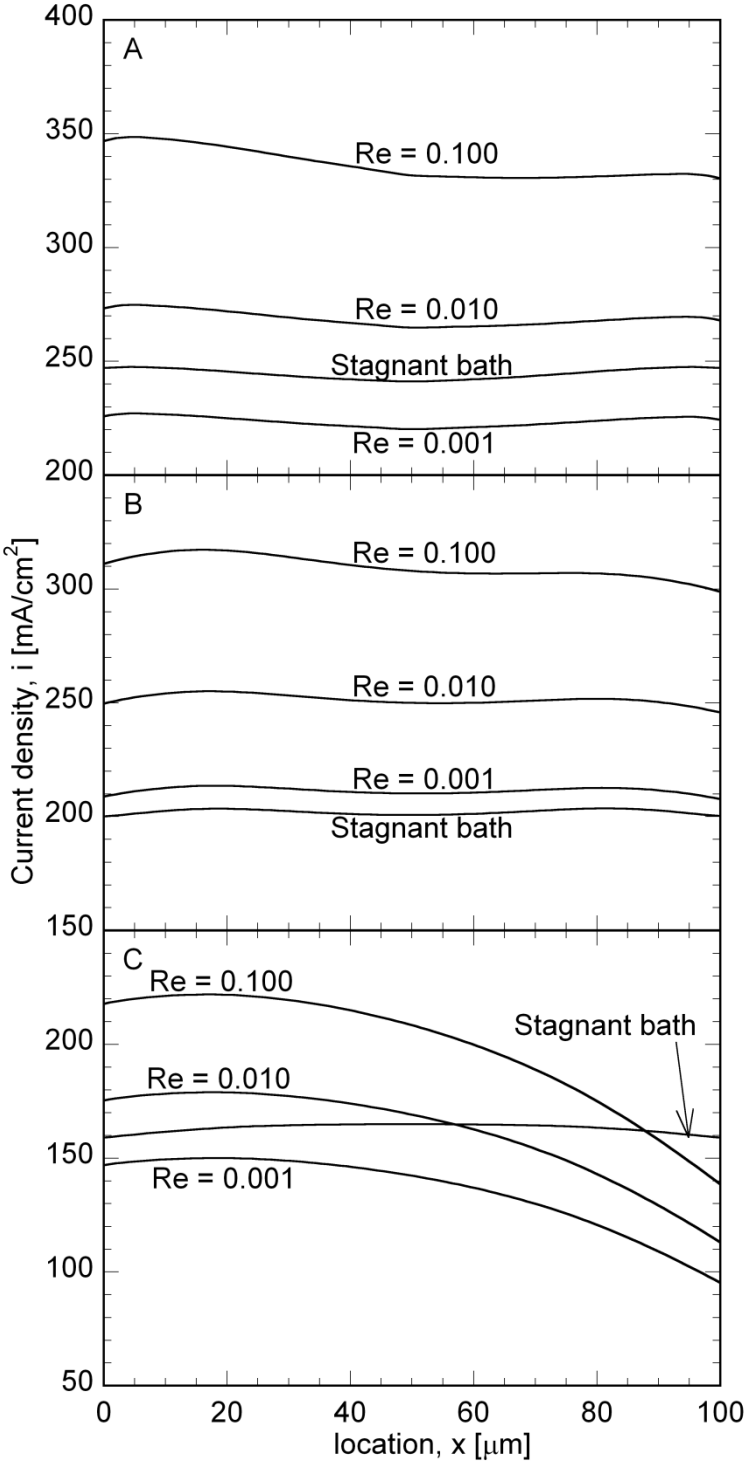

Figure 22: Current density profile when deposit is 50 μm bellow the topmost boundary of the microtrench with W = 100 μm and and height H = (a) 100 μm (b) 500 μm and (c) 1000 μm and magnitude of V_0 = (a) 0.80 V (b) 0.75 V and (c) 0.65 V.

extreme case of the effect of the convection on the process. In general convection tends to decrease overplating and fill time. Consequently, the optimum conditions presented by Figure 18 and Figure 19 are based on the conservative design scenarios.

At small Reynolds numbers convection is in the order of the diffusion and reaction kinetics and the process conditions are much far from the conditions applicable to the bath under secondary effect. Figure 22A–C show current density profile for a microtrench of width, W = 100 μm, and height, H = 100, 500 and 1000 μm, respectively, when deposit is 50 μm bellow the topmost boundary of the trench and applied voltage corresponds to the $V_{0,max}$ shown in Table 1 for each geometry. These figures are based on implementing convective flow from left to right by solving Navier-Stokes equation in the bath considering Reynolds numbers of 0.100, 0.010 and 0.001 in addition to the Nernst-Plank and moving mesh formulation mentioned in section 2. Detailed formulation can be found elsewhere [15, 56-58]. Based on these figures, current density and correspondingly deposition rate decrease in the direction of the flow from left to right. Current density non-uniformity due to the bath flow is more for higher Reynolds numbers or higher aspect ratios.

The results in this section highlighted the effects of the microtrench geometry, inter-trench spacing and the applied cathode voltage profiles on the overplating and fill time and presented two example conservative design scenarios. More studies on the effect of the convection on the reducing processing time and improving quality of the deposition process may be considered in a future study. Further, the modeling presented here may be expanded to include evolution of the grain morphology during electrodeposition in microcavities for a comprehensive relationship between the process and geometry parameters and the resulting micropart quality. These issues will be considered in a future study.

Chapter 4: Modeling of Electrodeposition Through a Microscreen-based Micromold

Electrodeposition in sacrificial micromolds with a microscreen base and thermoplastic sidewalls is one of the main techniques for fabricating metallic microstructures. These micromolds are fabricated through an injection molding process by forcing a metal microscreen into a softened thermoplastic. During this process, the holes of the microscreen are filled by the thermoplastic and form insulating parts on the micromold base. In the electrodeposirtion process, deposit originates from the conductive parts of the micromold base and grows along the insulating walls conforming to the micromold geometry. In this work, computational models for the governing transport and electrochemical phenomena are used to simulate the shape of the electrodeposition front and the spatial current density profile with time. The effects of the applied voltage and microscreen geometry (the size and number of the insulating parts on the micromold base) are systematically studied for their influence on the nonuniformity of the current density and deposit surface profile. Conditions that lead to desirable process and part quality are derived from the studies.

4.1 Introduction

Electrodeposition is a competitive process in precision micromanufacturing due to its ability to produce microstructures close to dimensional tolerances with superior material characteristics. In fact, when fabrication requires high tolerance, complexity, and miniature geometry, electrodeposition is usually the only economically viable manufacturing process[1]. Metallic microstructures are mainly fabricated by electrodeposition of a metal or alloy through sacrificial polymeric micromolds. This microfabrication technique is called LIGA, an acronym for the

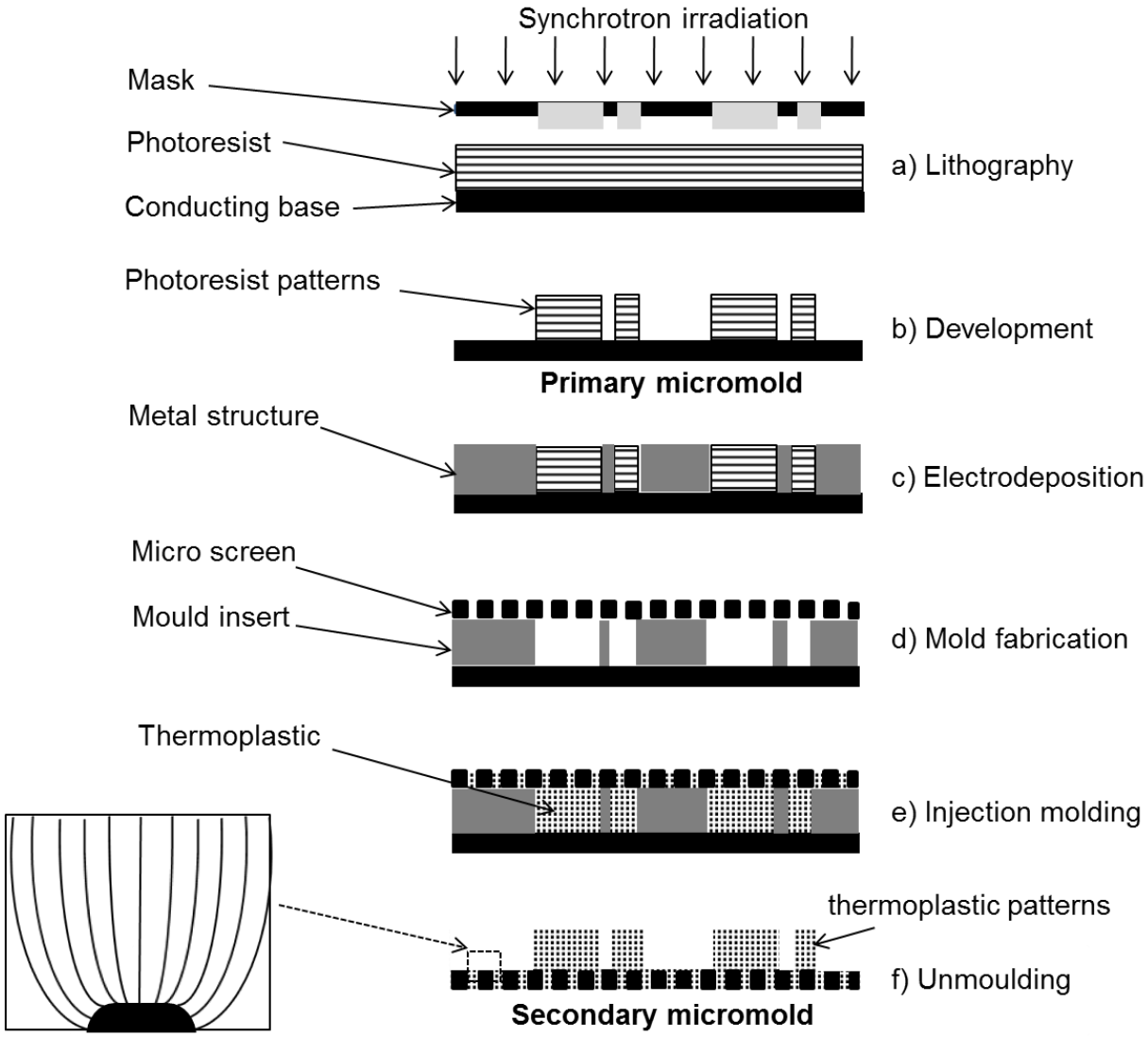

Figure 23: Steps of the LIGA process. Inset: Bending of the current lines close to the insulating holes on the base of the trench.

German words for lithography, electrodeposition and molding. The steps of the LIGA process have been shown in Figure 23. Synchrotron radiation lithography is used to make patterns with micron dimensions on a layer of photoresist spread over a conducting substrate (Figure 23a and Figure 23b). Each pattern is considered a primary micromold with a conducting base and insulating walls, such that the metal deposit originates from its conducting base and grows along

the insulating walls conforming to the micromold geometry (Figure 23c). Therefore, a metallic microstructure that is negative in feature with respect to the micromold (Figure 23d) is formed which can be either used directly or placed as a mold insert in an injection molding process to force a metal microscreen into a softened thermoplastic (Figure 23e). The injection molding process results in the formation of the secondary micromold composed of a microscreen base and thermoplastic walls (Figure 23f). The holes of the microscreen are filled by the thermoplastic during the injection molding process and form insulating parts on the base of the secondary micromold. In contrast, the base of the primary micromold is composed of an integrated conductive part. In addition, the cost and fabrication time of the secondary micromold are much less than the primary micromold [2-5].

In general, electrodeposition may be controlled by two main processes: a mass transfer process in the electrolyte and an electrochemical reaction on the electrode surface. Reaction-controlled deposition occurs in a well-mixed bath or when a sufficiently low overpotential is applied in a diffusive bath. When deposition is mainly controlled by the electrochemical reaction, a uniform concentration profile is developed in the electrolyte. As a result, the mass transfer effect is negligible and the current density distribution is defined by the effects of the electric field distribution on the rate of the electrochemical reaction [54, 55, 64]. In a diffusive bath, if the overpotential is higher than what is required for the reaction-controlled deposition, a concentration gradient is developed in the bath and the concentration of ions on the electrode surface reduces to a value less than the bulk concentration. At this condition, both mass transfer and electrochemical reaction are considered the controlling parameters. However, in the case of electrodeposition through microtrenches mass transfer usually plays a more important role due to the confinement effect. Even if convection is applied in the bath, the speed of the induced circulating flow falls

dramatically along the depth of the microtrench so that transport is controlled by diffusion along most of the microtrench depth[15]. When deposition is partially or completely controlled by diffusion, ion concentration along microtrench sidewalls is higher than the central part. This is because the central part of the microtrench receives ions only from the bath area above it while the microtrench edges have access to other parts of the bath as well[53]. Later on in this paper, this effect of the diffusion process on the concentration nonuniformity is referred to as the "edge effect". The nonuniform concentration results in the higher current density or deposition rate along the microtrench sidewalls. The nonuniformity of the current density is negligible at the onset of deposition through a microtrench but it gradually increases and results in a thicker deposit along the sidewalls of the microtrench compared to the central part[37]. Consequently, when the microtrench is completely filled, an overplating is obtained along the edges of the microtrench opening. This overplating should be removed in a subsequent precision grinding process in order to level the surface of the microstructure. The overplating amount determines the time required for the grinding process and depends on the applied voltage and micromold geometry.

The model for the electrodeposition though a primary micromold was previously presented in the several works[10, 12, 13], though in most of these works, the model was not used to study the effects of the process parameters on the extent of overplating. Haghdoost and Pitchumani[37] used the Nernst-Plank model to systematically study the effects of the process parameters on the deposit surface profile in electrodeposition thorough a primary micromold. Based on their study, higher potential magnitude results in less deposition time and more overplating amount. Moreover, the overplating amount is smaller for a microtrench with larger height to width ratio.

Unlike electrodeposition through a primary micromold, relatively few investigations are found in the literature on electrodeposition through a secondary micromold. The base of the secondary

micromold is composed of the insulating thermoplastic and conductive metal parts. Chen and Evans[16] showed that the deposit surface is essentially flat when the thermoplastic part of the base is elevated relative to the microscreen metal. In contrast, dimples are formed on the deposit surface when the microscreen metal is slightly elevated relative to the thermoplastic parts of the microtrench base. In this case, overplating amount depends on the size and number of the insulating holes on the microtrench base in addition to the "edge effect". In the work presented by Chen and Evans, the effect of the microscreen geometry on the shape profile of the deposition front has not been presented.

The surface area of a patterned electrode may be defined in two different ways. The superficial area, A_{sup}, is the projected area of the patterned surface which is equal to the area of the corresponding flat surface. Consequently, the existence of the insulating holes is ignored in the definition of the superficial area for a secondary micromold. On the contrary, the active area, A_{act}, is defined as the conductive area available for metal deposition. Note that in this study, none of the aforementioned area definitions account for the existence of the microscopic surface roughness. Having defined the superficial and active areas, it is now possible to define the active-area density as

$$a = A_{act}/A_{sup} \tag{41}$$

In addition, superficial current density, i_{sup}, and actual current density, i_{act}, are defined as the ratio of the current to the superficial and active areas, respectively. The definitions of i_{sup}, i_{act}, and a are consistent with the following relation

$$i_{act} = i_{sup}/a \tag{42}$$

The physical interpretations of i_{sup} and i_{act} are illustrated in the inset of Figure 23 which shows current lines in a secondary micromold extending toward the microscreen base. Far from the

microtrench base, current lines are evenly spaced, reflecting that the discrete insulating holes on the depositing surface do not exert any influence on the current distribution. Consequently, far from the microtrench base, current density corresponds to i_{sup}. In contrast, current lines are bent toward the conductive parts of the microscreen close to the base of the secondary micromold. The actual current density obtained at this location is larger than the superficial current density. Equation (42) relates the solution of the electrochemical model for a primary micromold to the one for a secondary micromold with the same size through a geometric parameter, a, which depends on the size and number of the insulating holes. The same method was used previously by Mehdizadeh et al.[47] to model the electrodeposition process on a surface patterned by closely-spaced microtrenches.

Later on in this paper, the effect of the insulating holes on the current density distribution and deposit surface profile is referred to as the “active-area density effect”. The "active-area density effect" and "edge effect" are more pronounced close to the beginning and end of the deposition process, respectively. The present model considers the more prominent effect at each process time and neglects the other one. This model can be used to capture the evolution of the deposition front and find the effects of the microscreen geometry (i.e. size and number of the insulating holes) on the fill time and overplating amount. This article is organized as follows: The mathematical modeling and the numerical simulation procedure are described in the next section, followed by a presentation and discussion of the results of the study.

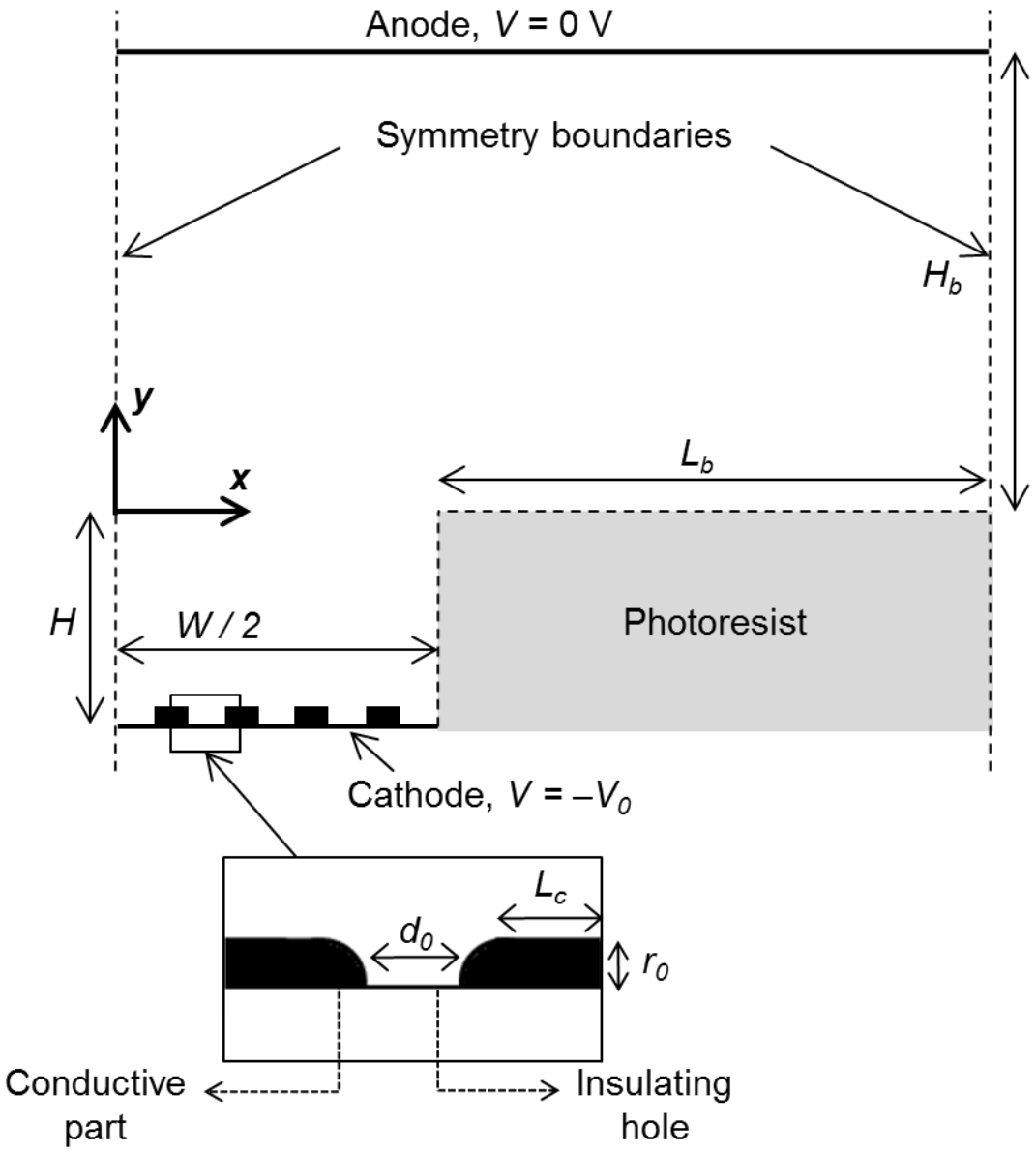

Figure 24: Schematic of the modeling domain considered in the study. Inset: Cathode geometry

4.2 Mathematical Model

Figure 24 shows a schematic of a two-dimensional rectangular microtrench with width *W*, and height *H* in an electrodeposition bath with height H_b, and width outside of the microtrench L_b. The origin of the coordinate system is positioned coincident with the center of the top surface of the

microtrench. The anode with reference voltage $V = 0$ V, covers the entire top surface of the bath; while cathode is considered to be at the bottom surface of the microtrench, where a constant voltage of $V = -V_0$ is applied during the electrodeposition process. Other surfaces, shown by the dashed lines in the figure, represent either a wall or a line of symmetry. As depicted in the inset of Figure 24, cathode is alternately composed of the insulating and conductive parts with size of d_0 and L_c, respectively, which are connected by ninety degree fillets with radius r_0. Size of the connecting fillets does not affect the solution as long as it is small compared to the flat parts of the cathode. By virtue of symmetry of the geometry domain and the applied boundary conditions, only one half of the microtrench is considered in the modeling domain.

The electrolyte system is a nickel sulfate bath consisting of a solution of Ni^{2+} and SO_4^{2-} ions in water. The anode is assumed to be unpolarized; therefore its shape remains constant during the process. On the contrary, nickel deposition occurs on the cathode surface through the electrochemical reaction of $Ni^{2+} + 2e^- \leftrightarrow Ni$. In addition to this surface reaction, the homogeneous reaction of $Ni^{2+} + OH^- \leftrightarrow Ni(OH)^+$ occurs in the electrolyte at high pH values. However, in this investigation, the bath pH is assumed to be maintained below 4, for which the production of $Ni(OH)^+$ and the concentration change of Ni^{2+} due to the homogeneous reaction is negligible[16]. Furthermore, in this modeling, constant diffusion coefficient and electrode kinetic parameters are considered.

Superficial current density, i_{sup}, is obtained using the model described in the next section by considering a conductive flat surface instead of the microscreen at the bottom surface of the microtrench. The growth velocity, v, which is normal to the deposit surface, is governed by the following equation:

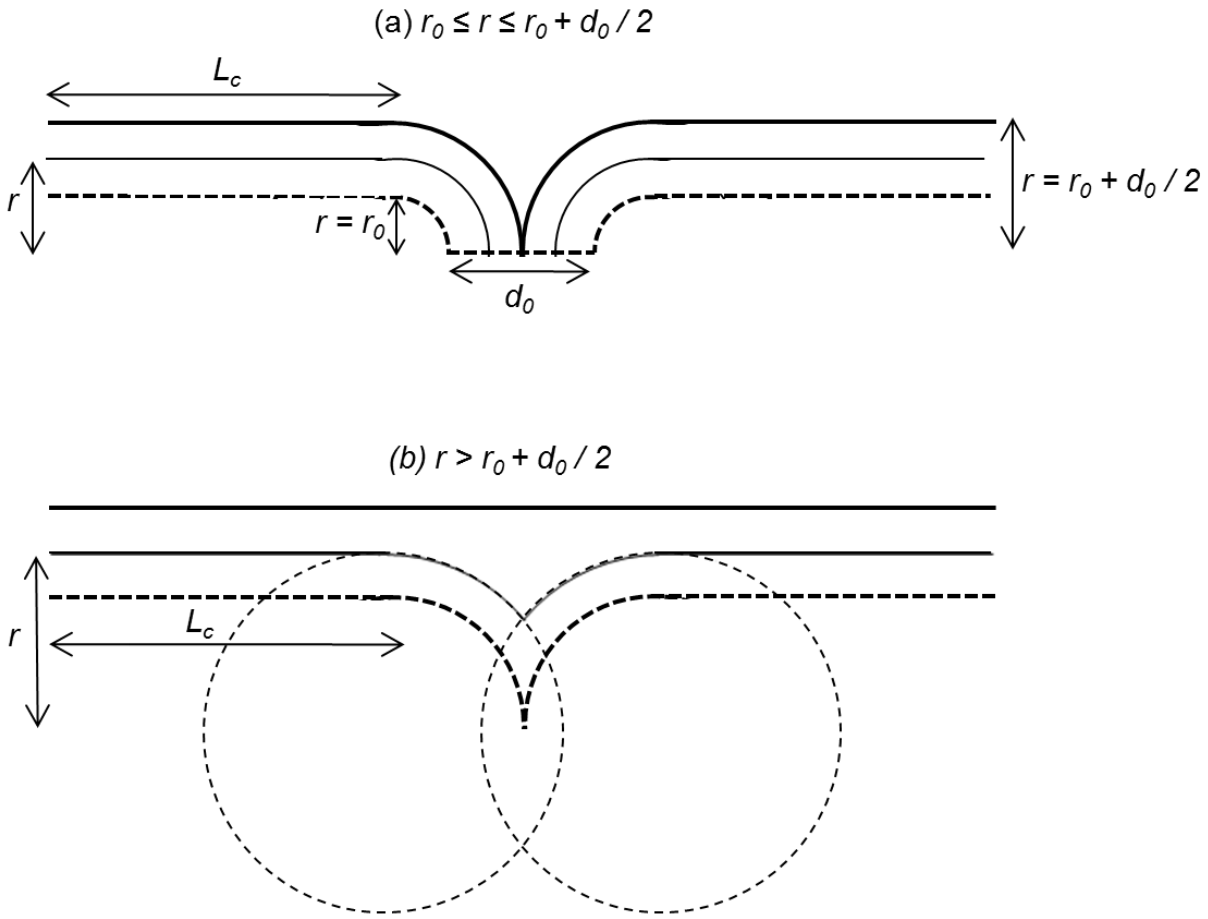

Figure 25: Schematic of the deposit evolution (a) $\boldsymbol{r_0 \leq r \leq r_0 + \frac{d_0}{2}}$, Size of the hole varies from $\boldsymbol{d_0}$ to zero. (b) $\boldsymbol{r > r_0 + \frac{d_0}{2}}$, Size of the cleavage on the deposit surface is getting smaller during time. Dashed lines corresponds to the schematic at the later time.

$$v = \frac{M_{Ni} i_{sup}}{a F z_{Ni} \rho_{Ni}} \tag{43}$$

Growth velocity may also be obtained from the time derivative of the deposit height, *r*. As the inset in Figure 24 shows, deposit growth is initiated from the height of r_0, because microscreen metal is elevated by r_0 relative to the thermoplastic parts of the micromold base. Consequently, following equation may be used to obtain deposit height at different process times:

$$\frac{dr}{dt} = v, \qquad @\ t = 0: r = r_0 \tag{44}$$

At small deposition times, "edge effect" is negligible and shape of the deposition front is mainly determined by the "active-area density effect". Figure 25a-b show the schematics of the deposit surface profile when only the "active-area density effect" is considered. The thick dashed line in Figure 25a shows the surface profile of the micromold base which has also been shown in the inset of Figure 24. As the deposit grows, the size of the insulating hole at the micromold base decreases from d_0 to zero. The thick solid line in Figure 25a shows the deposit surface profile right after the insulating hole was filled in. At this time, the deposit reaches to the height of $r_0 + d_0/2$. When deposit height is in between r_0 *and* $r_0 + d_0/2$, the general schematic of the deposit surface is represented by the thin solid line in Figure 25a. Moreover, at this region, active-area density, *a*, increases with time and can be obtained from the following equation:

$$a = \frac{(N+1)L_c + N\pi r}{W} \quad , \quad r_0 \le r \le r_0 + \frac{d_0}{2} \tag{45}$$

where *N* is the number of insulating holes and L_c, *r*, *W* and d_0 are geometric parameters shown in Figure 24 and Figure 25a.

Figure 25b shows the schematic of the deposit surface profile for the deposit heights more than $r_0 + d_0/2$. The thick dashed line in this figure corresponds to the last line in Figure 25a which shows the surface profile right after the insulating hole was completely covered by the deposit. At this time, the active-area density reaches its maximum value which is greater than one. The general schematic of the deposit surface profile at deposit height *r* has been shown by the thin solid line in Figure 25b. As this line shows, the effect of the initial insulating hole remains as a dimple on the deposit surface. The size of this dimple is smaller at more deposit heights. Consequently, at the stage of deposition shown in Figure 25b, active-area density decreases with time. Finally, the

dimple vanishes and a flat surface profile as shown by the thick solid line in Figure 25b is obtained. Consequently, at the stage of deposition shown in Figure 25b, active-area density decreases with time and finally approaches one. At this stage, the following equation for the active-area density is held:

$$a = \frac{(N+1)L_c + N\pi r - 2Nr \times \text{acos}(\frac{r_0 + \frac{d_0}{2}}{r})}{W} \quad , \quad r > r_0 + \frac{d_0}{2} \tag{46}$$

At the deposition time, denoted by t_{ex}, "active-area density effect" and "edge effect" are equal. In this work, “edge effect” and “active-area effect” are denoted by E_e and E_{aad}, respectively, and may be defined using the following equations:

$$E_{aad} = a - 1 \quad , \quad E_e = \frac{A_{act}^{*}}{A_{sup}} - 1 \tag{47}$$

where A_{act}^{*} is the active area of a primary micromold with the same superficial area, A_{sup}, as the secondary micromold. A_{act}^{*} is obtained from the model presented in the next section for electrodeposition through a primary micromold, while A_{sup} is the area of a rectangle with the width of W. At the start of the deposition, A_{act}^{*} is equal to the superficial area and E_e is zero. As deposit develops, a curved deposition front is evolved from the flat micromold base due to the “edge effect” and A_{act}^{*} gradually enhances. Consequently, E_e monotonically increases during the deposition process. In contrast, E_{aad} starts from a non-zero value due to the existence of the insulating parts on the base of the secondary micromold. It increases gradually and reaches its maximum value when the insulating parts are completely covered by the deposit. After this time, E_{aad} decreases gradually by approaching zero.

The current model assumes negligible “edge effect” compared to the “active-area density effect” for the deposition times less than t_{ex}. At this stage of the deposition, uniform growth rate, shown by Eq. (43), is considered on the deposit surface. In this equation, superficial current

density, i_{sup}, is found from the model presented in the next chapter for the electrodeposition through a primary micromold with the width of *W*. Moreover, *a* is found from either Eq. (45) or Eq. (46). At each time step, the growth rate obtained from Eq. (43) is applied in Eq. (44) to obtain deposit height at the next time step. Furthermore, the surface profile of the deposit can be constructed considering the schematic shown in Figure 25. After t_{ex}, the shape of the deposition front is governed by the "edge effect", and "active-area density effect" is negligible. At this stage of the deposition, the surface profile of the deposit is obtained from the model presented in the next section for the electrodeposition through a primary micromold.

4.2.1 Modeling of the Electrodeposition through a Primary Micromold

In Figure 24, if the microscreen at the bottom surface of the micromold is replaced by an integrated conductive surface with width of *W*, model schematic for the electrodeposition through a primary micromold is obtained. The dimensionless transport equations of the dissolved ions, $Ni^{2+}$and SO_4^{2-}, are governed by:

$$\frac{\partial {c_i}^*}{\partial t^*} + \nabla^*.(-\nabla^* {c_i}^* - {c_i}^* \nabla^* {\phi_i}^*) = 0 \quad , \qquad i = 1, 2 \tag{48}$$

where ${c_1}^*$and ${c_2}^*$are dimensionless concentrations of Ni^{2+} and SO_4^{2-}, respectively. In addition, t^* and ϕ^* denote dimensionless time and potential, respectively. The term in the parentheses is the dimensionless mass flux of the ion *i*, composed of two components standing for the diffusive mass flux and electromigration, respectively. Characteristic concentration, length and time are defined as the bulk concentration of nickel sulfate (c_0 = 0.00126 mol/cm^3), height of the trench, *H*, and square height over diffusivity, H^2/D_i, respectively. Moreover, dimensionless potential, ${\phi_i}^*$, in the electromigration term is defined as follows:

$$\phi_i{}^* = \frac{\emptyset + V_0 + U_0}{RT/(z_i F)} \quad , \qquad i = 1,2 \tag{49}$$

where V_0 is the magnitude of the external voltage applied to the cathodic deposition surface. In addition, U_0, R, F, T, and z_i denote the open-circuit potential, gas constant, Faraday constant, temperature, and charge number of the ions, respectively.

Any charge imbalance across an electrochemical system is quickly neutralized by the ions solved in the electrolyte. This electroneutrality condition is governed by the following equation:

$$\sum_{i=1}^{2} z_i c_i{}^* = 0 \tag{50}$$

Equation (51) is obtained by multiplying Eq. (48) by $z_i F$ and then summing over two species:

$$F \sum_{i=1}^{2} z_i \frac{\partial c_i{}^*}{\partial t^*} + \nabla^* . \left(F \sum_{i=1}^{2} (-z_i \nabla^* c_i{}^* - z_i c_i{}^* \nabla^* \phi_i{}^*) \right) = 0 \tag{51}$$

The time derivative of Eq. (50) shows that the first term in Eq.(51) is zero. As a result, following equation is obtained:

$$\nabla^* . \left(\sum_{i=1}^{2} (-\nabla^* c_i{}^* - c_i{}^* \nabla^* \phi_i{}^*) \right) = 0 \tag{52}$$

Equations (48) and (52) represent dimensionless formulations of the Nernst-Planck model for the electrodeposition process. This model may be solved to obtain three unknowns: dimensionless potential in the bath, $\phi_i{}^*$, dimensionless concentrations of Ni^{2+}, $c_1{}^*$, and $SO_4{}^{2-}$, $c_2{}^*$.

The system of equations is solved subject to the following boundary conditions: (a) along the anode surface, molar concentration of the ions is fixed at the bulk value which results in the dimensionless concentration of one ($c_i{}^* = 1$). Moreover, dimensionless potential along the anode surface is obtained from Eq. (49) considering zero electric potential ($\phi_i{}^* = \frac{V_0 + U_{0,Ni}}{RT/(z_i F)}$); (b) insulated conditions are applied along the symmetry boundaries, side walls of the bath and microtrench and

on the bottom surface of the bath; and (c) along the moving cathodic deposition surface at the base of the microtrench, flux of the sulfate ion is zero and current density is obtained from the flux of the nickel ion using the Butler-Volmer equation. This current density is the actual current density if deposition occurs through a primary micromold. In this work, the model formulation for the electrodeposition through a secondary micromold is related to the one through a primary micromold using active-area density parameter. For the electrodeposition through a secondary micromold, the dimensionless current density along the cathodic deposition surface is defined as follows:

$$a)\quad {i_{sup}}^{*} = a\left(\frac{k_1 H}{D_1}\right)c_1^{*}\left[e^{\frac{-\alpha_{a,1}{\phi_1}^{*}}{z_1}} - e^{\frac{\alpha_{c,1}{\phi_1}^{*}}{z_1}}\right], \qquad t \le t_{ex} \tag{53}$$

$$b)\quad {i_{act}}^{*} = \left(\frac{k_1 H}{D_1}\right)c_1^{*}\left[e^{\frac{-\alpha_{a,1}{\phi_1}^{*}}{z_1}} - e^{\frac{\alpha_{c,1}{\phi_1}^{*}}{z_1}}\right], \qquad t > t_{ex}$$

where k_1, $\alpha_{a,1}$and $\alpha_{c,1}$, are kinetic parameters denoting the rate constant, anodic and cathodic transfer coefficients respectively, which are all assumed constant in this work. Moreover, the dimensionless current density is defined as: $i^{*} = \frac{i}{c_0 z_1 F D_1/H}$. Equation (53) indicates that for the deposition times less than t_{ex}, the superficial current density, used in Eq. (43), is obtained from the present model by multiplying the actual current density by the active-area density. In contrast, after t_{ex}, "active-area density effect" is negligible and actual current density is found from the model. Equation (53) indicates that at the deposition times less than t_{ex}, the present model may be used to obtain superficial current density is obtained by multiplying actual current density by the active-area density.

The moving computational domain during electrodeposition was modeled using the arbitrary Lagrangian-Eulerian (ALE) method [63]. In this method, if the mesh displacement becomes large and the mesh quality degrades at any instant during the computations, the domain is re-meshed and

all solution variables are mapped from the old mesh to the new one. The moving mesh formulation is subject to the following boundary conditions: (a) the mesh displacement along the left and right side walls of the microtrench and bath was fixed to be zero in the *x* direction; (b) the mesh displacement along the bottom surface of the bath was fixed to be zero in the *y* direction; (c) the mesh displacement was restricted in both *x* and *y* directions along the top boundary of the bath and (d) along the moving deposition surface, the normal velocity of the deposition front is obtained from equation (43).

4.2.2 Method of Solution

The model formulation described above is solved using a finite element technique, in the commercial software, COMSOL 3.5a. An initial concentration, c_0 = 0.00126 mol/cm^3, is considered for both Ni^{2+} and SO_4^{2-} ions. Bath height, H_b, is assumed at least ten times larger than the microtrench height; as a result the existence of the microtrench at the bottom surface of the bath has negligible effect on the concentration profile along the top surface of the bath which remains constant at c_0 during the deposition process. The open circuit potential, kinetic parameters and diffusivity are obtained from the literature for the nickel sulfate bath at the temperature of 40 °C [16] as follows U_0 = –0.22 V, k_1 = 0.0001 *cm/s*, $\alpha_{c,1} = \alpha_{a,1}$ =0.21, and $D_1 = D_2 = 10^{-5}$ cm^2/s. Equation (53) is utilized to obtain the initial value of the superficial current density which may be used in Eq. (43) to find the initial velocity of the deposition surface. The initial growth velocity is used in Eq. (44) and the model presented in section 2-1 to acquire the surface profile of the deposit and superficial current density at the next time step, respectively. This procedure is continued before time t_{ex} at which the values of E_{aad} and E_e shown in Eq. (47) are equal. Note that before t_{ex},

active-area density is found from either Eq (45) or Eq (46). On the contrary, after t_{ex}, active-area density is removed from the model formulation and deposit surface profile is obtained using the model presented in section 2-1 for the electrodeposition through a primary micromold.

In the next section, the model is first validated by comparisons with a previously published model. Systematic parametric studies are then conducted to investigate the influence of the applied voltage, the size of the insulating hole and number of holes on the variation of the current density with time as well as the extent of the overplating at the end of the process. A micromold with equal height and width, W^* = 1, is considered in the model. Furthermore, the dimensionless parameters of the bath, $L_b^* = \frac{L_b}{H}$ and $H_b^* = \frac{H_b}{H}$, and dimensionless fillet size, r_0^*, are kept constant at 50, 100, and 0.001, respectively, unless otherwise mentioned. The effect of the microscreen geometry is studied by varying the dimensionless size of the insulating hole, d_0^*, or number of holes, N, while keeping the potential magnitude, V_0, constant. Moreover, in order to investigate the effect of the potential magnitude, model was solved for different potential magnitudes while the micromold geometry was kept constant. Mesh refinement test was performed for each study to make the results independent of the mesh size.

4.3 Results and Discussion

The model presented in section 2-1 was validated with the computational results of Chen and Evans [16] for electrodeposition through two primary micromolds with the size of 1 mm × 1 mm (wide) and 1 mm × 0.2 mm (narrow). Figure 26 presents the current density at the centers and sidewalls of these microtrenches as a function of time when the external potential of –0.6 V is applied. In this figure, the lines denote the results of the present simulation, while the markers

correspond to the data reported by Chen and Evans. It is seen that the present simulation is in close agreement with the results of Chen and Evans. Furthermore, effect of the micromold geometry on the current density in electrodeposition through a primary micromold has been depicted in this figure. For the micromold with a larger height to width ratio, i.e. narrow microtrench in Figure 26, current density is higher and changes more with time compared to the wide microtrench. Moreover, current density curves at the centerline and sidewalls of the narrow microtrench are indistinguishable from each other. Consequently, for the narrow microtrench, current density is spatially uniform, while for the wide microtrench, the current density is seen to vary spatially, with a higher value toward the sidewalls, which is particularly evident near the end of the process. The effects of the micromold geometry and voltage on the current density distribution has been further investigated in the previous work[37].

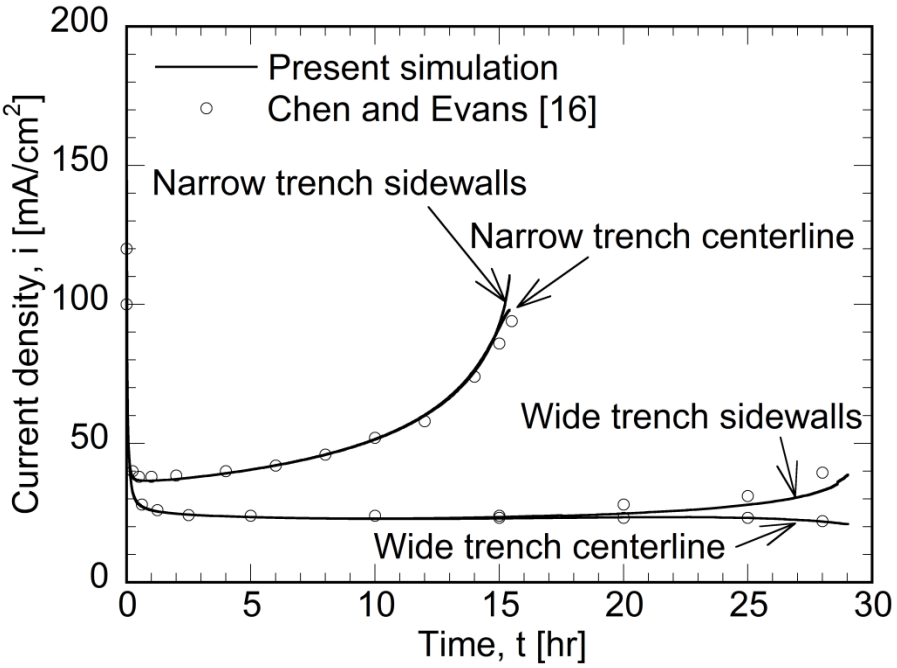

Figure 26: Validation of the present numerical simulation with the results of Chen and Evans [16] for an applied voltage magnitude V_0 = 0.6 V.

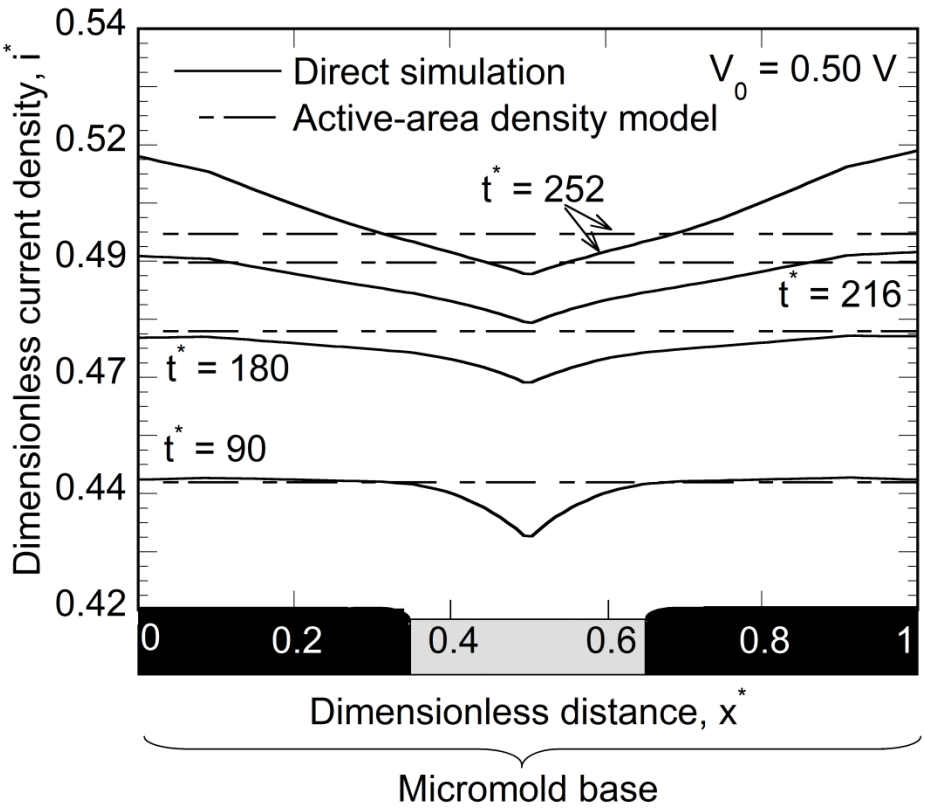

Figure 27: Results of the "active area density" model, dashed lines, and direct method, solid lines, for a microtrench with $\boldsymbol{W^* = 1}$, $\boldsymbol{d_0^* = 0.3}$ and $\boldsymbol{r_0^* = 0.02}$ by applying V_0= 0.50 V on the cathode.

Model formulation in section 2.1 may be directly used for an electrodeposition process through a secondary micromold, considering Eq (53)b as the boundary condition along the conductive parts of the micromold base throughout the deposition process. In the direct model, a change of the model schematic occurs when the insulating parts of the micromold base are completely covered by the deposit and the insulating boundary condition along the deposition surface is eliminated. The topological change of the model schematic results in an instability of the ALE method with the model failing at a higher potential magnitude. If a low external potential of -0.50 V is applied (V_0 = 0.50 V) in electrodeposition through a secondary micromold with dimensionless width (W^* = W / H) of 1, the direct model continues to the dimensionless time of 252. The result of the direct

model at this region is shown by the solid lines in Figure 27 as the variation of the dimensionless current density with the dimensionless distance, x^*. As depicted in the schematic of the micromold base along the x^* axis of Figure 27, a single insulating hole with the dimensionless size ($d_0^* = d_0 / H$) of 0.3 is considered at the center of the micromold base, while the other parts of the micromold base shown by the black color in Figure 27 are conductive. The conductive and insulating parts are connected by the fillets with the dimensionless size ($r_0^* = r_0 / H$) of 0.02. The results of the direct model may be compared with those of the "active-area density" model shown by the dashed lines in Figure 27. At all the deposition times, which are shown in Figure 27 to be less than t_{ex}, uniform current density along the micromold base is obtained from the "active-area density" model and the "edge effect" is assumed negligible. As a result of this assumption, the solution of the "active-area density" model deviates from that of the direct model close to the microtrench sidewalls. This deviation has been shown by the differences between the dashed and solid lines close to the vertical axis of Figure 27. In this figure, the maximum error of the "active-area density" model due to the negligible "edge effect" assumption is 3.3 %, which occurs at the dimensionless time of 252. The direct model also results in a smaller current density along the surface of the cleavage formed on the deposit surface above the insulating hole. This is attributed to the lower concentration of nickel ions along the cleavage surface compared to that along the flat parts of the deposition front. This deviation of the "active-area density" model from the direct model is depicted in Figure 27 by the differences between the solid and dashed lines close to the middle section of the x^* axis. The differences are more pronounced near the start of the deposition process and reduce gradually as the size of the cleavage decreases. In Figure 27, the maximum error of the "active-area density" model at the center of the x^* axis is 2.8 %, which is seen at the dimensionless time of 90.

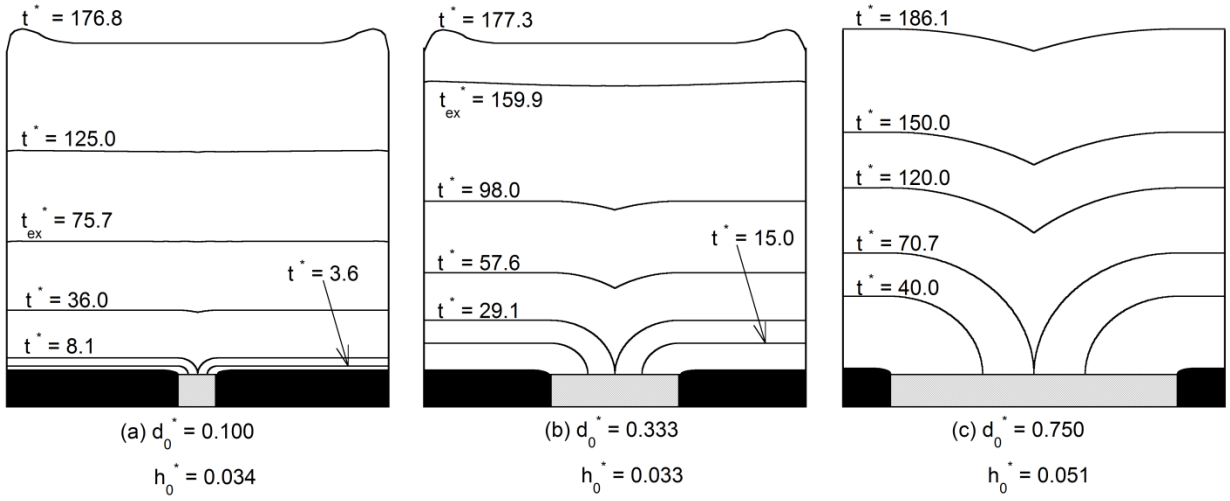

Figure 28: Time-evolution of the electrodeposition front for voltage magnitude of V_0= 0.60 V through a microtrench with $\boldsymbol{W^* = 1}$ and dimensionless hole size of $\boldsymbol{d_0^*}$ = (a) 0.100, (b) 0.333 and (c) 0.750. $\boldsymbol{h_0^*}$ shows dimensionless overplating amount for each case.

Figure 28a–c show the time-evolution of the electrodeposition front when the potential magnitude of 0.6 V is applied to fill the micromolds containing a single insulating hole with the respective dimensionless size of 0.100, 0.333, and 0.750 at the center of their bottom surfaces. Deposition starts from the conductive parts of the micromold base, shown by the black areas in Figure 28a–c, and covers the whole insulating part (the hatched section) at dimensionless times of 8.1, 29.1, and 70.7, respectively. Before these times, the actual surface area of the deposit and consequently, the active-area density increase with time. At the aforementioned deposition times, active-area density reaches its maximum value larger than one and a sharp cleavage is formed on the deposit surface, which is deeper in the micromold with a larger insulating hole. Later on, the size of the cleavage decreases and the deposition front approaches a flat surface which implies that the active-area density decreases by approaching one. In Figure 28a and Figure 28b, the cleavage is unnoticeable and the active-area density is nearly one at the respective dimensionless times of

75.7 and 159.5, denoted by t_{ex}^{*}. The effect of the initial insulating hole, presented by the cleavage, remains longer on the deposition front of the micromold with a larger hole. In Figure 28c, this effect remains throughout the whole deposition process and consequently, t_{ex}^{*} is not determined for the micromold shown in this figure. It is seen in Figure 28a and Figure 28b that after t_{ex}^{*}, the deposition front gradually bulges out near the micromold sidewalls while the central part of the micromold remains flat. In contrast, nonuniformity of the deposition front in Figure 28c is due to the existence of the cleavage in the middle of the deposition surface and the flat deposition front is formed close to the micromold sidewalls. Due to the nonuniform deposition front, a certain extent of overplating is necessary in each of the cases to completely fill the micromold. As indicated below the micromolds shown in Figure 28a–c, the dimensionless overplating amount ($h_0^{*} = h_0 / H$) of 0.034, 0.033, and 0.051 is obtained, respectively, for these micromolds. Although h_0^{*} is almost the same for the micromolds in Figure 28a–b, the large difference between the overplating amount of the micromold in Figure 28c with those of the micromolds in Figure 28a–b indicates that the size of the insulating hole can be fairly important on the overplating amount. The times shown below the topmost deposition fronts in Figure 28a–c are the dimensionless fill times, equal to 176.8, 177.3, and 186.1, respectively. These values indicate that the size of the insulating hole doesn't have a significant effect on the fill time.

"Edge effect" and "active-area density effect" for the micromolds in Figure 28a–c are evaluated using Eq. (47) and their respective ratio is shown in Figure 29a–c with respect to the dimensionless deposition time. Dashed lines in Figure 29a–b correspond to the deposition time t_{ex}^{*} at which the ratio of the "edge effect" to the "active-area density effect" is one. At smaller deposition times, represented by the points below the dashed lines in Figure 29a–b and

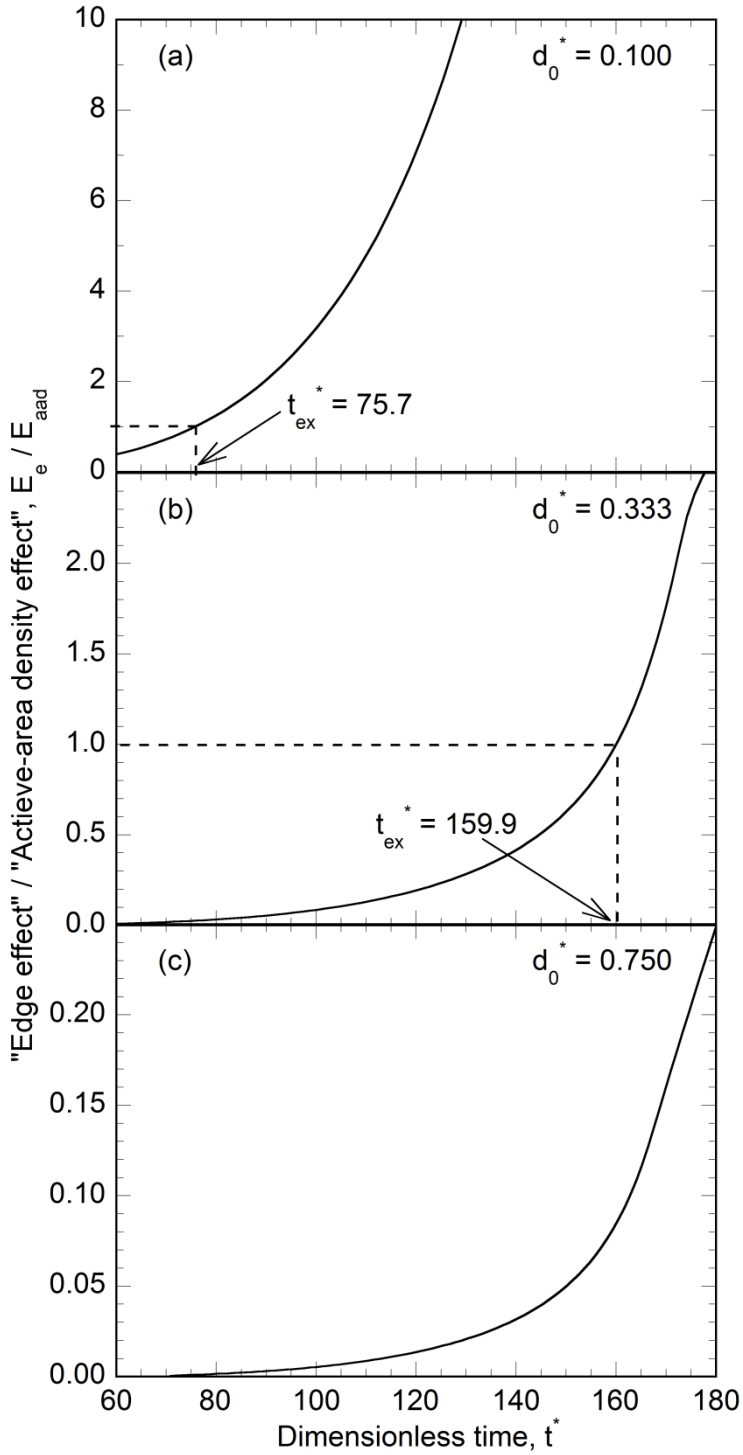

Figure 29: Ratio of E_e to E_{aad} for three geometries shown in Figs. 6a–c, respectively. When the ratio is less than one, points below the dashed line in Figs. 7a and 7b and whole range of Fig. 7c, the edge effect is neglected comparing to the " active area density" effect.

throughout the whole range of Figure 29c, the "edge effect" is neglected compared to the "active-area density effect". At these deposition times, surface nonuniformity is mainly due to the existence of the cleavage in the middle of the deposition surface and flat deposition fronts are assumed close to the micromold sidewalls, as inferred from Figure 28a–c. In contrast, at the deposition times larger than t_{ex}^{*}, represented by the points above the dashed lines in Figure 29a–b, "active-area density effect" is neglected and the model is solved considering only the "edge effect". At these deposition times, the model results in a larger deposition rate close to the micromold sidewalls and a thicker deposit is formed along the edges of the micromold opening, as shown in Figure 28a–b.

Figure 30a–b present variation of the dimensionless actual current density with the dimensionless distance along the width of the micromold with respective dimensionless hole size of 0.100 and 0.333, at the same deposition times depicted in Figure 28a–b, respectively. For the deposition times less than t_{ex}^{*}, uniform current density is obtained along the conductive parts of the deposition surface, which has been shown by the straight lines in Figure 30a–b for the deposition times less than 75.7 and 159.9, respectively. The straight lines of the current density at the smallest deposition times shown in Figure 30a–b, $t^{*} = 3.6$ and 15, respectively, are interrupted in the center. At these deposition times, the insulating hole has not completely been covered by the deposit, as inferred from Figure 28a–b, and therefore, the current density drops to zero along the exposed part of the insulating hole. Moreover, at these deposition times active area density is smaller than the next deposition times shown in Figure 30a–b, $t^{*} = 36$ and 29.1, respectively, at which the insulating hole is completely covered by the deposit. Consequently, larger current densities are obtained from Eq (42) at the deposition times of 3.6 and 15, compared to the deposition times of 36 and 29.1, respectively. Lateral variation of the current density due to the "edge effect" starts at t_{ex}^{*} and

results in a smaller current density at the central parts of the micromold compared to the sidewalls. As a result, a thicker deposit is formed along the micromold

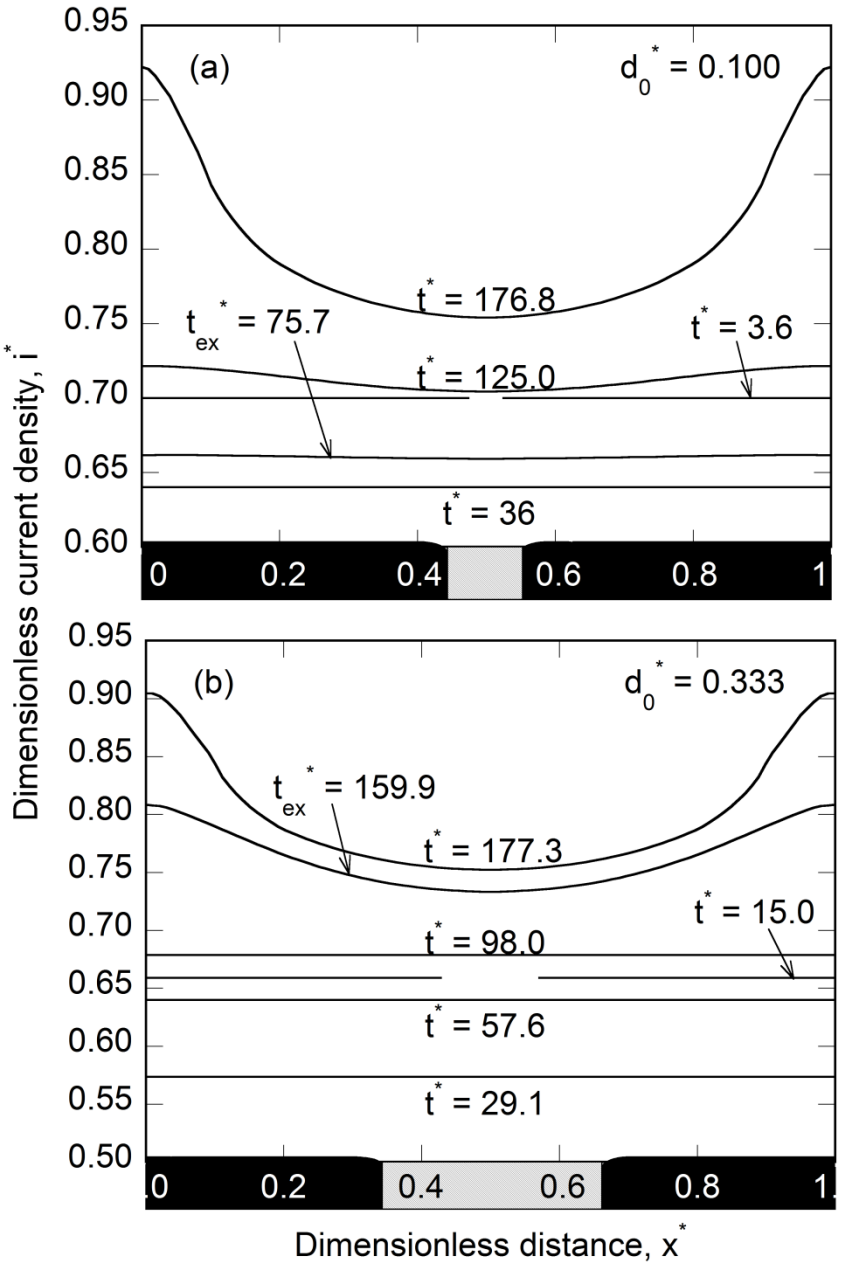

Figure 30: Variation of the dimensionless current density across the width of the microtrench with the same geometries as Figs. 6a and 6b, respective.

sidewalls, as depicted in Figure 28a–b. A comparison of the last current density curves in Figure 30a and Figure 30b shows that lateral variation of the current density at the fill time is larger for the micromold with a smaller hole size. This is also inferred from the overplating amount shown in Figure 28a–b, which is higher for the micromold with a smaller hole size. This effect of the hole size on the overplating amount is attributed to the effect of the hole size on t_{ex}^{*}. For the micromold with a smaller hole size, t_{ex}^{*} is smaller and the "edge effect" is the controlling parameter throughout the larger extent of the deposition time; therefore, larger lateral variation of the current density is obtained for this micromold at the fill time.

The effect of potential magnitude, V_0, on the time-evolution of the deposition front may be explained by comparing the profiles shown in Figure 28a–b for the potential magnitude of 0.6 V with those presented in Figure 31a–b and 9c–d for the potential magnitudes of 0.7 V and 0.8 V, respectively. For each potential magnitude, the time-evolution of the electrodeposition front through two micromolds with the dimensionless hole sizes, d^{*}, of 0.05 and 0.166 is presented. In Figure 31a–d, the bottommost profiles correspond to the complete coverage of the insulating hole, while the deposit surface profiles at t_{ex}^{*} and the fill time have been shown by the middle and topmost curves, respectively. It is observed that as the potential magnitude increases from 0.6 V (Figure 28a–b) to 0.8 V (Figure 31c–d), the dimensionless fill time decreases from 176.8 (Figure 28a) to 121.8 (Figure 31c) for the micromold with $d^{*} = 0.100$ and from 177.3 (Figure 28b) to 120.2 (Figure 31d) for the micromold with $d^{*} = 0.333$. It is also noted that an increase in the potential magnitude from 0.6 V in Figure 28a–b to 0.8 V in Figure 31c–d results in an increase in the overplating amount of the micromolds with $d^{*} = 0.100$ and $d^{*} = 0.333$ from 0.034 (Figure 28a) to 0.089 (Figure 31c) and from 0.033 (Figure 28b) to 0.073 (Figure 31d), respectively. These variations of the fill time and overplating amount with the potential magnitude are attributed to the

higher current density and increased nonuniformity in current density at higher potential magnitudes. Comparing the bottommost curves in Figure 31a and Figure 31b with the ones in Figs Figure 31c and Figure 31d, respectively, shows that the insulating hole at the micromold base is covered faster by the deposit if a higher potential magnitude is applied, though the shape of the deposit surface profile at the time of the complete coverage of the insulating hole is independent of the potential magnitude. As a result, at higher potentials, the cleavage formed on the deposit surface vanishes sooner, which is also inferred from the smaller t_{ex}^{*} in Figure 31c and Figure 31d compared to the t_{ex}^{*} in Figure 31a and Figure 31b, respectively. Therefore, at higher potential magnitudes, "edge effect" controls the process throughout a larger extent of the deposition time, which results in more nonuniformity in current density at the fill time.

Based on the results in Figure 31, a higher potential magnitude leads to a reduction in the fill time, whereas smaller potential magnitudes are preferred from the viewpoint of minimizing the amount of overplating. In the previous work[37], the optimum potential, which minimizes the fill time and the overplating simultaneously, was determined for different micromold geometries in the electrodeposition through a primary micromold. In this work, it is desirable to evaluate the optimum potential in the electrodeposition through a secondary micromold and compare that with the results presented in the previous work in order to determine the effect of the insulating hole on the optimum potential. To this end, the potential magnitude, V_0, which minimizes the product of dimensionless fill time and overplating, $t_{fill}^{*}.\square_{0}^{*}$, is sought as the optimum voltage that simultaneously minimizes the fill time and the overplating height. Figure 32 shows the variation of the product function, $t_{fill}^{*}.h_{0}^{*}$, with the potential magnitude, V_0, for two micromolds presented in Figure 28a–b. The minimum point on each plot yields the optimum potential magnitude for each micromold. It is seen that the optimum potential magnitude occurs at the same point, V_0 = 0.6 V,

for the micromolds with different dimensionless hole sizes of 0.100 and 0.333. The optimum potential magnitude of 0.6 V was also obtained for a primary micromold with equal height and width in the previous work[37]. These results show that the existence of the insulating

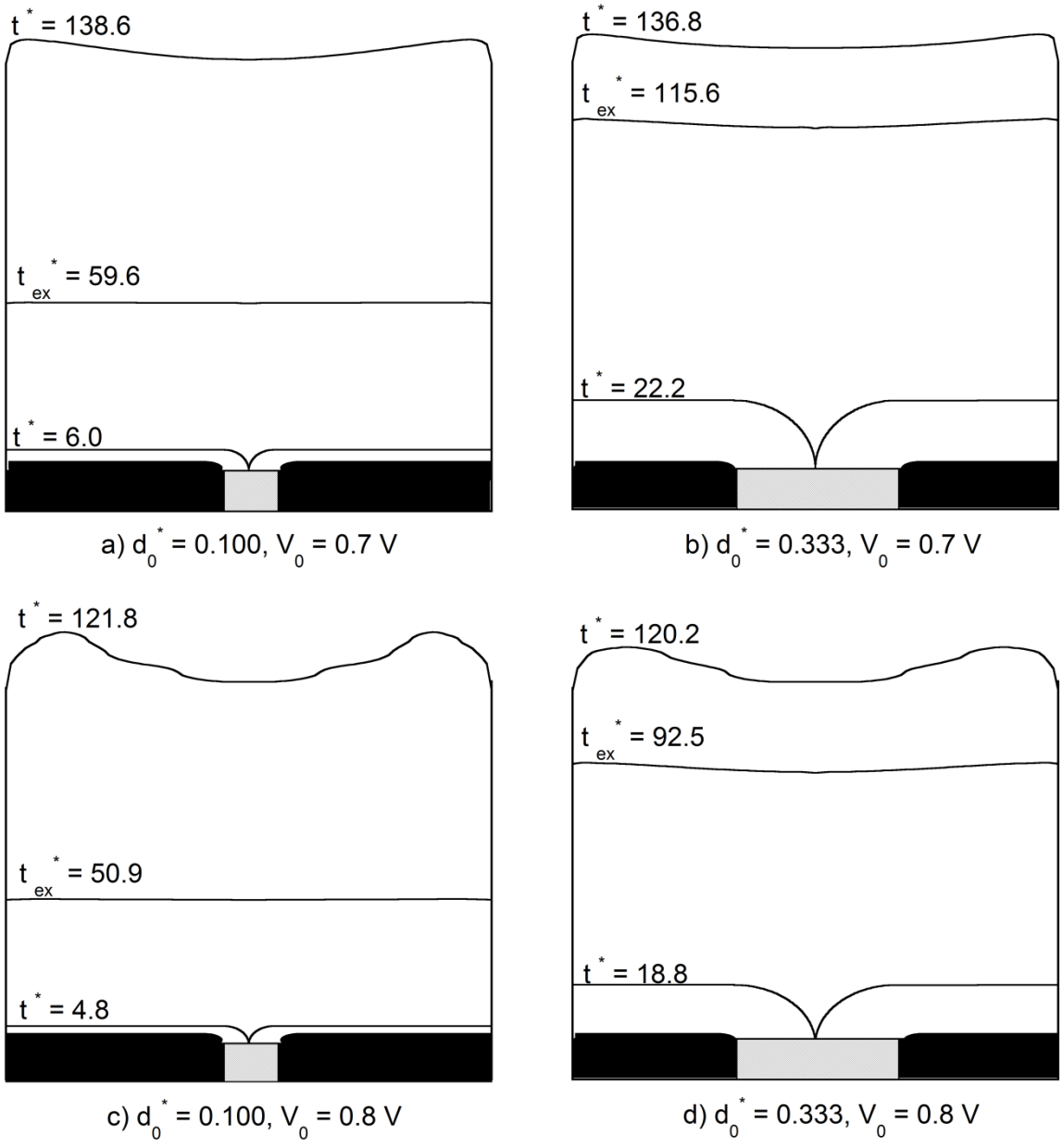

Figure 31: Time-evolution of the electrodeposition front for voltage magnitude of V_0= 0.70 V, (a) and (b), and V_0= 0.80 V, (c) and (d), through a microtrench with $\boldsymbol{W^*} = \mathbf{1}$ and dimensionless hole size of $\boldsymbol{d_0^*} = 0.100$, (a) and (c), and 0.333, (b) and (d).

hole at the micromold base does not have any effect on the magnitude of the optimum potential, which mainly depends on the micromold size, W^*, as discussed in the previous work.

Figure 34a–c show the time-evolution of the deposit surface profile when the optimum potential magnitude of 0.6 V is applied to fill the micromold which contains 3, 5, and 7 evenly distributed insulating holes, respectively. The insulating holes are of the same size, d^* = 0.100, and have been presented in Figure 34a–c by an array of evenly distributed hatched sections on the micromold base. The three deposit surface profiles shown in these figures from the bottom to the top of the micromolds correspond to the complete coverage of the insulating hole, t_{ex}^*, and fill

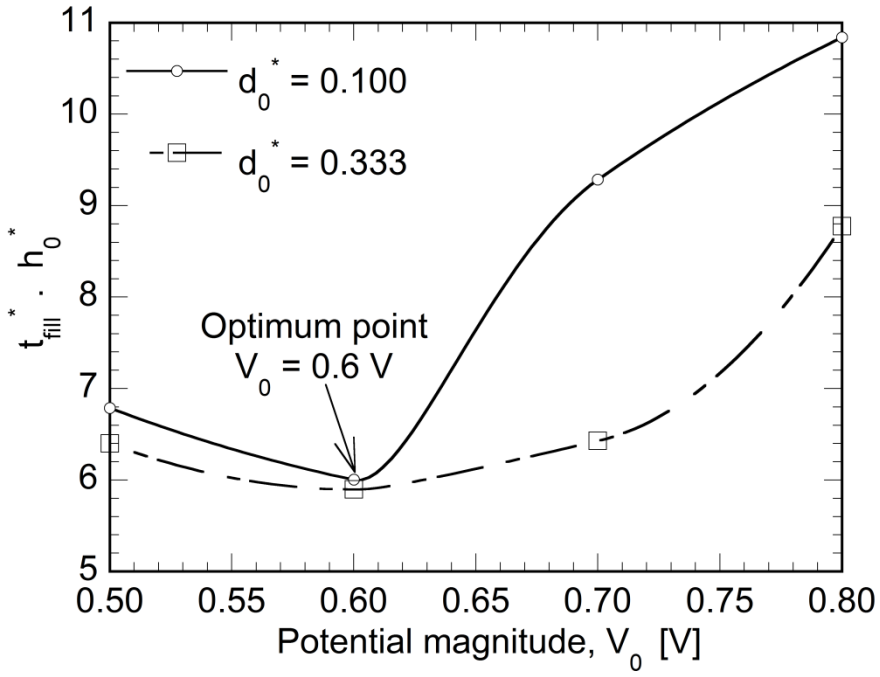

Figure 32: The variation of the product function, $t^*_{fill}.h^*_0$, with the magnitude of the applied voltage, V_0, for a microtrench with $W^* = 1$ with two different dimensionless hole sizes of 0.100 and 0.333.

time, respectively. A comparison of Figure 28a, Figure 34a, Figure 34b, and Figure 34c shows that the number of the insulating holes has negligible effect on the overplating amount and the times corresponding to the complete coverage of the insulating holes and complete fill of the micromold. For the micromolds with 1, 3, 5, and 7 insulating holes, complete coverage of the insulating holes and complete fill of the micromold occur at almost the same dimesionless times of 8.0 and 176.5, respectively. Moreover, for all of these micromolds, the dimensionless overplating amount is around 0.034.

Figure 33 shows the ratio of the "edge effect" to the "active-area density effect", E_a/E_{aad}, with respect to the dimensionless time for the micromolds shown in Figure 28a and Figure 34a–c with 1, 3, 5, and 7 evenly distributed insulating holes, respectively. The dashed line in Figure 33 corresponds to the deposition time t_{ex}^{*} at which the "edge effect" is equal to the "active-area density effect". It is noted from this figure and the results shown in Figure 28a and Figure 34a–c that t_{ex}^{*} is slightly higher for the micromold with a larger number of insulating holes, because "active-area density effect" controls the deposit surface profile of this micromold throughout the larger extent of the deposition time. In addition, a comparison of Figure 33 with Figure 29a–c reveals a minimal effect of the hole number on t_{ex}^{*} compared to the effect of the hole size. In Figure 28a, the micromold contains a single insulating hole with the same size as the cumulative size of the three insulating holes at the micromold base in Figure 34a. A comparison of t_{ex}^{*} in these two micromolds shows that a single hole with a larger size exerts more "active-area density effect", which lasts longer compared to several smaller holes with the same cumulative size. This explanation can be used to justify the negligible effect of the hole number compared to the hole size on the overplating amount and fill time.

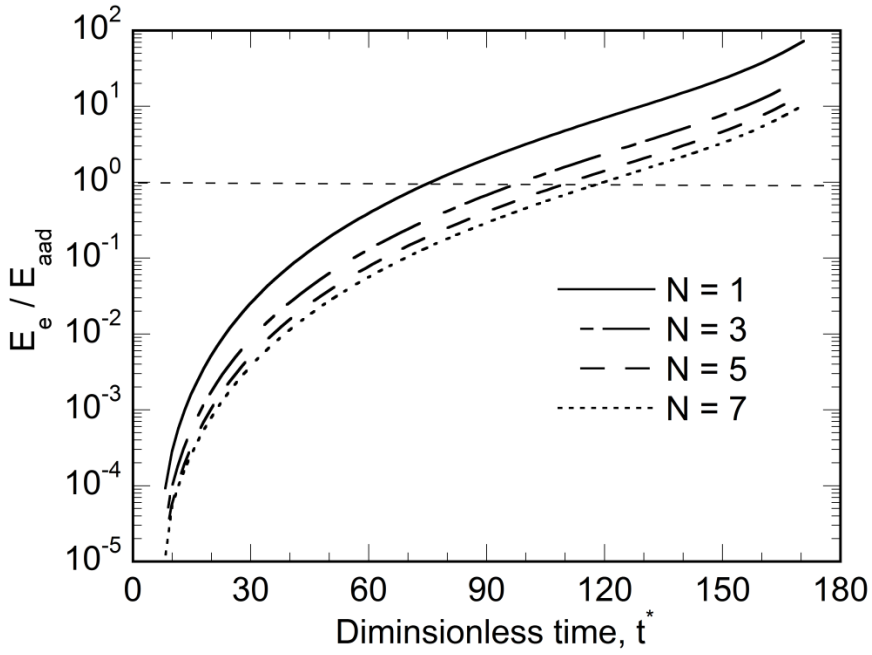

Figure 33: Ratio of E_e to E_{aad}, in the log scale for the geometries shown in Figs.6a and 11a–c with 1, 3, 5 and 7 evenly distributed insulating holes, respectively.

Figure 35a–b show the effect of the hole size and hole number, respectively, on the variation of the dimensionless average current density, i_{ave}^*, with respect to the dimensionless deposition time, t^*, when the optimum potential magnitude of 0.6 V is applied. i_{ave}^* of a primary micromold, which is also shown in Figure 35a, sharply decreases at the small deposition times because of the initial reduction of the ion concentration on the deposition surface before the steady state condition. For the secondary micromolds, the initial decrease in i_{ave}^* also occurs due to the increase in the active-area density before the complete coverage of the insulating hole. Active-area density reaches its maximum value at the time the insulating hole is completely covered by the deposit which corresponds to the minimum i_{ave}^* of the secondary micromolds in Figure 35a–b. The larger maximum of the active-area density and, consequently, the smaller minimum of i_{ave}^* is obtained for a micromold with larger hole size or greater number of insulating holes, as seen in

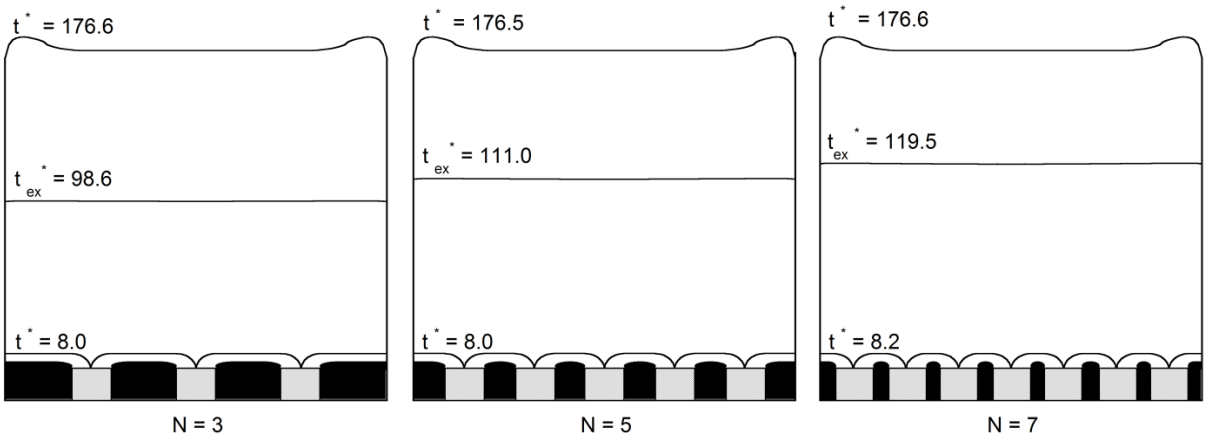

Figure 34: Time-evolution of the electrodeposition front for voltage magnitude of V_0= 0.60 V through a microtrench with $\boldsymbol{W^* = 1}$ and (a) 3 (b) 5 and (c) 7 evenly distributed insulating holes, $\boldsymbol{d_0^* = 0.100}$, on the electrode surface.

Figure 35a and the inset of Figure 35b, respectively. For the primary micromold, the slight increase in i_{ave}^* after the sharp initial decrease occurs when the surface concentration reaches the steady state value, due to the change of the position of the deposition surface with time. For the secondary micromolds, the increase in i_{ave}^* also occurs due to the decrease in the active-area density. Consequently, the i_{ave}^* curves of the secondary micromolds rises faster after the minimum than the curve of the primary micromold. As seen in Figure 35a, the curves of the secondary micromolds finally approach that of the primary micromold because after t_{ex}^*, the effect of the initial insulating hole on the deposit surface profile is negligible and, similar to the primary micromold, the surface profile of the secondary micromold is mainly controlled by the "edge effect".

Figure 35a shows that the variation of i_{ave}^* with deposition time is larger for the micromold with a larger insulating hole. In general, larger variation of the current density results in more nonuniformity in the microstructure of the deposit and greater grain size distribution[52, 65]. In

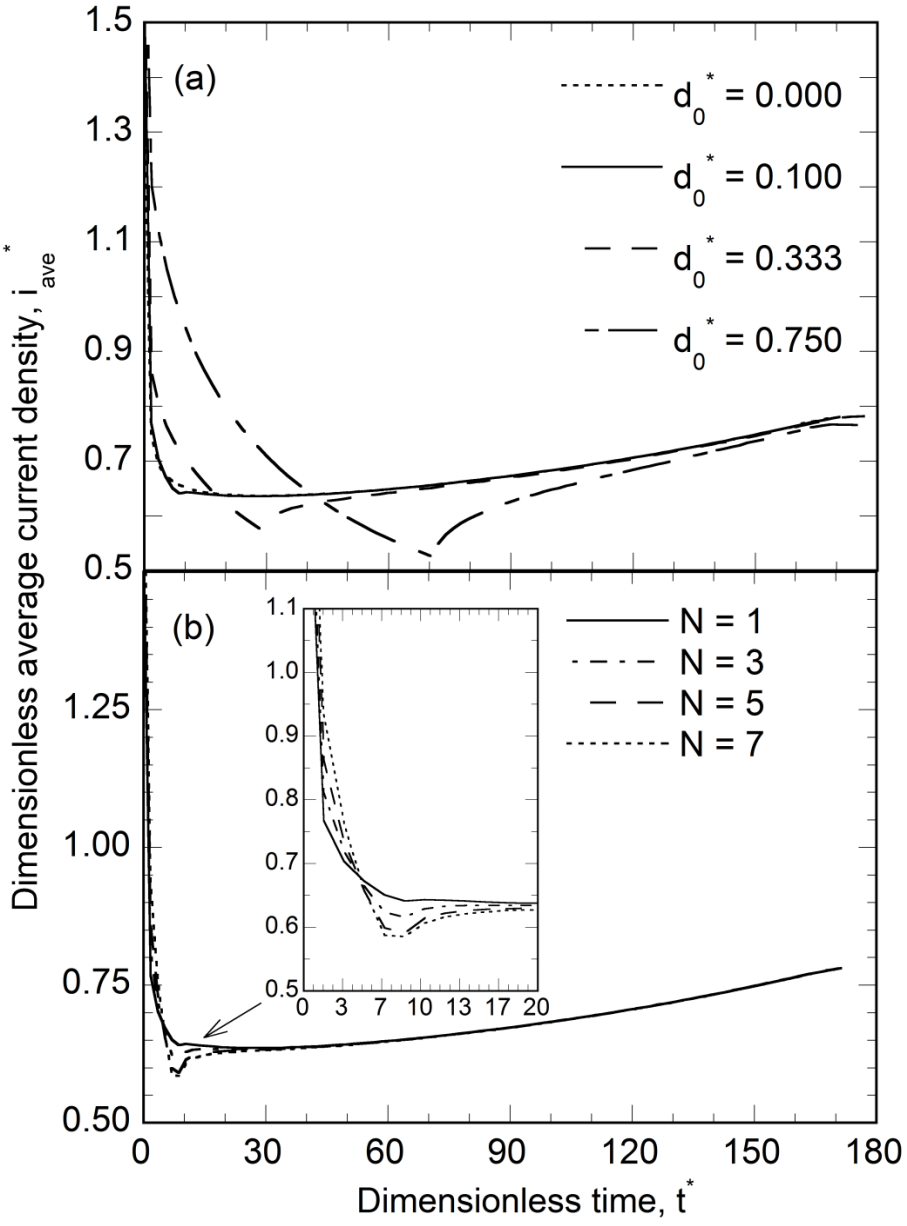

Figure 35: Dimensionless average current density as a function of dimensionless time for voltage magnitude of V_0= 0.60 V, through a microelectrode with equal height and width considering different (a) hole size ($\boldsymbol{d_0^* = 0.000, 0.100, 0.333, 0.750}$) and (b) number of holes while $\boldsymbol{d_0^* = 0.100}$ (N = 1, 3, 5, 7).

addition, the concentration of additives and impurities entrapped in the deposit structure is higher when the current density is larger. The standard deviations of 0.06, 0.08, and 0.20 are obtained for the curves corresponding to the respective dimensionless hole sizes of 0.100, 0.333, and 0. 750 in Figure 35a. Therefore, i^*_{ave} of the micromold with a larger insulating hole has greater variation with time and consequently, more nonuniformity in the microstructure is expected for the deposit formed within this micromold.

A comparison of Figs 13a and 13b shows that the effect of the hole number on the current density variation is less than the effect of the hole size. In fact, the curves in Fig 13b completely overlap except at the region shown in the inset of this figure. The order of the curves reverses at the middle of this region; for example, a curve with the largest current density at the first part of this region has the smallest current density at the second part of this region. Consequently, the difference in i^*_{ave} at the region shown in the inset of Fig 13b does not exert any overall effect on the fill time and overplating amount of the micromolds with different number of insulating holes. This explanation may be used to justify the negligible effect of the hole number on the fill time and overplating amount.

Chapter 5: Superhydrophobic Copper Surfaces via Two-step Electrodeposition Technique

The work presents a template-free electrochemical route to make superhydrophobic copper coatings with the water contact angle of 160º ± 6° and contact angle hysteresis of 5° ± 2°. In this technique, copper deposit with multiscale surface features is formed through a two-step electrodeposition process in a concentrated copper sulfate bath ($CuSO_4$ 1 M and H_2SO_4 0.5 M). In the first step, applying a high overpotential results in the formation of fractal-shaped structures, which are loosely attached to the surface. In the second step, an additional thin layer of the deposit is formed by applying a low overpotential for a short time, which is used to reinforce fractal-shaped branches on the surface. This low-cost, simple technique for coating metallic surfaces with an enduring superhydrophobic film does not require any chemical modification or application of an additional layer of a low surface energy material. Moreover, it can be utilized to make a uniform coating in a short time regardless of the surface size and shape. The work also presents a theoretical explanation for the effects of the fabrication parameters on the surface texture of the deposit. This explanation shows that at high overpotential in a concentrated bath, the electrodeposition is so unstable that branches which become detached from the deposit surface can grow independently in the electrolyte. This unstable growth process results in the formation of the fractal-shaped structures which are known as the main reason of the superhydrophobic characteristic of the deposit.

5.1 Introduction

Engineering micro-nano scale texture of the surfaces achieved a great interest in the recent years

due to its importance in both fundamental research and practical applications[33, 66-70]. In particular, it was a great focus on superhydrophobic surfaces inspired by lotus leaf effect[71]. On these surfaces, a sessile droplet shows apparent contact angle higher than 150°; in addition, a dynamic droplet dose not stick to these surfaces[21-26]. Several methods were presented in the literature to demonstrate and measure the non-wetting characteristic of a superhydrophobic surface. For example, it is shown that a falling droplet bounces off after hitting a superhydrophobic surface[72]. Moreover, low contact angle hysteresis, i.e. small difference between the contact angles at the front and back of a moving droplet, is another method to show non-wetting characteristic of a surface[73-75]. It is already known that proper design of surface topographical features is required to support the aforementioned criteria for superhydrophobicity[76-78]. In particular, roughness at two or more length scales has been presented as the cause of superhydrophobicity in the lotus leaf and other naturally superhydrophobic materials[79, 80]. A sessile drop interacting with a rough surface may fully wet the surface which is known as the Wenzel wetting regime (WE)[81] or it may result in Cassie-Baxter regime (CB) in which air pockets are entrapped underneath the drop and a composite interface (liquid-solid-air)[82] is formed. Reduction of the liquid-sold contact area in CB regime results in both high apparent contact angles (α) and low contact angle hysteresis; therefore CB regime supports the criteria of superhydrophobicity.

Until now, many methods have been developed to fabricate superhydrophobic surfaces, such as sol-gel processing[83, 84], self-assembly technique[85-88], electrospinning[89], hydrothermal synthesis[90], laser etching[91], plasma etching[92], physical and chemical vapor deposition[93], anodic oxidation[94], and spray method[95]. Some of the fabrication techniques presented in the literature for making superhydrophobic surfaces are costly and time-consuming. These techniques

are not ideal for making superhydrophobic coatings with industrial applications, which require facile and time-saving fabrication techniques. For some of these applications, the effects of the superhydrophobic coating on thermal and electrical conductivity of the substrate should be minimized; therefore, insulating coatings presented in most of the previous works are not applicable. Among the conductive coatings, superhydrophobic copper coating has attracted considerable interest due to its high diathermanous and electric performance in addition to its good thermal and mechanical stability[96-101]. In some of the techniques presented in the literature for making superhydrophobic copper surfaces, besides formation of surface topographical features, the chemistry of the copper surface is changed, which may result in undesirable changes in the essential surface properties[99]. In addition, in some of these techniques, the topmost layer of the copper surface is transformed to a superhydrophobic film while for most of the applications, coating a substrate with an additional layer of a superhydrophobic copper film is required.

Electrodeposition is a well-known coating technique which can be utilized to make uniform coatings regardless of the surface size and shape[102]. Template-assisted electrodeposition has been utilized previously to coat surfaces with a patterned layer of a superhydrophobic metal deposit[101, 103, 104]. In this technique, texture of the deposit depends on the template structure and might be adversely affected by the template fabrication step. Due to this reason, template-free electrodeposition methods have gained more interest and applications. Wang et al.[105] presented a method to directly deposit hierarchical spherical cupreous microstructures from an aqueous solution of $Cu(NO_3)$ by applying a constant overpotential and further hydrophobized the deposit surface by a self-assembled monolayer of *n*-dodecanethiol. Wang et al.[106] used a two-step procedure to deposit a hydrophobic copper film: the first step at a low overpotential in order to create nucleation sites and the second step at a high overpotential for the growth of particles on the

nucleation sites. Afterward, they enhanced the wettability of the copper deposit to the superhydrophobic region by applying a self-assembled monolayer of an n-alkanoic acid. Shirtcliffe et al.[107] made a fractal-shaped copper deposit by applying a specific current density and further made the deposit superhydrophobic using a layer of a fluorocarbon coating. In the aforementioned works, morphological instabilities which are inherently made during electrodeposition[17-20] are enhanced by applying an appropriate overpotential or current density. These instabilities provide the surface texture required for the hydrophobic state but in all these works, superhydrophobicity is not obtained without applying an additional layer of a low surface energy material. The endurance of this additional layer strongly affects the superhydrophobic characteristic of these surfaces and therefore, delamination of this layer is a serious issue for the superhydrophobic surfaces made using these techniques.

Though surface texture of an electrodeposited film can be controlled by changing both current density and overpotential, overpotential is more appropriate parameter to alter morphological instabilities made during electrodeposition. This is because, unlike overpotential, current density is bounded by a maximum value called limiting current density which corresponds to the mass transfer limitation of the system. After reaching the limiting condition, the current density remains constant with increasing overpotential and the change of the deposit surface structure should be attributed to the change of the overpotential. This work presents an experimental investigation on the effect of the overpotential on the surface texture of the copper deposit. As a result of this investigation, a novel two-step electrodeposition technique is developed to fabricate a superhydrophobic copper coating which does not require applying an additional layer of a low surface energy material. In the first step, applying a high overpotential in a concentrated electrolyte results in the formation of fractal-shaped structures, which are loosely attached to the surface. In

the second step, an additional thin layer of the deposit is formed by applying a low overpotential for a short time, which is used to reinforce the loosely-attached structures on the surface. This method is a potentially low-cost and simple approach for coating metallic surfaces with an enduring superhydrophobic film which is totally made of copper. In addition to the experimental investigation, this paper also presents a theoretical explanation, based on similar models presented in the literature on thermal solidification[27], to explain formation of the morphological instabilities during electrodeposition. This theoretical explanation shows that though deposit growth is always unstable, the instability is enhanced by applying a larger overpotential or using a more concentrated electrolyte.

The article is organized as follows: The experimental methods and fabrication technique are described in the next section, followed by a presentation and discussion of the results of the study. In the last section, a theoretical model which explains the experimental observations is presented.

5.2 Experimental Methods

Reagents. Though presence of impurities containing sulfur and hydrogen in the structure of copper deposit which is formed in a copper sulfate bath is inevitable, using analytical grade chemicals is important for accurate experimental results [41, 42]. Impurities other than the electrolyte species adversely influence the reproducibility of the experiment because they have uncontrolled effects on the mass transfer process in the bath and on the surface characteristic of the electrode [43]. Therefore, in this work analytical grade $CuSO_4$ and H_2SO_4 supplied by Fisher Chemicals (Pittsburgh, PA, USA) were used. In addition, deionized water with resistivity of 18 MΩ.cm (Millipore Corp., Billerica, MA, USA) was utilized for making all solutions.

Electrodeposition Experiments. Electrodeposition was performed using an AUTOLAB PGSTAT128N potentiostat (ECO Chemie, Utrecht, The Netherlands). A traditional three-electrode system was employed in which a copper sheet and a platinum mesh were utilized as the reference electrode and anode, respectively. As used herein, the term "substrate" refers to a surface, part, or item to which a coating is applied. Substrate plays the role of the cathode in the electrodeposition process. In this work, the substrate was a 0.7×0.6 cm^2 silicon wafer covered by a smooth copper film using physical vapor deposition (PVD). Furthermore, a concentrated electrolyte composed of $CuSO_4$ 1 M and H_2SO_4 0.5 M was used in this work. To remove oxygen from the electrolyte, it was bubbled for 15 minutes before fabricating each sample. Moreover, the electrolyte was replaced by a new solution after fabricating three samples to avoid contamination. Since the reference electrode was composed of the same material as the deposit, herein, the term overpotential is used to refer to the electric voltage. A constant negative overpotential was applied to coat substrate with a copper film. However, in this paper, the overpotential, is referred to by its absolute value, η. In order to investigate the effects of the overpotential on the deposit morphology, different overpotentials in the range of 0.1 V to 1.3 V were applied to deposit copper coatings with 30 μm thickness on the substrate.

Characterization. The surface morphologies of the deposited coatings were examined using the FEI Quanta 600 scanning electron microscope (SEM). The PHI Quantera x-ray photoelectron spectroscopy (XPS) was utilized to obtain the chemical state of the deposit. In order to show the reentrant geometry of the deposit topographical features, the cross section of one of the surface structures was revealed through a cut made by a focused ion beam using the FEI Helios 600 NanoLab.

Measurement of the Wetting characteristic. Droplets of deionized (DI) water with 4.5 µl volume were used in all wetting experiments. In order to investigate the effects of the overpotential and electrolyte concentration on the wetting characteristic of the deposit, the static contact angles of the droplet was obtained using FTÅ 200 contact angle measurement system at the room temperature. At each overpotential and electrolyte concentration, two samples were fabricated and on each sample .three contact angle measurements were performed. Angles were deduced from the measurements using the ImageJ software [108, 109]. The contact angle hysteresis of a moving droplet on the superhydrophobic coating was measured five times using the same equipment. All results are reported as the mean number ± standard deviation. In order to further show the non-wetting characteristic of a superhydrophobic surface, full rebound of a falling droplet was captured at the speed of 3000 Hz by a XS-5 high speed camera (IDT; Tallahassee, FL, USA).

Fabrication of the Superhydrophobic Coating. Figure 36 shows a schematic illustration of the two-step approach to fabricate a superhydrophobic coating. Figure 36a presents the incipient formation of the cauliflower-shaped structures on the deposit surface in the concentrated electrolyte of 1 M $CuSO_4$, when overpotentials greater than 0.9 V in magnitude were applied. At these conditions, as explained in the "Theoretical Basis" section, the interface between the electrolyte and the deposit is very unstable. At this level of instability, fractal-shaped structures with multiscale roughness such as those shown in Figure 36a are formed. Consequently, the coating fabricated at these conditions show hydrophobic characteristic. The cauliflower-shaped branches get larger with time or when a higher overpotential is applied and, as a result, hydrophobicity increases. Beyond a certain stage, branches which become detached from the cauliflower-shaped structures can grow independently and the surface of the deposit is covered by loosely attached

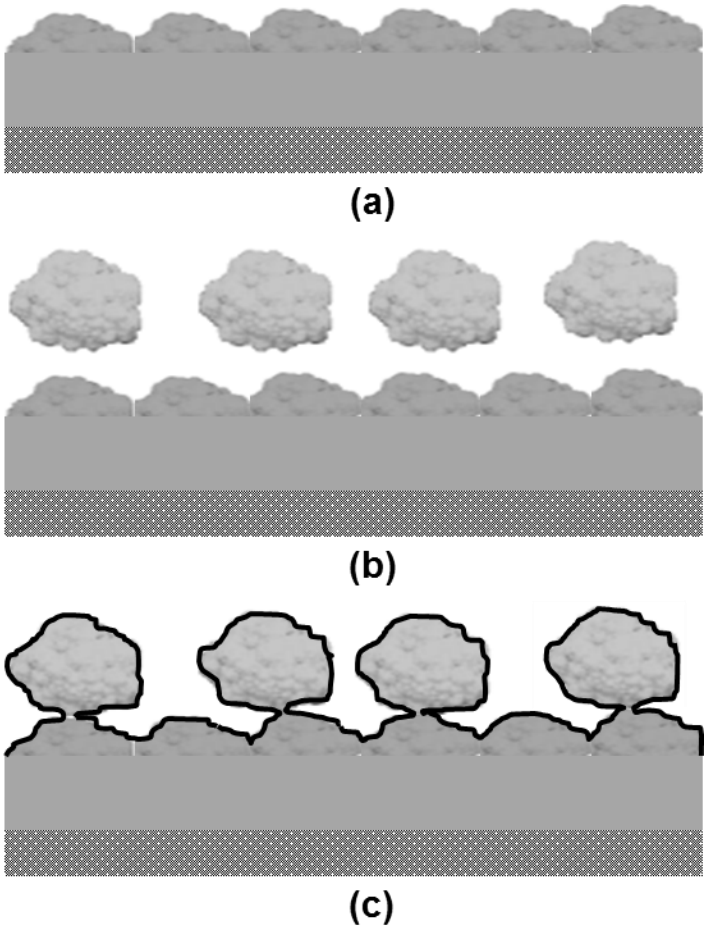

Figure 36: Schematic illustration of the two-step deposition technique: (a) (a) Cauliflower-shaped structures form on the deposit surface in a concentrated electrolyte of 1 M $CuSO_4$ when overpotentials higher than 0.9 V are applied; (b) At certain stage, with increasing time or with increasing overpotential, the branches appear detached from the surface; (c) The branches are reattached to the surface by depositing an additional thin layer (shown by the thick lines) of copper which is made by applying a low overpotential (0.15 V) for a short time (10 sec).

structures, as seen in Figure 36b. Generally, loosely attached branches are formed beyond a certain stage in all unstable growth processes but in the literature, their formation was mainly studied during thermal solidification[27]. The coating formed at the end of this first step of deposition will

be referred to as one-layer deposit in the rest of the discussion. In the present approach, the branches are reinforced on the deposit surface by an additional thin layer of copper which is made by applying a low overpotential (0.15 V) for a short duration (10 sec). This second deposit is shown by the thick line in Figure 36c. The coating obtained from the two-step electrodeposition technique will be referred to as two-layer deposit in the reminder of the discussion. The coating is hydrophobic at all three stages shown in Figure 36a-c, though surfaces displayed in Figure 36b and Figure 36c exhibit larger and more intricate topographical features, which is an important requisite for achieving higher contact angles and satisfying the requirements of superhydrophobicity.

5.3 Results and Discussion

The effect of the overpotential on the surface topography and contact angle of a one-layer deposit was studied by depositing copper coatings with 30 µm thickness at different overpotentials from an electrolyte of 1 M $CuSO_4$ and 0.5 M H_2SO_4. For each overpotential, two samples were fabricated and on each sample three contact angle measurements were performed. Figure 37a–f portray the micrographs of the surface topographies of the one-layer deposits formed by applying overpotentials in the range of 0.1 V to 1.1 V, in increments of 0.2 V, while Figure 37g–l show the median values of the contact angles, the standard deviations, and the representative shape of a 4.5 µL water droplet on the deposited surfaces. The deposit surface features are observed to change gradually from needle-shaped structures at low overpotentials (η = 0.1 V) in Figure 37a to cauliflower-shaped structures at high overpotentials (η = 1.1 V) in Figure 37f. For increase in overpotential from 0.1 V to 0.7 V, a gradual transition from needle-shaped structures in Figure 37a

and b to spherical-shaped structures in Figure 37c and d is observed. From Figure 37g–j, it is found that the needle-

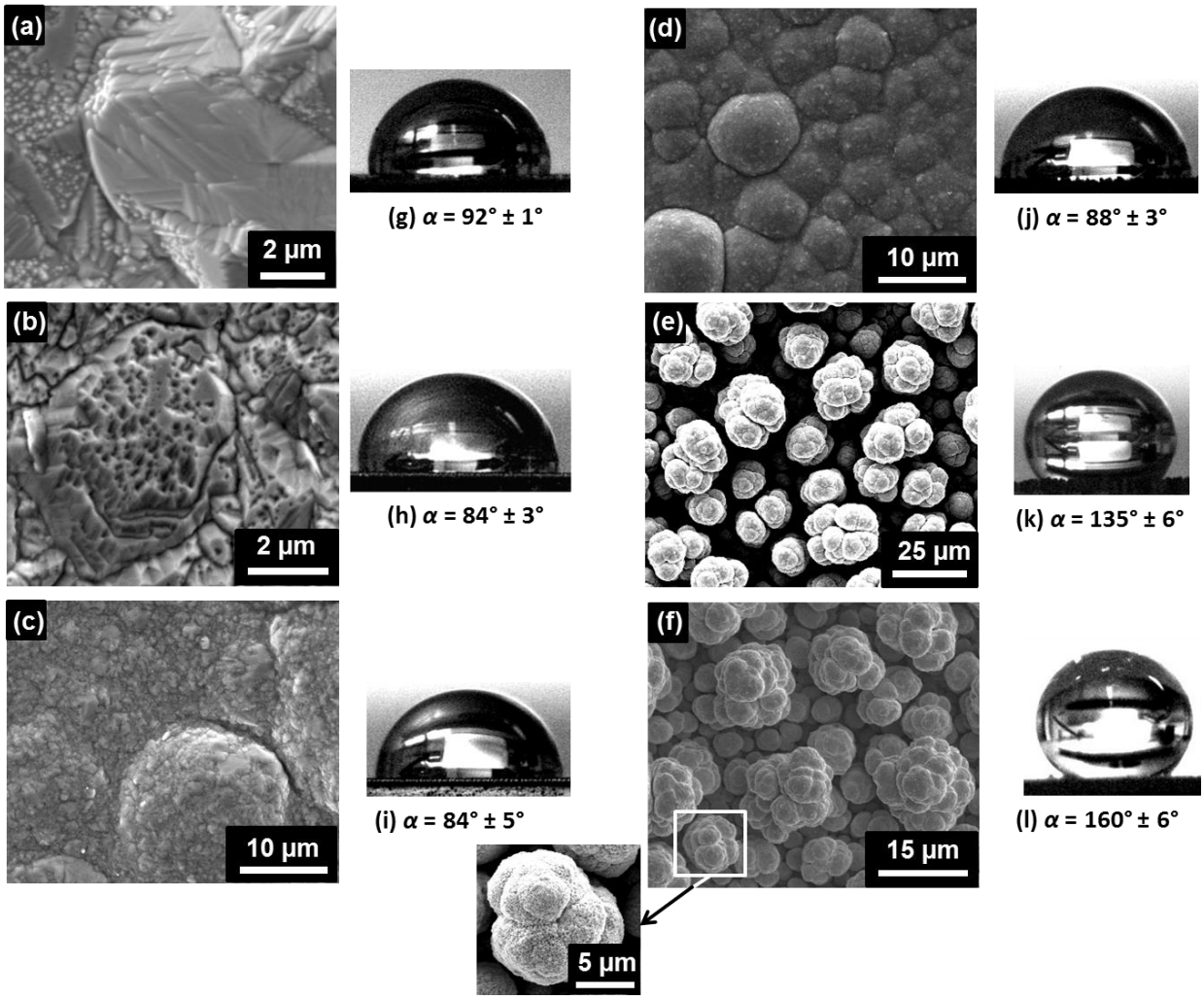

Figure 37: Micrographs (a–f) and the corresponding contact angles (g–l) of the deposits made by applying overpotentials of (a) and (g) 0.1 V, (b) and (h) 0.3 V, (c) and (i) 0.5 V, (d) and (j) 0.7 V, (e) and (k) 0.9 V, and (f) and (l) 1.1 V, respectively (The inset is a high-magnification micrograph of one of the florets on the deposit surface). The variation corresponds a standard deviation of ±1.

and spherical-shaped deposit surface textures (Figure 37a–d) have negligible effect on the contact angle, which is observed to remain in the vicinity of 90°. The results obtained for the contact

angles of these deposits agree with the value of 90° reported in the literature for smooth copper films exposed to the ambient conditions, which are always covered by a thin layer of Cu_2O[110].

At overpotentials greater than 0.7 V, when cauliflower-shaped surface features are formed (Figure 37e and f), the contact angle increases to larger values, as seen in Figure 37k and l. When water droplet is brought in contact with the deposit made by applying 1.1 V overpotential (Figure 37f), it does not leave the syringe tip. Similar to what has been reported for the lotus leaves[74], droplet is rejected by this surfaces and cannot sit on that. Those places of the deposit surface which allow the droplet to sit on them such as the one shown in Figure 37l contain a point defect. With the increase in overpotential to 0.9 V (Figure 37k) and to 1.1 V (Figure 37l), it is observed that the contact angle increases to 135° ± 6° and 160° ± 6°, respectively. This can be attributed to the increase in the number of asperities on the deposit surface with the corresponding increase in overpotential, as illustrated in Figure 37e and f. The inset displayed in Figure 37f is a high-magnification micrograph of one of the florets of the surface topography, which shows that these branches are covered by asperities of the smaller scale. This suggests the formation of fractal structures, resulting in the multiscale roughness on the coating deposited through the use of a high overpotential of 1.1 V, which is the main reason of the superhydrophobic behavior of this coating.

Figure 38a shows the footprint of a deposit surface made by applying 1.1 V overpotential on a piece of scotch tape (3M; St Paul, MN, USA). The cauliflower-shaped branches shown in Figure 37f are loosely attached to the surface and can be easily removed when the tape is peeled off from the surface. Depositing the second layer of copper by applying a low overpotential (0.15 V) for a short duration (10 sec) will fix the cauliflower-shaped branches on the deposit surface. Therefore, these branches are not removed from the surface when the tape is peeled off, as shown by the footprint of a two-layer deposit on a piece of tape in Figure 38b.

Figure 39 shows the micrograph of the two-layer deposit. In this figure the cross section of one of the florets is revealed through a cut made by ion beam. This cross section shows the reentrant geometry of the cauliflower-shaped structures which is considered as the main reason for their superhydrophobic characteristic[111]. Comparing surface features of the two-layer deposit (Figure 39) with those of a one-layer deposit (Figure 37f) reveals that applying the thin layer of the deposit in the second step does not have a considerable effect on the surface topography.

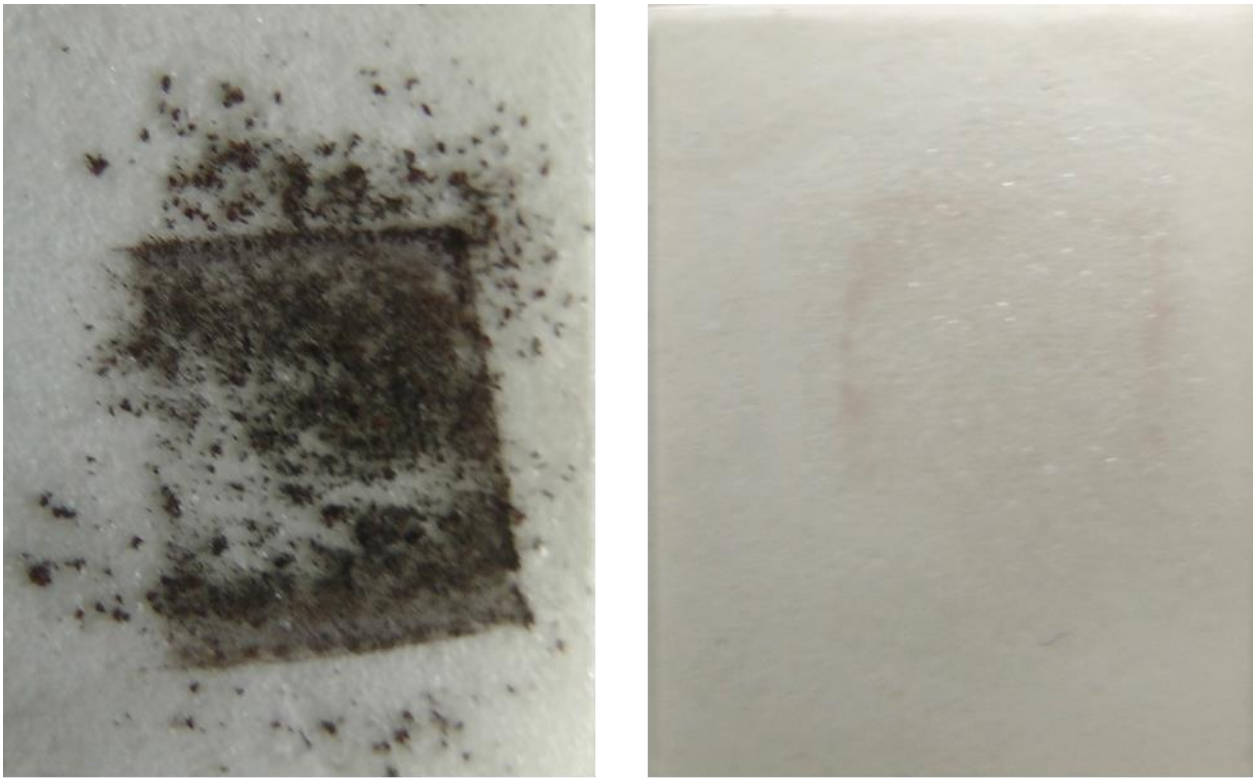

Figure 38: The footprint of (a) one-layer deposit (b) two-layer deposit on a piece of tape. The first layer is a 30 µm copper deposit made by applying 1.1 V overpotential. The second layer is a thin copper film deposited by applying *0.15 V overpotential for 10 sec and is* used to reinforce the cauliflower-shaped branches on the surface.

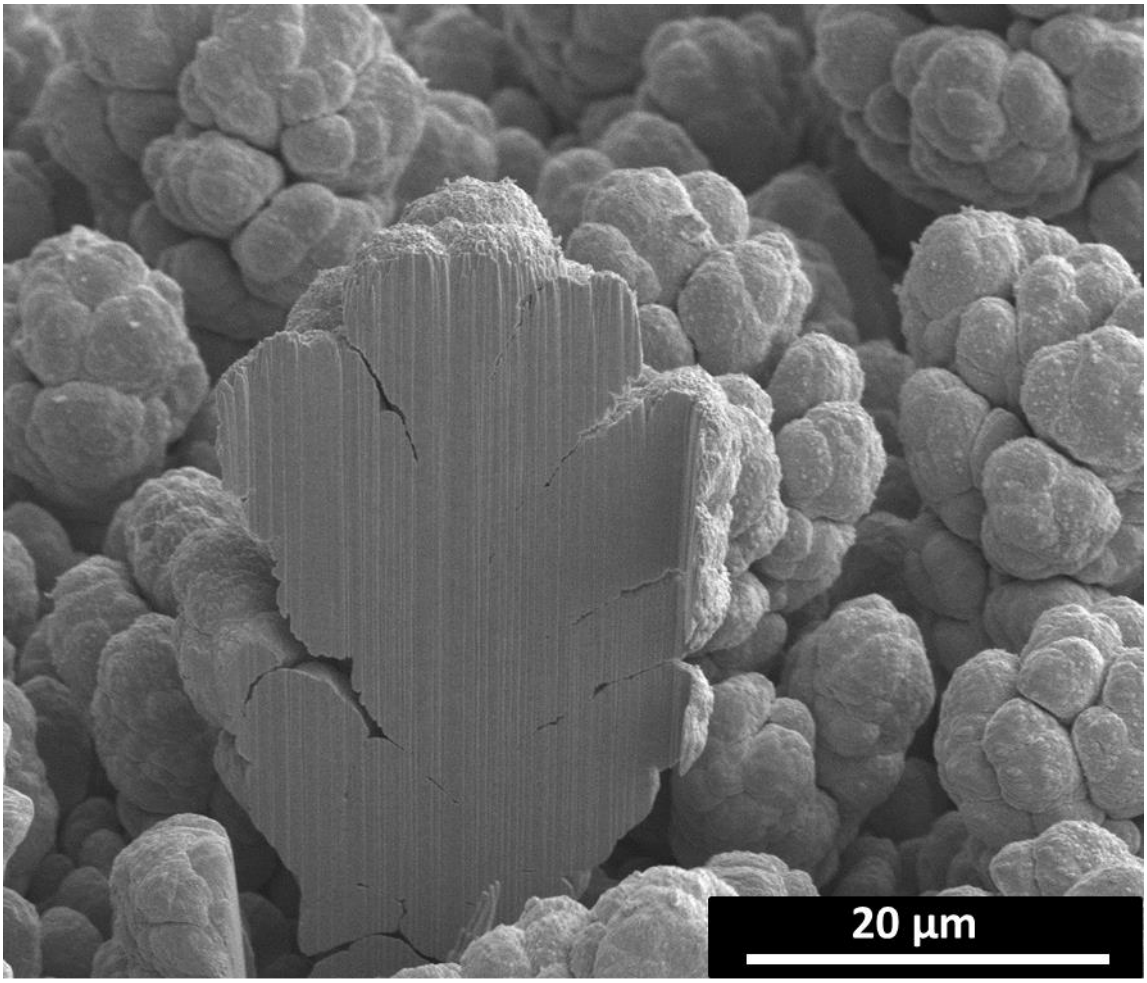

Figure 39: Micrograph of the two-layer deposit. The cross section of one of the florets is revealed through a cut made by ion beam.

Figure 40 shows six successive snapshots obtained from the full rebound of a 4.5 µL droplet on the two-layer deposit obtained by applying an overpotential of 1.1 V for the formation of the first layer of coating followed by applying the second layer of copper at an overpotential of 0.15 V for 10 s, . This bouncing sequence is similar to what has been reported for the dynamic behavior of a drop on a superhydrophobic surface in the literature[21]. The snapshot at t = 0 ms show the water droplet at the initial condition as it is about to hit the surface and the snapshot at t = 5.3 ms shows

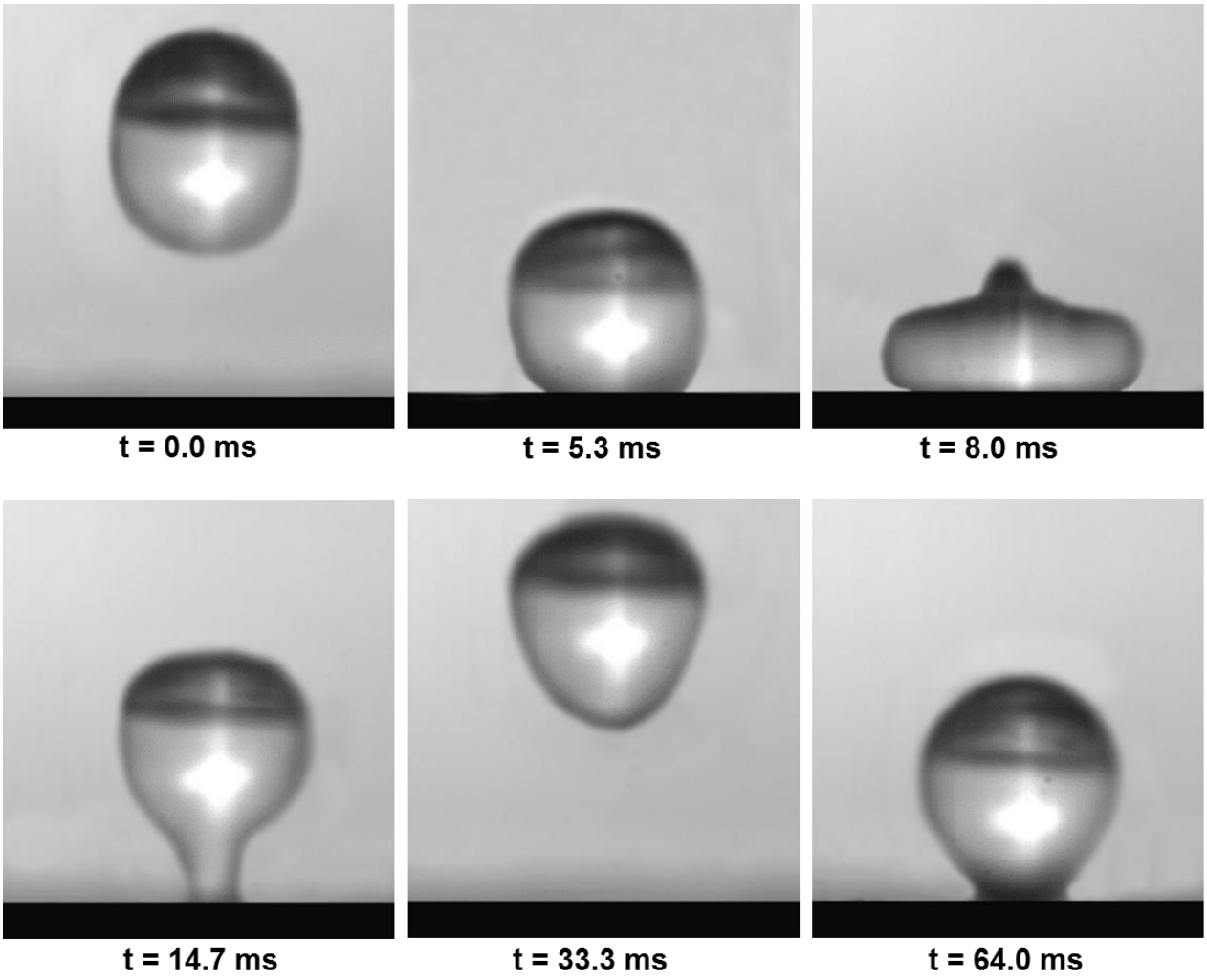

Figure 40: Successive snapshots obtained from the full rebound of a 4.5 µL droplet on the coating made by the two-step electrodeposition technique.

the image of the water droplet when it impinges on the surface and starts to deform. The droplet is completely deformed as seen in Figure 38 at t = 8.0 ms. For impingement on the superhydrophobic surface, the kinetic energy of the droplet is restored into the surface energy, which allows the droplet to bounce off the surface as observed at t = 33.3 ms and impinges on the surface again at t = 64 ms.

In addition to the quantitative and qualitative observations on the wetting characteristics presented in Figure 37 – Figure 40 above, it is also instructive to examine the surface chemical composition in order to show that the fabrication technique does not change the chemistry of the

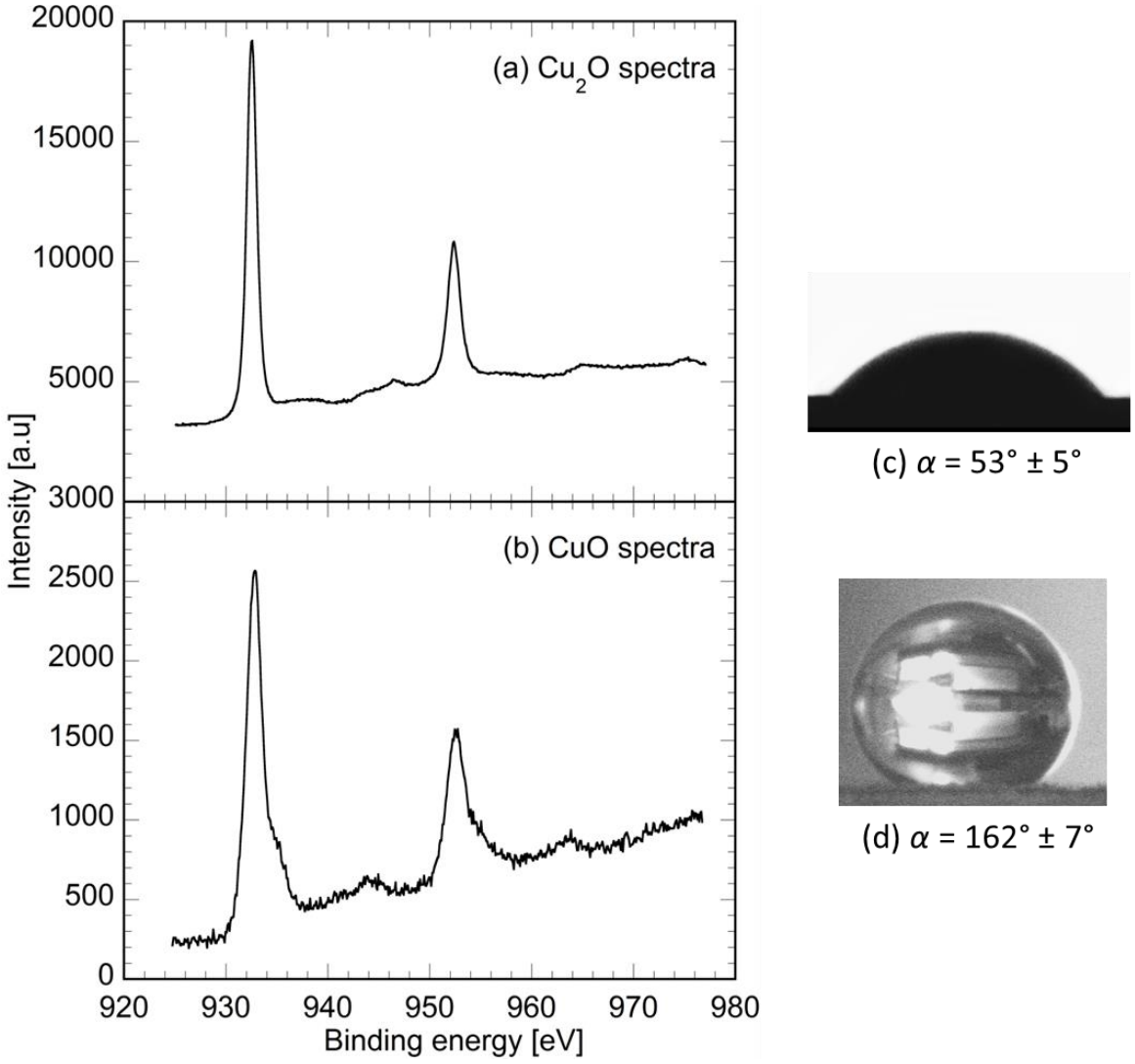

Figure 41: (a) XPS spectrum of the copper-colored made by applying 1.1 V overpotential (b) XPS spectrum of the copper-colored made by applying 1.3 V overpotential. The representative drop shape and the corresponding contact angle obtained on the black coating (c) just after its fabrication (d) after four weeks. The variation represents a standard deviation of ±1.

copper surface. At the ambient condition copper always appears in one of the two oxidation states: Cu_2O is the most common state that is associated with the copper color. Further oxidation of copper produces CuO, which is easily distinguished from Cu_2O because of its black color. One- and two-layer Deposits shown in Figure 37a-f and Figure 39 have the copper color associated with the Cu_2O oxidation state. Formation of a black CuO deposit was observed when overpotentials higher than 1.1 V were applied. In order to determine the chemical state of the copper- and black-colored deposits, XPS analysis has been carried out on two coatings made by applying 1.1 V and 1.3 V overpotentials and the spectra are shown in Figure 41a and Figure 41b, respectively. The spectrum of the black deposit in Figure 41b shows high intensity shake-up satellites after the peaks. Moreover, these peaks are broader than the ones displayed in Fig. 6a for the copper-colored Cu_2O deposit. Based on the literature, the peaks in Figure 41b are the main characteristics of the CuO spectrum which make it distinct from the spectrum of Cu_2O[112]. The electron micrograph of the black deposit is similar to that shown in Figure 37f for copper-colored Cu_2O deposit obtained by applying an overpotential of 1.1 V, and is not depicted here. Furthermore, the representative drop shape, the average contact angle, and its standard deviation obtained on three different black coatings just after their fabrication have been displayed in Figure 41c. As this figure shows as-deposited black coating shows complete-wetting characteristic, with an average contact angle of 53°, despite its multiscale roughness. After four weeks, the wetting property of this deposit was found to change to being superhydrophobic and the average contact angle of 162° was measured on the three samples, as shown in Figure 41d.

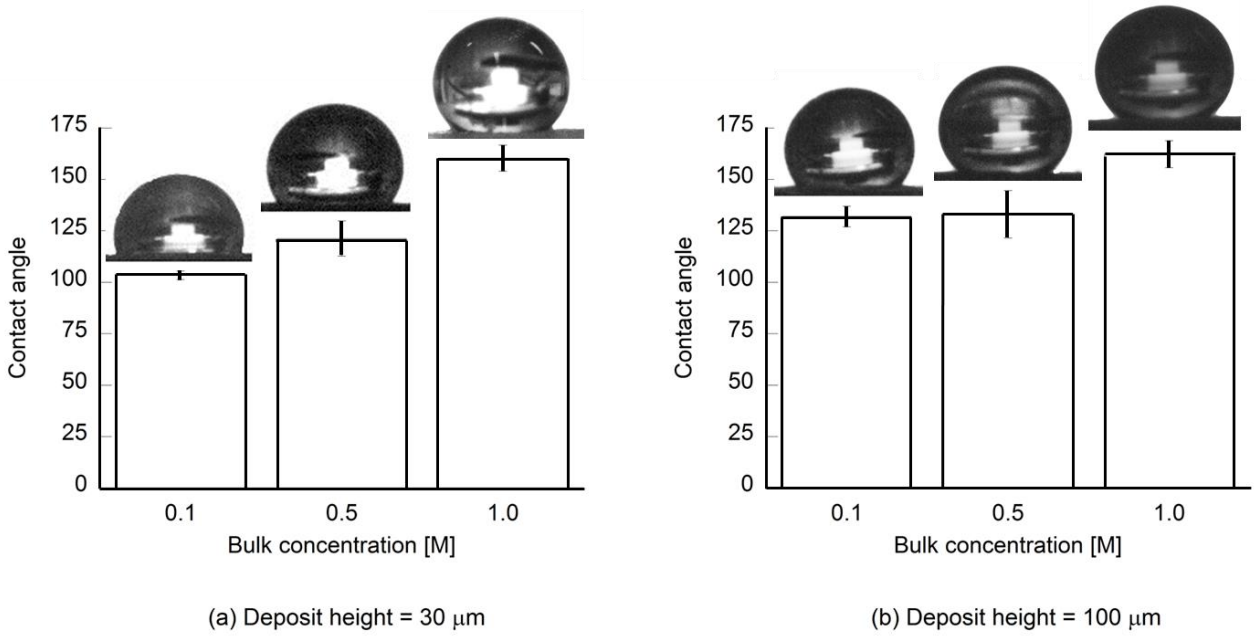

Figure 42: Effect of the $CuSO_4$ concentration in the electrolyte on the contact angle of two-layer deposits with (a) 30 μm and (b) 100 μm thickness made by applying 1.1 V overpotential. The concentration of H_2SO_4 was kept constant in 0.5 M for all three electrolytes. The error bar represents a standard deviation of ±1.

The shift from a complete wetting characteristic to superhydrophobicity after several weeks at the ambient condition is in agreement with studies reported in the literature for the textured CuO surfaces[113]. The change of the wetting characteristic of the black CuO deposit may be attributed to the explanation by Pei et al[99], who reported a reversible superhydrophobicity to superhydrophilicity transition of textured CuO surfaces by alternation of ultraviolet (UV) irradiation and dark storage. In their work, this transition was attributed to the water and oxygen adsorption on the defective sites made on the surface by UV irradiation. During electrodeposition, as in UV radiation exposure, defects are formed on the deposit surface. While water adsorption on the surface defects is kinetically favorable, thermodynamically, the defective sites are more prone

to adsorb oxygen. Initially, adsorption is mainly governed by the kinetic effect, as a result of which, most of the defective sites are occupied by the hydroxyl group. Hydroxyl adsorption results in the superhydrophilic characteristic of the as-deposited black coating. Adsorption of the hydroxyl groups gradually shifts the surface to a thermodynamically unstable condition and provides the driving force for the oxygen adsorption. Therefore, the hydroxyl groups are replaced gradually by oxygen atoms. After several weeks, the defective sites are mainly occupied by oxygen and the surface shows superhydrophobic characteristic.

In addition to the effect of overpotential which has been discussed so far, superhydrophobic characteristic of the deposit also depends on the bath concentration and deposit thickness. The effect of the bath concentration and deposit thickness on the contact angle of a two-layer deposit was studied by depositing copper coatings with 30 µm and 100 µm thickness at the overpotential of 1.1 V from the electrolytes with 0.1 M, 0.5 M, and 1 M $CuSO_4$ concentration. The concentration of H_2SO_4 was kept constant in 0.5 M for all three electrolytes. At each bath concentration and deposit thickness, contact angle of a 4.5 µL droplet was measured on two different samples and on each sample, the measurements were repeated three times. The median values of the contact angles and the representative shapes of the droplet on the deposits made from the electrolytes with different bulk concentrations are shown in Figure 42a–b for the deposit heights of 30 µm and 100 µm, respectively. As these figures display, average contact angle increases from 103° to 160° and from 132° to 162° for the deposit heights of 30 µm and 100 µm, respectively, when $CuSO_4$ concentration in the electrolyte increases from 0.1 M to 1 M. As explained in the "Theoretical Basis" section of this paper, at higher electrolyte concentrations, deposition process is more unstable, therefore more asperities are formed on the deposit surface and the hydrophobic characteristic of the surface is enhanced.

As shown in Figure 42a and Figure 42b, increasing electrolyte concentration from 0.1 M to 0.5 M results in 17 % enhancement in the contact angle of the 30 μm deposit and negligible change in the contact angle of the 100 μm deposit, respectively. In addition, if the bath concentration changes from 0.5 M to 1 M more increase in the deposit contact angle is obtained at the deposit height of 30 μm compared to the deposit height of 100 μm. Consequently, the effect of the electrolyte concentration on the contact angle is more evident at smaller deposit heights. Furthermore, the contact angle of 100 μm deposit is higher than the 30 μm deposit at all electrolyte concentrations shown in Figure 42a–b. These effects of the deposit height on the contact angle may be explained by the effect of the growth time on the surface asperities of the growing phase in an unstable growth process. During electrodeposition, like other unstable growth processes, protrusions develop with time and the surface roughness is higher at larger deposit heights[19]. Therefore, when deposition continues for a longer time and thicker deposit is formed, the effect of the electrolyte concentration on the deposit contact angle is diminished and larger contact angle is observed.

In addition to the static contact angles (Figure 42a–b) and the full rebound of the droplet on the surface (Figure 40), contact angle hysteresis may be determined to further show the superhydrophobic characteristic of the two-layer deposit[74]. To determine the contact angle hysteresis, a 4.5 μL droplet was formed with a syringe and brought in slight contact with the surface. Then water droplet, attached to the syringe, was slowly moved along the sample surface and the contact angle hysteresis was deduced from the advancing and receding contact angles which were measured at the front and back of the moving droplet, respectively. This measurement was repeated five times for a two-layer deposit with 30 μm thickness which was made by applying 1.1 V overpotential in a bath with 1 M $CuSO_4$ concentration (Figure 39). The representative shape

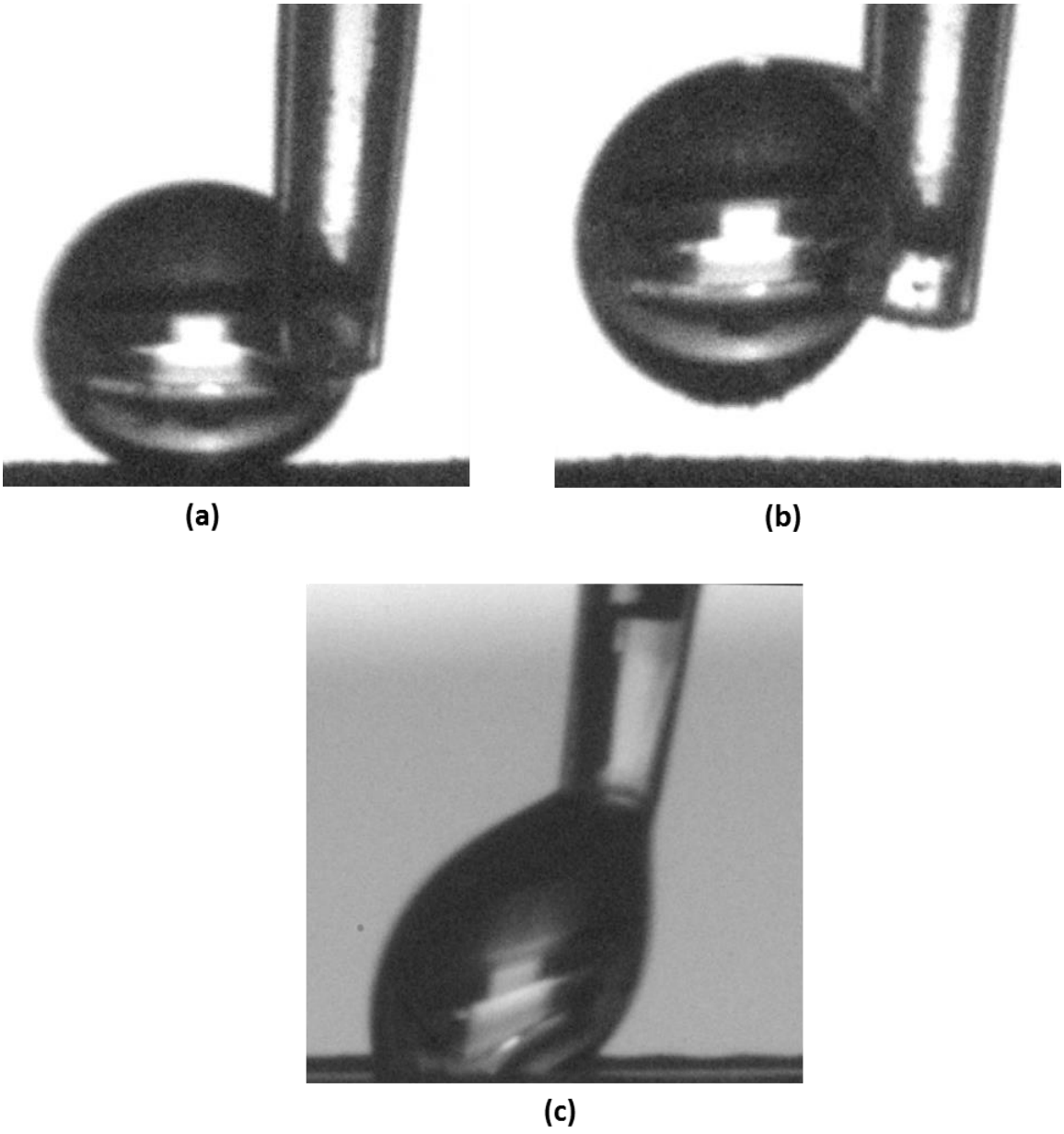

Figure 43: Water droplet attached to the syringe, was slowly moved along the two-layer deposit made from the electrolyte with (a) 1 M $CuSO_4$ concentration and (c) 0.5 M $CuSO_4$ concentration by applying 1.1 V overpotential. The contact angle hysteresis can be deduced from the advancing and receding contact angles which were measured at the front and back of the moving droplet, respectively. Droplet can be separated easily from the superhydrophobic surface made from the electrolyte with 1 M $CuSO_4$ concentration as shown in (b).

of the droplet which is moved on this surface by the syringe is shown in Figure 43a. On this surface, the median value of the contact angle hysteresis and the standard deviation of 5° and 2° were obtained, respectively. On this two-layer deposit, droplet can be moved freely and it can be separated from the surface easily as shown in Figure 43b. The similar behavior is observed when the droplet is moved faster on the surface. As presented in the video provided in the supporting material, water droplet does not adhere to the surface even if it is pushed onto the surface; furthermore it moves freely along the surface even at a high velocity. In contrast, a water droplet adheres to a non-superhydrophobic surface after the first contact and cannot be separated. Figure 43c shows an example of this behavior of the droplet on a two-layer deposit made from an electrolyte of 0.5 M $CuSO_4$. As this figure presents, when the syringe is moved, the droplet is not separated from the surface; instead it is elongated and a large difference between the advancing and receding contact angles is observed.

Experimental results presented so far suggest that the morphological instabilities formed during electrodeposition can result in the superhydrophobic characteristic of the deposit surface. In the next section, a theoretical explanation for the development of these morphological instabilities is presented and from that the effect of the bath concentration and overpotential on the unstable growth process during electrodeposition is deduced.

5.4 Theoretical Basis

The morphological instabilities, developed during the growth process, are known as the main reason for the superhydrophobic characteristic of the copper coatings deposited from a concentrated bath by applying a high overpotential. The effect of the bath concentration and

overpotential on developing morphological instabilities during electrodeposition may be explained based on the theoretical descriptions of the mass transport process in the electrolyte and growth kinetics on the deposit surface. These descriptions are mainly inspired from the literature in the well-studied area of unstable growth during thermal solidification[27]. When the interface between the growing phase and the parent phase is unstable, arbitrary perturbations on the growing phase get larger and multiscale surface features are formed. Beyond a certain level of instability, branches which become detached from the parent phase can grow independently and equiaxed growth occurs. The growth stability and shape of the surface features in thermal solidification are controlled by the combined effect of several parameters such as transfer of heat/mass, kinetic of atom attachment to the interface, capillarity, and solute pile-up. In this section, effects of the kinetic and mass transfer parameters on the growth stability during electrodeposition from an aqueous electrolyte are examined and compared to those reported in the literature for thermal solidification.

In general, instability occurs if the chemical potential of the solidifying species in the liquid, μ, increases with distance from the interface of the growing phase[17]. Therefore, the condition for unstable growth in the *y* direction at the growing interface ($y = 0$) is defined as follows:

$$\left(\frac{\partial \mu}{\partial y}\right)_{y=0} > 0 \qquad (54)$$

Since the chemical potential of an ion in an aqueous solution is a function of temperature, *T*, and ion activity, *a*, the partial derivative of the chemical potential with respect to *y* in Eq. (54) may be expressed as follows:

$$\frac{\partial \mu}{\partial y} = \left(\frac{\partial \mu}{\partial a}\right)_T \left(\frac{\partial a}{\partial y}\right) + \left(\frac{\partial \mu}{\partial T}\right)_a \left(\frac{\partial T}{\partial y}\right) \qquad (55)$$

During electrodeposition, temperature remains constant; therefore the second term on the right hand side of Eq. (55) is zero. Obtaining the partial derivative of the chemical potential with respect to activity from $\mu_{cu^{2+}} = \mu^0 + RT\ln(a_{cu^{2+}})$ and substituting that into Eq. (55) results in the following equation:

$$\left(\frac{\partial \mu}{\partial y}\right)_{y=0} = \left[\frac{RT}{a}\left(\frac{\partial a}{\partial y}\right)\right]_{y=0} \tag{56}$$

The activity gradient is directly related to the concentration gradient. In electrodeposition, the concentration gradient of the metal ion with respect to the growth direction at the deposit interface is always positive. Therefore, Eq. (56) shows that the partial derivative of the chemical potential with respect to *y* is positive at the deposit interface and the condition for the unstable growth, Eq. (54), is always satisfied. In this regard, electrodeposition is similar to the thermal solidification of alloys, in which the dendritic surface features are always developed due to the unstable growth mechanism. The increase of the surface roughness with deposit height during electrodeposition, which has been previously reported in the literature[19], is the result of this unstable growth mechanism.

In addition to the trend of the chemical potential, unstable growth during electrodeposition can be explained by the mass transfer process in the electrolyte. In a quiescent electrolyte, besides electric migration, a significant portion of the mass transfer always occurs by diffusion. Local diffusive flux to different positions of the surface mainly depends on the geometry of those positions[37, 38]. Protrusions are more accessible to the electrolyte; therefore, they collect additional diffusive flux from the electrolyte and grow faster compared to the flat parts of the deposit surface.

Though electrodeposition from an aqueous electrolyte is always considered as an unstable growth process, the experimental observation presented in this work shows that morphological

instabilities are higher when larger overpotentials are applied (Figure 37a–l) or when deposition occurs from a more concentrated bath (Figure 42a–b). This effect of the overpotential and electrolyte concentration on the morphological instabilities can be explained by Eq. (56) using the effects of these parameters on the concentration gradient of the depositing species on the deposit surface. The governing equations for the combined migration-diffusion transfer in an electrolyte can be solved analytically only if all ions present have the same magnitude of charge (homovalent electrolyte) [48]. Though electrolyte of $CuSO_4$ and H_2SO_4 is not homovalent but the solution for a homovalent electrolyte can provide schematics which explain the effects of the overpotential and electrolyte concentration on the concentration profile of the depositing ion, as shown in Figure 44a–b. At high enough overpotentials, the system reaches its mass transfer limitation and the ion concentration on the deposit surface approaches zero. This concentration gradually increases in the bath and reaches the bulk concentration, c_∞, at locations far from the deposit surface. At larger overpotential, concentration gradient at the deposit surface is higher (Figure 44a) and as a result, greater derivative of the chemical potential is obtained from Eq. (56). Therefore, more instability is expected for the deposit made by applying higher overpotentials. Similarly, at larger bulk concentration, a steeper change of the ion concentration at the deposit surface is observed (Figure 44b) and the growth is more unstable.

The similarities between electrodeposition and thermal solidification can also be used to explain the effect of the overpotential on the shape of the surface features shown in Figure 37a–f. In the solidification literature, it has been reported that the unstable growth process may result in the formation of either faceted or non-faceted surface features[27]. The non-faceted surface features are recognized by their dendritic trunks, while faceted structures have smooth, planar surfaces (facets). In the faceted mode of growth, the process is mainly controlled by the kinetics of

atom transfer from the liquid to the solid interface and the growth rate depends on the crystal plane orientations. Consequently, the structure remains bounded by the slower growing orientations and facets form. On the contrary, when a substrate exhibits the non-faceted growth mode, the kinetics of transfer of atoms from the liquid to the solid interface are so rapid that atoms can be easily added to any point of the surface. As a result, crystal plane orientations have negligible effect on the growth rate. The aforementioned explanation for the kinetic effect in thermal solidification may be used to describe the effect of the overpotential on the shape of the surface features formed by electrodeposition. At low overpotentials, the deposition process is mainly controlled by the kinetics of the electron-transfer reaction; consequently, faceted surface features, such as those shown in Figure 37a for η = 0.1 V, are formed. In contrast, at high overpotentials kinetic effect is negligible and deposition is mainly controlled by the diffusion process. As a result, non-faceted surface features, such as the fractal-shaped structures shown in Figure 37f for η = 1.1 V, are developed.

In this section, formation of the morphological instabilities during electrodeposition was theoretically explained using the theories of the unstable growth during thermal solidification. This theoretical explanation provides the foundation for using the fabrication technique, presented in this work, in other electrodeposition systems besides copper. Using this fabrication technique for making superhydrophobic coatings from materials other than copper will be considered in a future study.

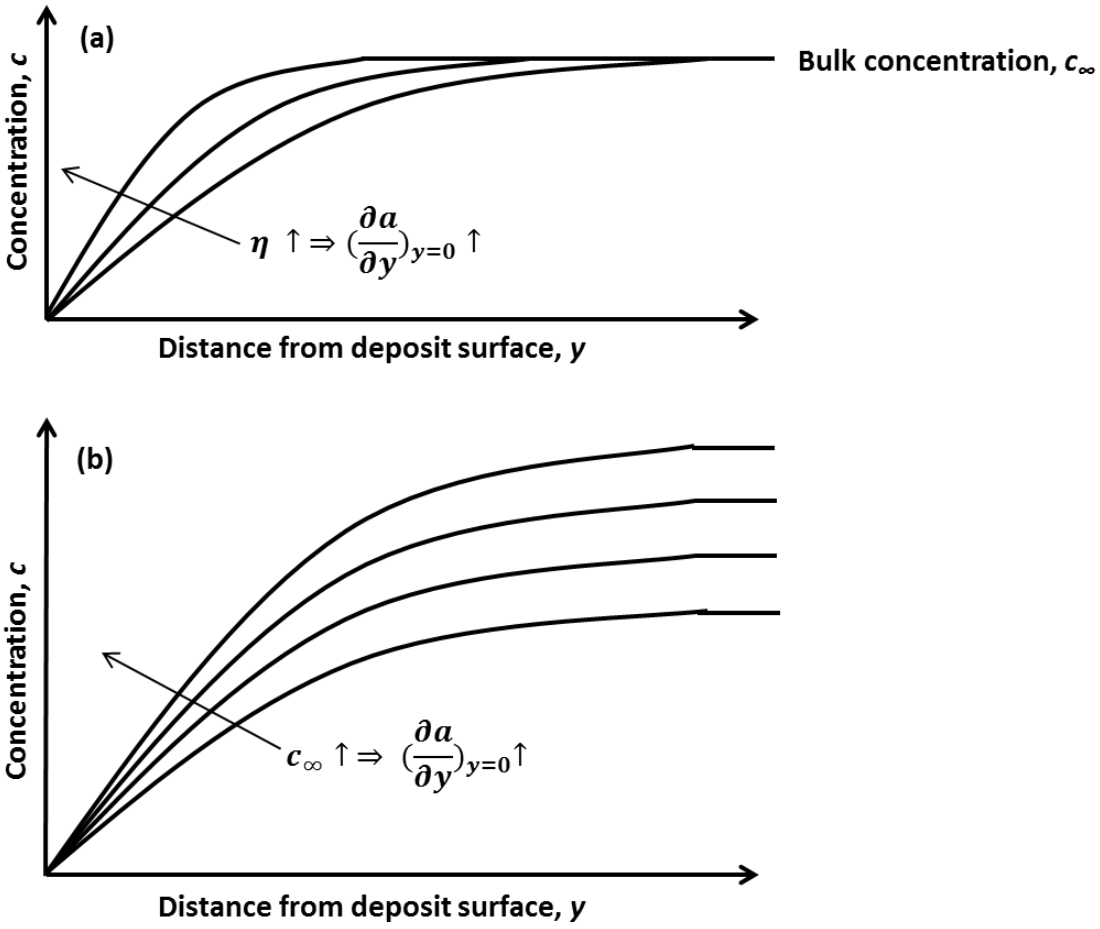

Figure 44: Effects of (a) overpotential and (b) bulk concentration of the electrolyte on the concentration profile of the depositing ion in the electrolyte.

Chapter 6: Effects of the Electrochemical Parameters on the Internal Structure of the Electrodeposited Microparts

6.1 Introduction

Properties of an electrodeposited metal are usually completely different from the data reported for the pure metallurgical samples. This difference is considered as the result of developing special crystalline structure during electrodeposition. In addition to the high level of impurities and defects, size and shape of the crystalline grains are also different in the metal made by electrodeposition compared to other techniques [28]. In particular, metals with small crystalline grains can be obtained by applying appropriate process variables during electrodeposition. For instance, electrodeposition is known as a cost-effective and non-equipment-sensitive method for the preparation of nanocrystalline metals, with grain size less than 100 nm [114]. In addition to nanocrystalline metals, electrodeposition is used to make superplastic metals with the grain size less than 10 μm. Superplastic metals have different applications due to their capability to undergo extensive, neck-free, tensile deformation prior to fracture [115].

The microstructure of an electrodeposited metal is mainly determined by the characteristic of the nucleation and growth process. For electrodeposition on a foreign substrate, the nucleation and growth process consists of two stages. In the initial stage, which covers deposit thickness up to several microns, the substrate influences deposit morphology. After this stage, nucleation and growth process is manly controlled by the process variables and is completely independent of the substrate structure [28]. At the second stage of the nucleation and growth process, grain refinement may be obtained by altering different process parameters such as current density, pulse duration,

and overpotential [116]. Different techniques for making fine-grained metals using electrodeposition were presented in the literature [28, 116, 117] but a general basis which can be utilized to predict the grain size has not been provided so far.

This work presents an experimental investigation for the effects of overpotential and current density on the morphology and surface structure of the copper deposited from a copper sulfate bath. In electrodeposition, overpotential provides the driving force for the nucleation and growth process. Therefore, overpotential may intuitively appear as a better parameter for controlling deposit morphology compared to the current density. Unlike this intuition, in this work, it is shown that current density can be utilized to predict the grain size in the whole process range while overpotential cannot be related to the grain size when special process conditions are applied. This is because, unlike overpotential, current density is bounded by a maximum value called limiting current density which corresponds to the mass transfer limitation of the system. The experimental results presented in this work for the electrodeposited coating show that after reaching the limiting condition, both grain size and current density remains constant with increasing overpotential. Therefore, overpotential does not provide a good prediction for the grain size at the limiting condition. In addition to the deficiency of the overpotential to predict the grain size at the limiting condition, in this work it was shown that the morphology of the deposit which is grown through a microtrench is completely different from that of the electrodeposited coating on a flat surface made by applying the same overpotential. Similar to the deposit morphology, different current densities are obtained for the electrodeposition through a microtrench and on a flat surface when the same overpotential is applied. Consequently, the change of the grain size with the electrode position in the bath can be more appropriately related to the current density than the overpotential. Unlike grain size, surface characteristics of the deposit such as roughness and surface texture change by

increasing overpotential at the limiting condition. Therefore, current density cannot be used to predict deposit surface structure at the limiting condition.

In addition to the effect of the overpotential and current density on the grain size and surface structure of the deposit, the work also presents a theoretical explanation for the effect of the overpotential on the formation of material defects other than the grain boundaries, such as dislocations. The article is organized as follows: A description of the experimental study is discussed in the next section, followed by a presentation and discussion of the results of the study.

6.2 Experimental Methods

Reagents. Though presence of impurities containing sulfur and hydrogen in the structure of copper deposit which is formed in a copper sulfate bath is inevitable, using analytical grade chemicals is important for accurate experimental results [41, 42]. Impurities other than the electrolyte species adversely influence the reproducibility of the experiment because they have uncontrolled effects on the mass transfer process in the bath and on the surface characteristic of the electrode [43]. Therefore, in this work analytical grade $CuSO_4$ and H_2SO_4 supplied by Fisher Chemicals (Pittsburgh, PA, USA) were used. In addition, deionized water with resistivity of 18 MΩ.cm (Millipore Corp., Billerica, MA, USA) was utilized for making all solutions.

Fabrication process. In this work, electrodeposition was utilized to make coatings with 30 µm thickness and to fabricate standalone microstructures with height, width, and length of 100 µm, 100 µm and 1.5 cm. Herein, electrodeposited films are called one-dimensional microparts while standalone microstructures are referred to as two-dimensional microparts. Both one and two

dimensional microparts were deposited on silicon substrates covered by a smooth copper film using physical vapor deposition (PVD). For making two-dimensional microparts, electrodeposition occurs through micromolds which are made on a layer of KMPR photoresist spread over the silicone substrate. In contrast, flat silicon substrate with the area of 0.7×0.6 cm^2 was used to fabricate one dimensional microparts. For making both these microparts, electrodeposition was performed using an AUTOLAB PGSTAT128N potentiostat (ECO Chemie, Utrecht, The Netherlands). A traditional three-electrode system was employed in which a copper sheet and a platinum mesh were utilized as the reference electrode and anode, respectively. Furthermore, an electrolyte of $CuSO_4$ 1 M and H_2SO_4 0.5 M was used in all fabrication techniques. To remove oxygen from the electrolyte, it was bubbled for 15 minutes before fabricating each sample. Moreover, the electrolyte was replaced by a new solution after fabricating each sample to avoid contamination. Since the reference electrode was composed of the same material as the deposit, herein, the term overpotential is used to refer to the electric voltage. A constant negative overpotential was applied to deposit copper on the substrate. However, in this paper, the overpotential, is referred to by its absolute value, η. Coatings were fabricated by applying different overpotentials in the range of 0.1 V to 1.1 V and two dimensional microparts were made using overpotentials of 0.1 V and 0.2 V.

Characterization. The surface morphologies and the roughness of the one dimensional microparts were examined using the FEI Quanta 600 scanning electron microscope (SEM) and NewView 7100 surface profiler, respectively. In addition, FEI Helios 600 NanoLab was used to get ion induced secondary electron images of the deposit cross section.

6.3 Results and Discussion

Figure 45 shows the time-variation of current during deposition of one-dimensional microparts with 30 μm thickness, when constant overpotentials in the range of 0.3 V to 1.1 V, in increments of 0.2 V, are applied. In general, current varies with time during the deposition process because of (1) changes in the electrolyte concentration on the electrode surface and (2) changes in the active electrode area. The sharp decrease at small times in the current curves shown in Figure 45 corresponds to the initial decrease in Cu^{2+} surface concentration from the bulk concentration, c_0, to the steady-state concentration. After this initial decrease, the flat deposit surface gradually evolves

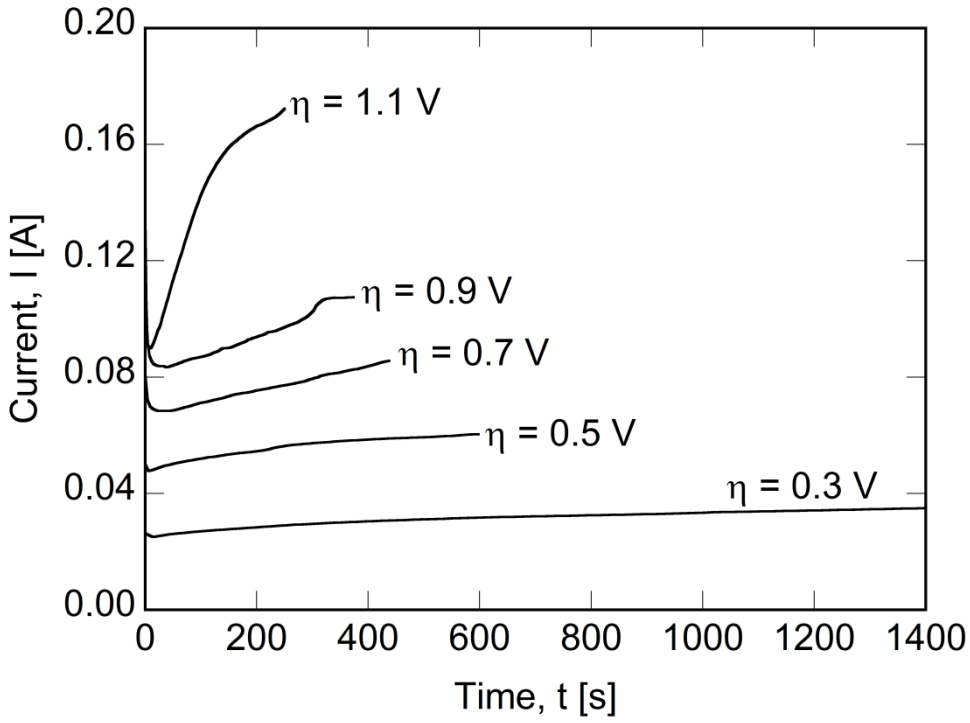

Figure 45: Time-variation of current during deposition of one-dimensional microparts with 30 μm thickness, when constant overpotentials in the range of 0.3 V to 1.1 V, in increments of 0.2 V, are applied.

to a volcano structure due to edge effects [37, 38], resulting in a gradual increase of the active area and consequently, a slight increase in the current trend. Therefore, at the local minimum of the current trend, shown in Figure 45, the surface concentration approaches that of the steady state. In addition, at this point, an almost flat deposition front is formed whose surface area is very close to the initial substrate area (A = 0.42 cm^2). Considering this explanation, the current values at the local minimum points, I_∞, may be used in the following equation to obtain the steady-state current densities, i_∞, at different overpotentials:

$$i_\infty = \frac{I_\infty}{A} \tag{57}$$

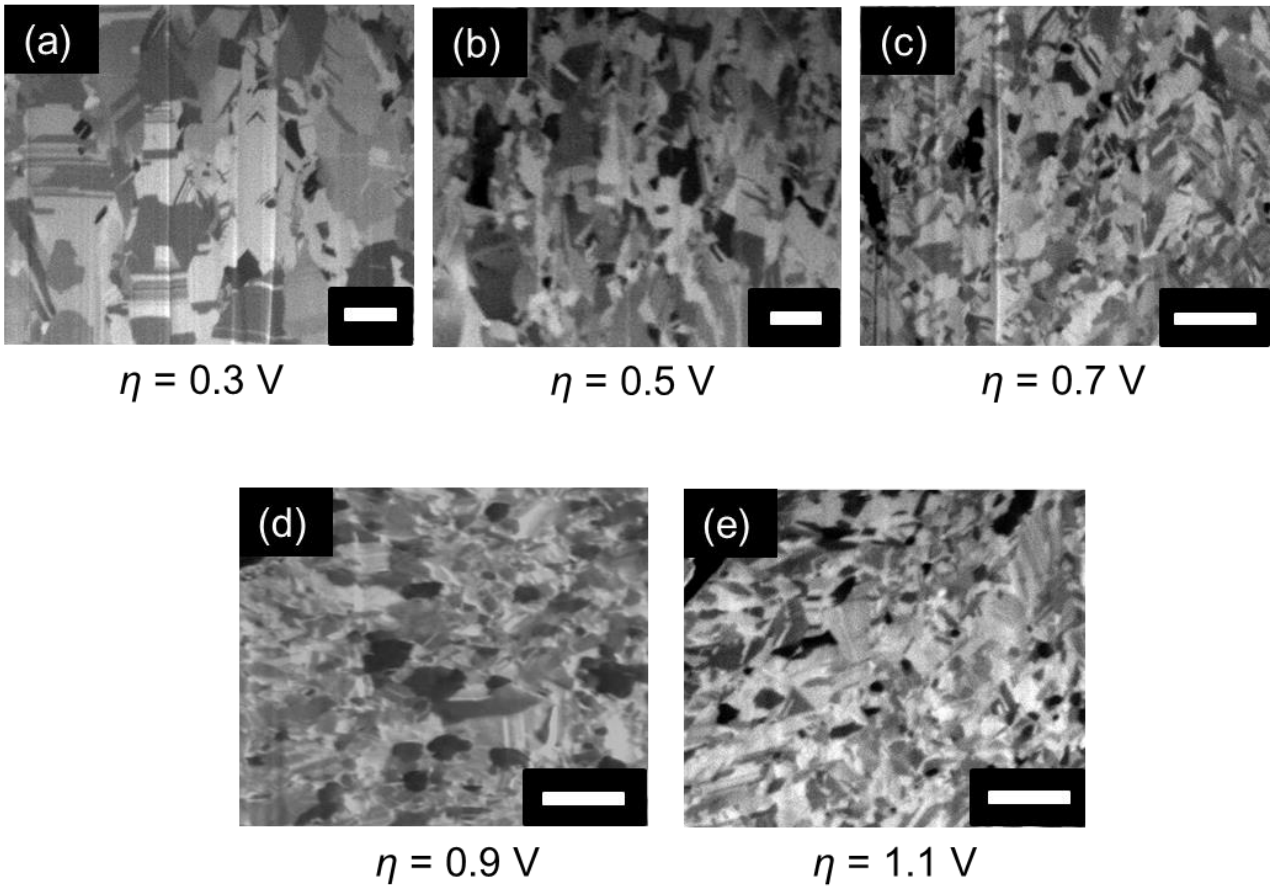

Figure 46: Internal structure of one-dimensional microparts made by applying constant overpotentials in the range of 0.3 V to 1.1 V, in increments of 0.2 V.

Two samples were fabricated at each of the overpotentials shown in Figure 45. The cross section of each sample was revealed through two cuts made by focused ion beam at the center of each sample, then the internal structure of the microparts were obtained using ion induced secondary electron images of the cuts. Figure 46a–e show the representatives of the ion induced secondary electron images for the microparts made by applying overpotentials in the range of 0.3 V to 1.1 V, in increments of 0.2 V. In these images, the grains are seen as regions with uniform contrast, different from the neighboring areas and characterized by well-defined edges. Note that in this work, the grains are defined as the largest sized microstructural features revealed in Figure 46a–e. Intercept method was used to obtain the average size of the grains for each of the ion induced secondary electron images and the results were shown in Figure 47 as the variation of mean grain diameter with overpotential.

Figure 47a indicates that the average grain size reduces sharply by increasing overpotential in the range of 0.3 V to 0.7 V, while increasing overpotential to the values more than 0.7 V does not have a notable effect on the grain size. Points beyond overpotential of 0.7 V are located in the limiting region which corresponds to the mass transfer limitation of the system. In this region, the concentration of the metal ion on the deposit surface falls to zero and the distribution of the local current density or the local deposition rate is mainly controlled by mass transfer process in the electrolyte. Similar to the grain size, current density remains constant with increasing overpotential in the limiting region. Consequently, current density is more appropriate parameter to explain grain size in the whole operating range. Figure 47b shows variation of the surface roughness of one-dimensional microparts obtained using light interferometery (Scan length is 650 μm) with overpotential. These figures reveal a strong enhancement of roughness with overpotential for the films fabricated using overpotentials more than 0.5 V, which can be explained using the models

presented in the literature for the unstable growth process [9-12]. These models show that mass transfer favors the growth of the arbitrary protrusions of the surface and enhances the morphological instabilities of the deposit. At higher overpotentials, mass transfer has more controlling effect on the deposition process and consequently, the growth is more unstable. On the contrary, the decrease in the surface roughness with overpotential for the films fabricated using overpotentials less than 0.5 V, which has been indicated in Figure 47b, can be attributed to the decrease in the average grain size in this region [2]. Figure 47b shows that though at low overpotentials internal and external structures are directly related at higher overpotentials, when the growth instability enhances, this direct relationship is not satisfied. In addition, since after reaching the limiting condition, the current density remains constant with increasing overpotential, the change of the deposit surface structure at the limiting condition is more appropriately attributed to the change in the overpotential.

Figure 48a and Figure 48b show the internal structures of the two-dimensional microparts made by applying 0.2 V and 0.1 V overpotentials, respectively. These figures were obtained from the cross sections of the microparts at their central parts. Similar to the one dimensional microparts shown in Figure 46a–e, internal structure of the two-dimensional micropart fabricated at higher overpotential (Figure 46a) reveals smaller grain size compared to the one made by applying lower overpotential (Figure 46b). In addition, internal structure of the two-dimensional micropart shown in Figure 46b may be compared with that of the one-dimensional micropart made by applying the same overpotential ($\eta = 0.1$ V) in Figure 46c. This comparison shows that the grain size of deposit which is grown through a microtrench is larger than that of the electrodeposited coating on a flat surface made by applying the same overpotential. In general, Figure 46a–e and Figure 48a–b show

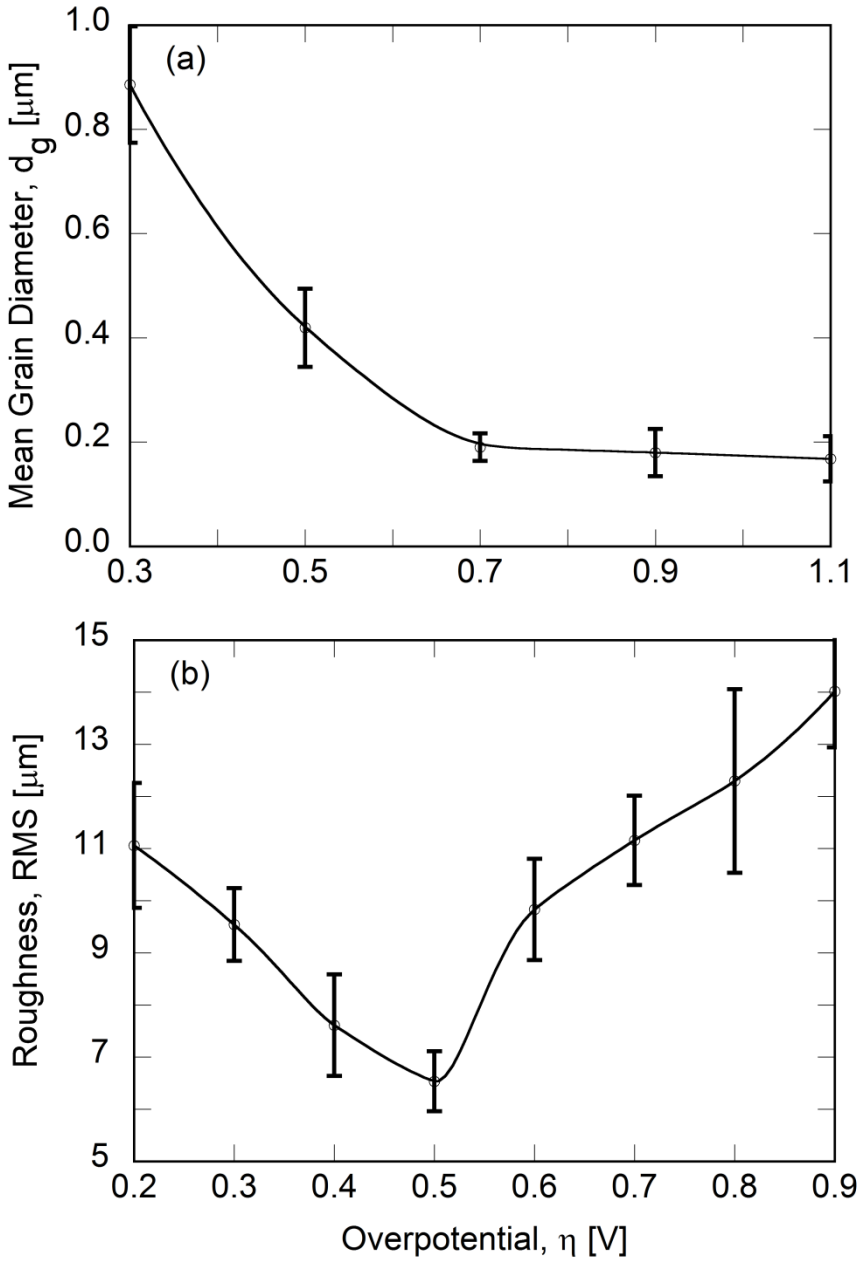

Figure 47: Variation of (a) mean grain diameter and (b) surface roughness of one-dimensional microparts with overpotential

grain size of an electrodeposited micropart is mainly controlled by the current density. Smaller grains are obtained at higher current densities.

In addition to the grain size the shape of the grains is also controlled by the current density. In this work, average shape factor, SF, defined by the following equation is used to present the grain shape:

$$SF = \frac{4\pi A_g}{{L_g}^2} \tag{58}$$

where A_g is the grain's surface area and L_g is its perimeter. The shape factor is equal to one for a circle and falls to zero for a straight line. Figure **49**a shows the cumulative distribution function (CDF) of the shape factor for the one-dimensional microparts shown in Figure **46**a–e, while Figure **49**b shows the same trend for the microparts shown in Figure **48**a–c. In general, at higher current densities, the shape of the grains is closer to a circular shape and therefore, larger shape factor is obtained.

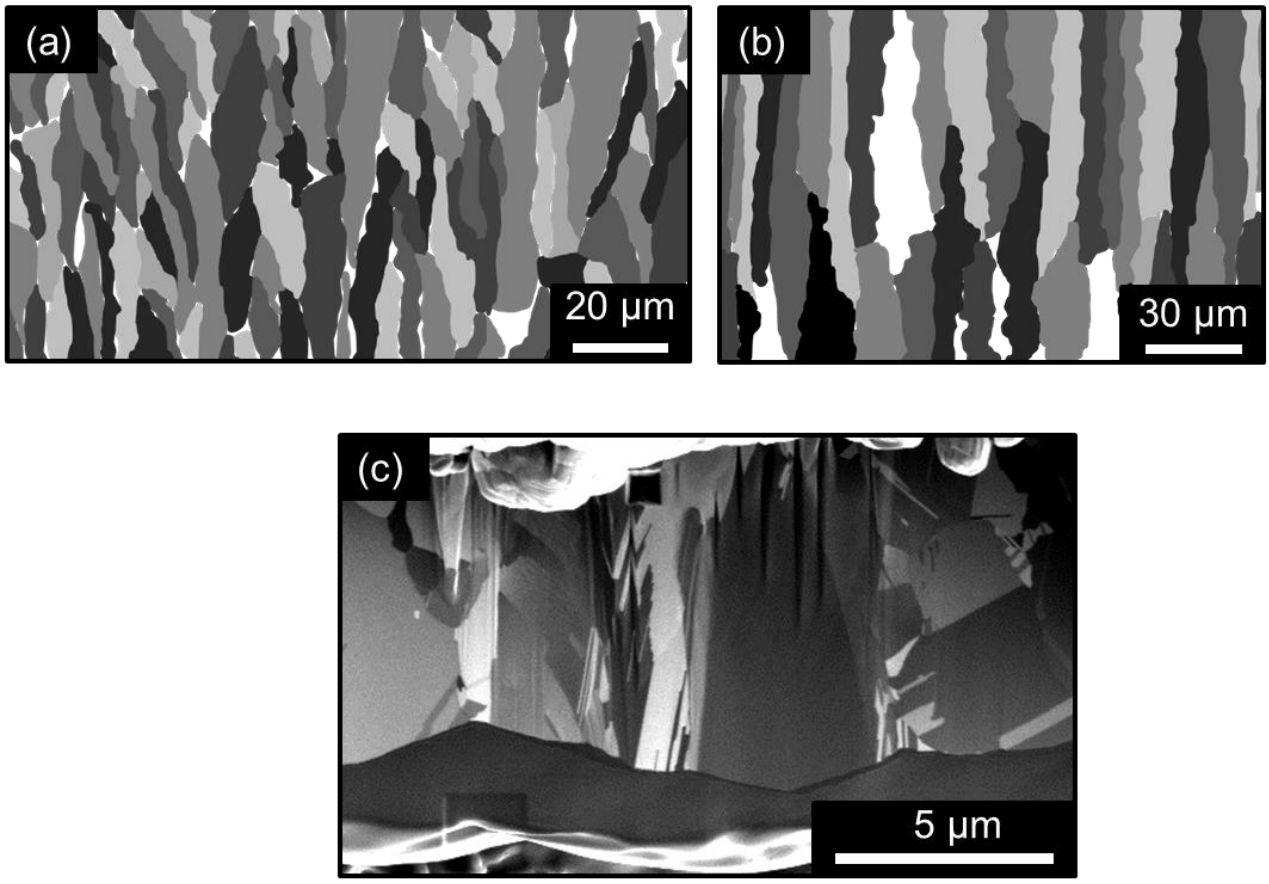

Figure 48: Internal structures of the two-dimensional microparts made by applying (a) 0.2 V and (b) 0.1 V overpotentials and (c) one-dimensional micropart fabricated by applying 0.1 V overpotential.

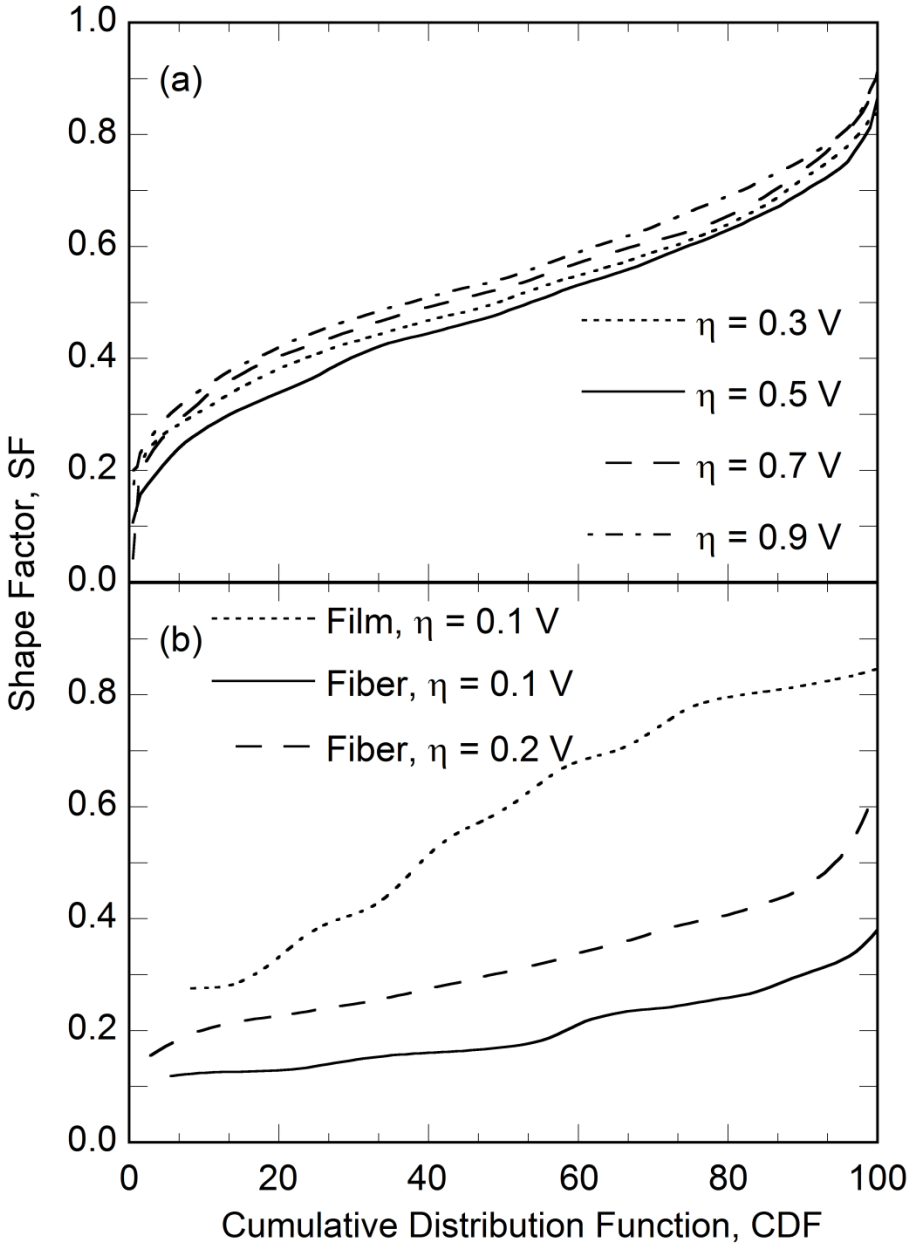

Figure 49: Cumulative distribution function (CDF) of the shape factor for (a) one-dimensional microparts shown in Figs. 2a–e and (b) microparts shown in Fig. 4a–c.

Chapter 7: Conclusion and Future Works

Electrodeposition is one of the main techniques for fabricating conductive parts with one or two dimensions in the micron size range. This technique is utilized to coat surfaces with protective films of several micrometers thickness or fabricate interconnects and standalone microstructures. In this work, electrodeposited films are called one-dimensional microparts while interconnects and standalone microstructures are referred as two-dimensional microparts. In electrodeposition, an electric voltage, called overpotential, provides a driving force for the crystallization process. Electrocrystallization results in the evolution of a deposition front from a conductive substrate which finally leads to the formation of a micropart. In electrodeposition, profile of the deposition front may deviate from the substrate shape. Consequently, different leveling conditions may obtain for a deposit evolved from a flat substrate. Moreover, the evolved surface will have a special texture in micro or nanoscale domain. Crystalline structure, surface texture and leveling condition are three important factors which define several properties of the microparts. These three factors are functions of several fabrication parameters such as overpotential, size of the substrate and its position in the bath. Dissertation work aims at improving the current understanding of the effects of the overpotential and geometrical parameters on the aforementioned factors. The contribution and significance of the study performed on each of these three parameters in this dissertation work has been discussed separately in the following three sections:

1. **Deposit Uniformity.** Electrodeposition in sacrificial polymeric micromolds is one of the main techniques for fabricating two-dimensional microparts. If electrodeposition mold is fabricated by UV lithography, the sidewalls and base of the mold are composed of an insulating polymer and a metal film, respectively. Deposit originates from the conductive base and grows

conforming to the micromold geometry. As deposit develops, deposition front is evolved in the form of a curved surface. Evolution of the curved interface requires a subsequent precision grinding process to level surface of the microparts. This work aims at removing the need for this subsequent process. To this end, multiphysics modeling has been used to simulate temporal evolution of deposition front in a micromold. The work presents a systematic study for the effects of the applied overpotential and micromold geometry on the leveling condition of the deposit. Consequently, a design strategy has been suggested to obtain a flat deposition front at the highest possible deposition rate. Unlike models presented previously in the literature, the model presented in this work covers the complete range of the relevant overpotentials. This model has been presented previously in a couple of literatures but it has been used for the first time for the detailed analysis of the effects of the fabrication parameters on the leveling condition of the deposit.

The second type of the electrodeposition molds are fabricated by plastic molding instead of UV lithography. The sidewalls and base of these molds are, respectively, composed of a thermoplastic and a microscreen with insulating holes. In the second part of this work, temporal evolution of deposition front in a microscreen-based micromold has been modeled. Effects of the applied overpotential and microscreen geometry (size and number of the insulating holes) on the leveling condition of the deposit has been investigated. Modeling of the deposition process in a microscreen-based micromold has been presented in this work for the first time in the literature.

2. Surface Texture. Surface texture is an important characteristic of materials which regulates several important properties such as wettability and optical characteristics. It is known in the literature that the surface texture of an electrodeposited structure depends on the applied overpotential. This part of the dissertation work presents an experimental investigation on the

effects of the overpotential on the surface texture of the copper deposit which has not been reported in the literature with this detail, previously. It is already known that proper design of the surface micro/nano topography can complement its chemical properties and lead to formation of superfunctionalities such as superhydrophobicity, self cleaning and anti-reflectivity. Different fabrication techniques such as lithography, etching or self assembly has been used by other authors to make properly designed surface features. In this part of the dissertation work, It has been shown that special electrochemical conditions result in developing multiscale surface features with reentrant geometry. The film deposited at these conditions shows excellent super-hydrophobic characteristic. In conclusion, the work identified electrodeposition as a low-cost technique for coating surfaces with a super-hydrophobic film. Developing superhydrophobic films by electrodeposition with the approach of this work has not been reported in the literature, so far. The work also presents a thermodynamic model to explain effects of the overpotential on the surface texture, qualitatively. The model has been inspired from the thermodynamic model presented previousely in the literature for the effect of temperature on the surface texture during themal solidification. A few studies in the field of electrodeposition have previously used this model but they all focused on developing a smooth film and eliminating surface features. In conclusion, the thermodynamic model presented in this work explains the behavior of the system at the range beyond that has been already covered in the literature.

3. Crystalline Strucrture. Several characteristics of the material such as hardness, ductility and thermal resistance depend on its crystalline structure. This work presents an investigation on the crystalline structure of one and two dimensional microparts made by electrodeposition. It is known in the literature that the crystalline structure formed during electrodeposition depends on

the applied overpotential. In this work, it has been shown that size and shape of the crystalline grains depend on a non-dimensional parameter which explains the relative importance of the mass transfer and electrochemical reaction in deposition process. Effect of the overpotential, size of the substrate and its position in the bath on this non-dimensional parameter has been discussed and connected to the effect of these manufacturing parameters on the size and shape of the crystalline grains. This approach for explaining effects of the manufacturing parameters on the crystalline structure of the deposit has not been presented in the literature previousely.

It has been reported in the literature that crystalline structure of the material is connected to its surface characteristics such as roughness. In this work this connection has been shown for the electrodeposited material. Moreover, a thermodynamic model has been used to explain this connection and relate that to the applied overpotential. This explanation has not been presented in the literature, so far.

Electron Transfer Kinetics on a Microelectrode. Kinetics of the electron-transfer reaction is considered as one of the main controlling parameters in electrocrystallization which can be neglected only at very high overpotentials, when the growth is mainly controlled by the mass transfer. Kinetic parameters depend on the properties of the electrode surface including chemical composition, crystal structure and metallography. Most of these properties depend on the preliminary treatment of the electrode surface such as polishing or cleaning. Consequently, kinetic parameters should be measured individually for each electrochemical system. Measurement techniques available in the literature, are hard to implement for the electrochemical reactions occuring on a microelectrode. This part of the dissertation work presents a new method to measure kinetic parameters, which is superior for the electrochemical reactions occuring on an electrode with micron or submicron dimensions. The method utilizes an analitical model of the surface

concentration which has been developed in this work. Model parameters are obtained with a limited number of potentiostatic measurements. The model has been explained through the kinetic measurement of the electrochemical reaction of copper on a platinum microelectrode.

Future work. Molecular dynamic techniques such as phase field model may be used to simulate the internal and external structure of the deposit and the results may be compared to the experimental data presented in Chapter 4 and 5 of the dissertation. In addition, the application of the electrodeposition for making powder using the technique presented in Chapter 4 may be further explored and the technique presented in Chapter 2 may be further expanded to measure kinetic parameter of a fast electron-transfer reaction on a macroelectrode.

Bibliography

[1] J.A. McGeough, M.C. Leu, K.P. Rajurkar, A.K.M. De Silva, Q. Liu, Electroforming Process and Application to Micro/Macro Manufacturing, CIRP Annals - Manufacturing Technology, 50(2) (2001) 499-514.
[2] W. Bacher, W. Menz, J. Mohr, The LIGA technique and its potential for microsystems-a survey, Industrial Electronics, IEEE Transactions on, 42(5) (1995) 431-441.
[3] E.W. Becker, W. Ehrfeld, P. Hagmann, A. Maner, D. Münchmeyer, Fabrication of microstructures with high aspect ratios and great structural heights by synchrotron radiation lithography, galvanoforming, and plastic moulding (LIGA process), Microelectronic Engineering, 4(1) (1986) 35-56.
[4] W. Ehrfeld, V. Hessel, H. Löwe, C. Schulz, L. Weber, Materials of LIGA technology, Microsystem Technologies, 5(3) (1999) 105-112.
[5] J. Hruby, LIGA Technologies and Applications, MRS Bulletin, (April 2001) 337-340.
[6] E. Mattsson, J.O.M. Bockris, Galvanostatic studies of the kinetics of deposition and dissolution in the copper + copper sulphate system, Transactions of the Faraday Society, 55 (1959) 1586-1601.
[7] T. Berzins, P. Delahay, Kinetics of Fast Electrode Reactions, Journal of the American Chemical Society, 77(24) (1955) 6448-6453.
[8] W. Vielstich, H. Gerischer, Zur Elektrolyse bei konstantem Potential, Zeitschrift für Physikalische Chemie, 4(1_2) (1955) 10-23.
[9] H. Gerischer, Mechanism of Electrolytic Deposition and Dissolution of Metals, Analytical Chemistry, 31(1) (1959) 33-39.
[10] H. Gerischer, M. Krause, Eine Doppelimpuls-Methode zur Untersuchung sehr schneller Elektrodenreaktionen, Zeitschrift für Physikalische Chemie, 10(3_4) (1957) 264-269.
[11] O.A. Kopistko, N.V. Grushina, The galvanostatic double-pulse method in the study of the kinetics of stepwise electrode reactions, Journal of Electroanalytical Chemistry and Interfacial Electrochemistry, 178(1) (1984) 21-43.
[12] R.S. Nicholson, Theory and Application of Cyclic Voltammetry for Measurement of Electrode Reaction Kinetics, Analytical Chemistry, 37(11) (1965) 1351-1355.
[13] K. Doblhofer, S. Wasle, D.M. Soares, K.G. Weil, G. Weinberg, G. Ertl, The Influence of Halide Ions on the Kinetics of Electrochemical Copper(II) Reduction, Zeitschrift für Physikalische Chemie, 217(5-2003) (2003) 479-492.
[14] R.L. Sarma, S. Nageswar, Role of 2-thiouracil as addition agent during the electrodeposition of copper on the copper (III) plane, Journal of Applied Electrochemistry, 17(3) (1987) 649-652.
[15] S.K. Griffiths, R.H. Nilson, A. Ting, R.W. Bradshaw, W.D. Bonivert, J.M. Hruby, Modeling electrodeposition for LIGA microdevice fabrication, Microsystem Technologies, 4(2) (1998) 98-101.
[16] K.S. Chen, G.H. Evans, Two-dimensional modeling of nickel electrodeposition in LIGA microfabrication, Microsystem Technologies-Micro-and Nanosystems-Information Storage and Processing Systems, 10(6-7) (2004) 444-450.
[17] R.A. Huggins, D. Elwell, Morphological stability of a Plane interface during electroncrystallization from molten salts, Journal of Crystal Growth, 37(2) (1977) 159-162.
[18] D. Landolt, P.F. Chauvy, O. Zinger, Electrochemical micromachining, polishing and surface structuring of metals: fundamental aspects and new developments, Electrochimica Acta, 48(20) (2003) 3185-3201.
[19] M.C. Lafouresse, P.J. Heard, W. Schwarzacher, Anomalous Scaling for Thick Electrodeposited Films, Physical Review Letters, 98(23) (2007) 236101.
[20] R. Aogaki, K. Kitazawa, Y. Kose, K. Fueki, Theory of powdered crystal formation in electrocrystallization—occurrence of morphological instability at the electrode surface, Electrochimica Acta, 25(7) (1980) 965-972.
[21] D. Quéré, Rough ideas on wetting, Physica A: Statistical Mechanics and its Applications, 313(1) (2002) 32-46.
[22] D. Quéré, Non-sticking drops, Reports on Progress in Physics, 68(11) (2005) 2495.
[23] D. Quéré, A. Lafuma, J. Bico, Slippy and sticky microtextured solids, Nanotechnology, 14(10) (2003) 1109.
[24] L. Gao, T.J. McCarthy, Wetting 101°†, Langmuir, 25(24) (2009) 14105-14115.
[25] B. He, N.A. Patankar, J. Lee, Multiple Equilibrium Droplet Shapes and Design Criterion for Rough Hydrophobic Surfaces, Langmuir, 19(12) (2003) 4999-5003.
[26] A. Lafuma, D. Quere, Superhydrophobic states, Nat Mater, 2(7) (2003) 457-460.
[27] W. Kurz, D.J. Fisher, Fundamentals of Solidification, Trans Tech Publications Ltd, Switzerland, 1998.
[28] Y. Gamburg, G. Zangari, Structure and Microstructure of Electrodeposited Metals and Alloys, in: Theory and Practice of Metal Electrodeposition, Springer New York, 2011, pp. 317-333.

[29] A.J. Bard, L.R. Faulkner, Electrochmeical methods, Fundamentals and applications, John Wiley & Sons, Danvers, 2001.
[30] D.W. Kimmel, G. LeBlanc, M.E. Meschievitz, D.E. Cliffel, Electrochemical Sensors and Biosensors, Analytical Chemistry, 84(2) (2011) 685-707.
[31] N.M. Marković, C.A. Lucas, B.N. Grgur, P.N. Ross, Surface Electrochemistry of CO and H2/CO Mixtures at Pt(100) Interface: Electrode Kinetics and Interfacial Structures, The Journal of Physical Chemistry B, 103(44) (1999) 9616-9623.
[32] S.N. Raicheva, The effect of the surface state on the electrochemical behaviour of copper electrodes, Electrochimica Acta, 29(8) (1984) 1067-1073.
[33] W. Chen, A.Y. Fadeev, M.C. Hsieh, D. Öner, J. Youngblood, T.J. McCarthy, Ultrahydrophobic and Ultralyophobic Surfaces: Some Comments and Examples, Langmuir, 15(10) (1999) 3395-3399.
[34] R. Holze, MEASUREMENT METHODS | Electrochemical: Potential and Current Steps, in: G. Editor-in-Chief: Jürgen (Ed.) Encyclopedia of Electrochemical Power Sources, Elsevier, Amsterdam, 2009, pp. 655-659.
[35] L. Heerman, A. Tarallo, Electrochemical nucleation on microelectrodes. Theory and experiment for diffusion-controlled growth, Journal of Electroanalytical Chemistry, 451(1-2) (1998) 101-109.
[36] V. Kapočius, V. Karpavičien, A. Steponavičius, Electrochemical Processes at a Platinum Electrode in CuSO4 Solutions in the UPD Region and at Initial Electrocrystallization Stages: Effect of Polyethylene Glycol, Russian Journal of Electrochemistry, 38(3) (2002) 274-279.
[37] A. Haghdoost, R. Pitchumani, Numerical analysis of electrodeposition in microcavities, Electrochimica Acta, 56(24) (2011) 8260-8271.
[38] A. Haghdoost, R. Pitchumani, Electrodeposition in Micromolds with a Microscreen Base, submitted to Acta Materialia, (2013).
[39] N.N.A. Lebedev, R.A. Silverman, Special Functions & Their Applications, Dover, 1972.
[40] G.N. Watson, A Treatise on the Theory of Bessel Functions, Cambridge, 1922.
[41] A.M. Azzam, J.O.M. Bockris, B.E. Conway, H. Rosenberg, Some aspects of the measurement of hydrogen overpotential, Transactions of the Faraday Society, 46(0) (1950) 918-927.
[42] J. Konya, NOTES ON THE NON-FARADAY ELECTROLYSIS OF WATER, J. Electrochem. Soc., 126(1) (1979) 54-56.
[43] A. Haghdoost, A.M. Dehkordi, M. Darbandi, M. Shahalami, J. Saien, Combined Model of Mass-Transfer Coefficients for Clean and Contaminated Liquid−Liquid Systems, Industrial & Engineering Chemistry Research, 50(8) (2011) 4608-4617.
[44] M.A. May, V.K. Gupta, K. Hounsokou, Electrochemical cell system for voltammetry of high purity solvents, Review of Scientific Instruments, 71(2) (2000) 516-518.
[45] A. Radisic, P.M. Vereecken, J.B. Hannon, P.C. Searson, F.M. Ross, Quantifying Electrochemical Nucleation and Growth of Nanoscale Clusters Using Real-Time Kinetic Data, Nano Letters, 6(2) (2006) 238-242.
[46] D. Grujicic, B. Pesic, Electrodeposition of copper: the nucleation mechanisms, Electrochimica Acta, 47(18) (2002) 2901-2912.
[47] S. Mehdizadeh, J.O. Dukovic, P.C. Andricacos, L.T. Romankiw, H.Y. Cheh, The Influence of Lithographic Patterning on Current Distribution: A Model for Microfabrication by Electrodeposition, J. Electrochem. Soc., 139(1) (1992) 78-91.
[48] K.B. Oldham, C.G. Zoski, Chapter 2: Mass Transport to Electrodes, in: C.H. Bamford, R.G. Compton (Eds.) Comprehensive Chemical Kinetics, Elsevier, 1986, pp. 79-143.
[49] K.B. Oldham, Limiting Currents for Steady-State Electrolysis of an Equilibrium Mixture, with and without Supporting Inert Electrolyte, Analytical Chemistry, 69(3) (1997) 446-453.
[50] D. Shoup, A. Szabo, Chronoamperometric current at finite disk electrodes, J. Electroanal. Chem. , 140 (1982) 237-245
[51] R.H. Byrd, R.B. Schnabel, G.A. Shultz, A Trust Region Algorithm for Nonlinearly Constrained Optimization, SIAM Journal on Numerical Analysis, 24(5) (1987) 1152-1170.
[52] S.C. Chang, J. Edens, Growth and crystallinity of electroformed nickel structures, in: S.C. Chang, S.W. Pang (Eds.) Micromachining and Microfabrication Process Technology III, SPIE, Austin, TX, USA, 1997, pp. 100-109.
[53] E.C. Hume, Iii, W.M. Deen, R.A. Brown, Mass Transfer Analysis of Electrodeposition Through Polymeric Masks, J. Electrochem. Soc., 131(6) (1984) 1251-1258.
[54] C. Madore, M. M., L. D., Experimental investigation of the primary and secondary current distribution in a rotating cylinder Hull cell Journal of Applied Electrochemistry, 22(12) (1992) 1155-1160.

[55] G.A. Prentice, C.W. Tobias, Simulation of Changing Electrode Profiles, J. Electrochem. Soc., 129(1) (1982) 78-85.
[56] R.C. Alkire, D.B. Reiser, R.L. Sani, Effect of Fluid Flow on Removal of Dissolution Products from Small Cavities, J. Electrochem. Soc., 131(12) (1984) 2795-2800.
[57] K.G. Jordan, C.W. Tobias, Simulation of the Role of Convection in Electrodeposition into Microscopic Trenches, J. Electrochem. Soc., 138(7) (1991) 1933-1939.
[58] J.M. Occhialini, J.J.L. Higdon, Convective Mass Transport from Rectangular Cavities in Viscous Flow, J. Electrochem. Soc., 139(10) (1992) 2845-2855.
[59] Y.M. Yeh., G.C. Tu., T.H. Fang., Nanomechanical properties of nanocrystalline Ni-Fe mold insert, Journal of Alloys and Compounds, 372(1-2) (2004) 224-230.
[60] Y. Guo, G. Liu, Y. Tian, Investigation on overplating high-aspect-ratio microstructure, in: M.-A. Maher, H.D. Stewart, J.-C. Chiao (Eds.) Micromachining and Microfabrication Process Technology XI SPIE, San Jose, CA, USA, 2006, pp. 61090M-61098.
[61] S. Um, C.Y. Wang, K.S. Chen, Computational Fluid Dynamics Modeling of Proton Exchange Membrane Fuel Cells, J. Electrochem. Soc., 147(12) (2000) 4485-4493.
[62] Z. Zhang, X. Wang, X. Zhang, L. Jia, Optimizing the Performance of a Single PEM Fuel Cell, Journal of Fuel Cell Science and Technology, 5(3) (2008) 031007-031009.
[63] F. Duarte, R. Gormaz, S. Natesan, Arbitrary Lagrangian-Eulerian method for Navier-Stokes equations with moving boundaries, Computer Methods in Applied Mechanics and Engineering, 193(45-47) (2004) 4819-4836.
[64] R. Alkire, T. Bergh, R.L. Sani, Predicting Electrode Shape Change with Use of Finite Element Methods, J. Electrochem. Soc., 125(12) (1978) 1981-1988.
[65] V.F.C. Lins, E.S. Cecconello, T. Matencio, Effect of the current density on morphology, porosity, and tribological properties of electrodeposited nickel on copper, Journal of Materials Engineering and Performance, 17(5) (2008) 741-745.
[66] B. Bhushan, Y.C. Jung, Wetting, Adhesion and Friction of Superhydrophobic and Hydrophilic Leaves and Fabricated Micro/Nanopatterned Surfaces, Journal of Physics: Condensed Matter, 20 (2008) 1-24.
[67] L. Feng, S. Li, Y. Li, H. Li, L. Zhang, J. Zhai, Y. Song, B. Liu, L. Jiang, D. Zhu, Super-Hydrophobic Surfaces: From Natural to Artificial, Adv. Mater. , 14 (2002) 1857-1860.
[68] M. Ma, R.M. Hill, Superhydrophobic surfaces, Current Opinion in Colloid & Interface Science 11(4) (2006) 193-202.
[69] T.L. Sun, L. Feng, X.F. Gao, L. Jiang, Bioinspired surfaces with special wettability (vol 38, pg 644, 2005), Accounts Chem. Res., 39(7) (2006) 487-487.
[70] M. Kargar, J. Wang, A.S. Nain, B. Behkam, Controlling bacterial adhesion to surfaces using topographical cues: a study of the interaction of Pseudomonas aeruginosa with nanofiber-textured surfaces, Soft Matter, 8(40) (2012) 10254-10259.
[71] K. Koch, B. Bhushan, Y.C. Jung, W. Barthlott, Fabrication of artificial Lotus leaves and significance of hierarchical structure for superhydrophobicity and low adhesion, Soft Matter, 5(7) (2009) 1386-1393.
[72] C.R. Crick, I.P. Parkin, Water droplet bouncing-a definition for superhydrophobic surfaces, Chemical Communications, 47(44) (2011) 12059-12061.
[73] H. Dettre Robert, E. Johnson Rulon, Contact Angle Hysteresis, in: Contact Angle, Wettability, and Adhesion, AMERICAN CHEMICAL SOCIETY, 1964, pp. 136-144.
[74] M.H. Sun, C.X. Luo, L.P. Xu, H. Ji, O.Y. Qi, D.P. Yu, Y. Chen, Artificial lotus leaf by nanocasting, Langmuir, 21(19) (2005) 8978-8981.
[75] C.W. Extrand, Model for Contact Angles and Hysteresis on Rough and Ultraphobic Surfaces, Langmuir, 18(21) (2002) 7991-7999.
[76] A. Marmur, Wetting on Hydrophobic Rough Surfaces: To Be Heterogeneous or Not To Be?, Langmuir, 19(20) (2003) 8343-8348.
[77] N.A. Patankar, On the Modeling of Hydrophobic Contact Angles on Rough Surfaces, Langmuir, 19(4) (2003) 1249-1253.
[78] D. Quéré, Wetting and Roughness, Annual Review of Materials Research, 38 (2008) 71-99.
[79] L. Gao, T.J. McCarthy, The “Lotus Effect” Explained: Two Reasons Why Two Length Scales of Topography Are Important, Langmuir, 22(7) (2006) 2966-2967.
[80] M. Nosonovsky, B. Bhushan, Hierarchical roughness optimization for biomimetic superhydrophobic surfaces, Ultramicroscopy, 107(10–11) (2007) 969-979.

[81] R.N. Wenzel, Resistance of Solid Surfaces to Wetting by Water, Industrial & Engineering Chemistry, 28(8) (1936) 988-994.
[82] A. Cassie, Baxter, S.,, Wettability of Porous Surfaces, Faraday Soc. Trans., 40 (1944).
[83] S. Yang, S. Chen, Y. Tian, C. Feng, L. Chen, Facile Transformation of a Native Polystyrene (PS) Film into a Stable Superhydrophobic Surface via Sol–Gel Process, Chemistry of Materials, 20(4) (2008) 1233-1235.
[84] C.Y. Kuan, M.H. Hon, J.M. Chou, I.C. Leu, Wetting Characteristics on Micro/Nanostructured Zinc Oxide Coatings, J. Electrochem. Soc., 156(2) (2009) J32-J36.
[85] Y. Li, X.J. Huang, S.H. Heo, C.C. Li, Y.K. Choi, W.P. Cai, S.O. Cho, Superhydrophobic Bionic Surfaces with Hierarchical Microsphere/SWCNT Composite Arrays, Langmuir, 23(4) (2006) 2169-2174.
[86] W. Ming, D. Wu, R. van Benthem, G. de With, Superhydrophobic Films from Raspberry-like Particles, Nano Letters, 5(11) (2005) 2298-2301.
[87] Y. Zhao, M. Li, Q. Lu, Tunable Wettability of Polyimide Films Based on Electrostatic Self-Assembly of Ionic Liquids, Langmuir, 24(8) (2008) 3937-3943.
[88] Y. Zhao, M. Li, Q. Lu, Z. Shi, Superhydrophobic Polyimide Films with a Hierarchical Topography: Combined Replica Molding and Layer-by-Layer Assembly, Langmuir, 24(21) (2008) 12651-12657.
[89] J.M. Lim, G.R. Yi, J.H. Moon, C.-J. Heo, S.-M. Yang, Superhydrophobic Films of Electrospun Fibers with Multiple-Scale Surface Morphology, Langmuir, 23(15) (2007) 7981-7989.
[90] K. Liu, J. Zhai, L. Jiang, Fabrication and characterization of superhydrophobic Sb2O3 films, Nanotechnology 19 (2008).
[91] M. Jin, X. Feng, J. Xi, J. Zhai, K. Cho, L. Feng, L. Jiang, Super-Hydrophobic PDMS Surface with Ultra-Low Adhesive Force, Macromolecular Rapid Communications, 26(22) (2005) 1805-1809.
[92] K. Teshima, H. Sugimura, Y. Inoue, O. Takai, A. Takano, Transparent ultra water-repellent poly(ethylene terephthalate) substrates fabricated by oxygen plasma treatment and subsequent hydrophobic coating, Applied Surface Science, 244(1-4) (2005) 619-622.
[93] L. Huang, S.P. Lau, H.Y. Yang, E.S.P. Leong, S.F. Yu, S. Prawer, Stable superhydrophobic surface via carbon nanotubes coated with a ZnO thin film, J. Phys. Chem. B, 109(16) (2005) 7746-7748.
[94] M. Thieme, R. Frenzel, S. Schmidt, F. Simon, A. Hennig, H. Worch, K. Lunkwitz, D. Scharnweber, Generation of ultrahydrophobic properties of aluminium - A first step to self-cleaning transparently coated metal surfaces, Adv. Eng. Mater., 3(9) (2001) 691-695.
[95] D. Ebert, B. Bhushan, Durable Lotus-effect surfaces with hierarchical structure using micro- and nanosized hydrophobic silica particles, Journal of Colloid and Interface Science, 368(1) (2012) 584-591.
[96] G. Li, B. Wang, Y. Liu, T. Tan, X. Song, E. Li, H. Yan, Stable superhydrophobic surface: fabrication of interstitial cottonlike structure of copper nanocrystals by magnetron sputtering, Science and Technology of Advanced Materials, 9 (2) (2008) 1-6.
[97] Y. Chen, S. Chen, F. Yu, W. Sun, H. Zhu, Y. Yin, Fabrication and anti-corrosion property of superhydrophobic hybrid film on copper surface and its formation mechanism, Surface and Interface Analysis, 41(11) (2009) 872-877.
[98] M. Whitley, M. Newton, G. McHale, N.J. Shirtcliffe, The Self Assembly of Superhydrophobic Copper Thiolate Films on Copper in Thiol Solutions, Zeitschrift für Physikalische Chemie, 226(3) (2012) 187-200.
[99] M.D. Pei, B. Wang, E. Li, X.h. Zhang, X.m. Song, H. Yan, The fabrication of superhydrophobic copper films by a low-pressure-oxidation method, Applied Surface Science, 256(20) (2010) 5824-5827.
[100] Q.M. Pan, H.Z. Jin, H. Wang, Fabrication of superhydrophobic surfaces on interconnected Cu(OH)(2) nanowires via solution-immersion, Nanotechnology, 18(35) (2007).
[101] Y. Li, W.Z. Jia, Y.Y. Song, X.H. Xia, Superhydrophobicity of 3D Porous Copper Films Prepared Using the Hydrogen Bubble Dynamic Template, Chemistry of Materials, 19(23) (2007) 5758-5764.
[102] T. Darmanin, E. Taffin de Givenchy, S. Amigoni, F. Guittard, Superhydrophobic surfaces by electrochemical processes, Advanced materials (Deerfield Beach, Fla.), 25(10) (2013) 1378-1394.
[103] X. Zhang, F. Shi, X. Yu, H. Liu, Y. Fu, Z. Wang, L. Jiang, X. Li, Polyelectrolyte Multilayer as Matrix for Electrochemical Deposition of Gold Clusters: Toward Super-Hydrophobic Surface, Journal of the American Chemical Society, 126(10) (2004) 3064-3065.
[104] N.J. Shirtcliffe, G. McHale, M.I. Newton, G. Chabrol, C.C. Perry, Dual-Scale Roughness Produces Unusually Water-Repellent Surfaces, Advanced Materials, 16(21) (2004) 1929-1932.
[105] L. Wang, S. Guo, S. Dong, Facile electrochemical route to directly fabricate hierarchical spherical cupreous microstructures: Toward superhydrophobic surface, Electrochemistry Communications, 10(4) (2008) 655-658.

[106] S. Wang, L. Feng, H. Liu, T. Sun, X. Zhang, L. Jiang, D. Zhu, Manipulation of Surface Wettability between Superhydrophobicity and Superhydrophilicity on Copper Films, ChemPhysChem, 6(8) (2005) 1475-1478.
[107] N.J. Shirtcliffe, G. McHale, M.I. Newton, C.C. Perry, Wetting and Wetting Transitions on Copper-Based Super-Hydrophobic Surfaces, Langmuir, 21(3) (2005) 937-943.
[108] M.D. Abramoff, P.J. Magelhaes, S.J. Ram, Image Processing with ImageJ, Biophotonics International, 11(7) (2004) 36-42.
[109] A.F. Stalder, T. Melchior, M. Muller, D. Sage, T. Blu, M. Unser, Low-bond axisymmetric drop shape analysis for surface tension and contact angle measurements of sessile drops, Colloid Surf. A-Physicochem. Eng. Asp., 364(1-3) (2010) 72-81.
[110] B.T. McDonald, T. Cui, Superhydrophilic surface modification of copper surfaces by Layer-by-Layer self-assembly and Liquid Phase Deposition of TiO2 thin film, Journal of Colloid and Interface Science, 354(1) (2011) 1-6.
[111] A. Tuteja, W. Choi, G.H. McKinley, R.E. Cohen, M.F. Rubner, Design Parameters for Superhydrophobicity and Superoleophobicity, MRS Bulletin, 33(08) (2008) 752-758.
[112] S. Poulston, P.M. Parlett, P. Stone, M. Bowker, Surface Oxidation and Reduction of CuO and Cu2O Studied Using XPS and XAES, Surface and Interface Analysis, 24(12) (1996) 811-820.
[113] F.-M. Chang, S.-L. Cheng, S.-J. Hong, Y.-J. Sheng, H.-K. Tsao, Superhydrophilicity to superhydrophobicity transition of CuO nanowire films, Applied Physics Letters, 96(11) (2010) 114101-114103.
[114] L.P. Bicelli, B. Bozzini, C. Mele, L. D'Urzo, A Review of Nanostructural Aspects of Metal Electrodeposition Int. J. Electrochem. Sci., 3(4) (2008) 356-408.
[115] T.G. Nieh, J. Wadsworth,, O.D. Sherby., Superplasticity in Metals and Ceramics, Cambridge University Press, 1997.
[116] A. Jankowski, Modeling Nanocrystalline Grain Growth during the Pulsed Electrodeposition of Gold-Copper, ECS Transactions, (2006).
[117] S. Villain, P. Knauth, G. Schwitzgebel, Electrodeposition of Nanocrystalline Silver: Study of Grain Growth by Measurement of Reversible Electromotive Force, The Journal of Physical Chemistry B, 101(38) (1997) 7452-7454.